Two-level noise and stochastic resonance in individual permalloy nanoscale magnets

A DISSERTATION
SUBMITTED TO THE FACULTY OF THE GRADUATE SCHOOL
OF THE UNIVERSITY OF MINNESOTA
BY

Bern Willem Youngblood

IN PARTIAL FULFILLMENT OF THE REQUIREMENTS
FOR THE DEGREE OF
DOCTOR OF PHILOSOPHY

E. DAN DAHLBERG

August 2015

Acknowledgements

There are a number of people without whom this work would not have been possible. First and foremost, I am indebted to my advisor Dan, for taking me on as a student and teaching me to see the value of simplicity in an experiment. The graduate students with whom I shared a lab—Tanner Schultz, Dan Endean, Barry Costanzi and David Harrison—all assisted with this work, either materially, or by teaching me what I would need to survive graduate school. Barry in particular has been a springboard for ideas, an outlet for frustration, and a capable pair of hands throughout graduate school.

A few words of thanks to technical staff: to Dr. Brian Cord for his tireless work keeping the Vistec operational, despite the machine's best efforts to the contrary. To Jon Kilgore for teaching me what actual precision machining entails. And to Dr. Paul Crowell who (in addition to providing scientific guidance throughout this study) shepherded us all through what could have been a much more painful move between buildings.

Finally, I am forever grateful to my wife Janelle, partly for being a good enough sport to accompany me to the lab on a Saturday morning and ride the elevator in order to obtain the data used in figure 5.5, but also for editing the many drafts of this thesis and patiently educating me on my (mis)use of commas.

On a more formal note, this work was jointly supported by ONR Grant N00014-11-1-0850 and by the MRSEC program of the NSF under Grant No. DMR-0819885. Portions of this work were performed in the Minnesota Nano Center, which receives funding from the NSF through the NNIN program. Portions of this work were also performed in the University of Minnesota Characterization Facility, which receives funding from the NSF through the MRSEC program.

To Janelle, for everything.

Abstract

We present the results of a study on stochastic resonance in individual magnetic random telegraph oscillators. We have fabricated sub-micron magnetic samples, which have multiple stable magnetic states. We are able to observe random telegraph switching between magnetic states and tune the energetics by varying the temperature and applied external field. If a small AC field is applied to the system, it will modulate the energy well depth for the two states and the system shows stochastic resonance near the matching condition $2f_A = \omega_D$, where ω_D is the drive frequency and f_A is the characteristic frequency of magnetic transitions. We fit our measured data for the resonance amplitude and phase of the particle as a function of temperature to a linear-response model and obtain good agreement. At low temperatures we observe a peak in the phase lag of the returned signal, which is consistent with linear-response theories. At higher temperatures, our fitted model parameters suggest that the particle has an energy surface that is not sinusoidal. This contradicts our initial approximation for the energy surface, but it is consistent with a model for magnetic energy that takes into account the magnetization dynamics near the conditions for random telegraph switching.

Our work is the first clear observation of stochastic resonance in a single superparamagnetic particle where the energetics are modulated by an applied field. In addition, our work is the first physical system where stochastic resonance has been characterized with sufficient detail to allow for comparison to linear-response models.

Contents

List of Figures

Chapter 1

Introduction

1.1 Noise-added systems

The good experimentalist must eventually address noise in his or her experiment, and the idea that no signal can ever be truly constant in time is a lesson that is best learned quickly. This can be an exercise in frustration if one thinks of a noisy signal as a wrong signal, or, at least, a signal that is not what it "should" be. In reality, noise is intrinsic to any experiment and it should be present as much as the signal should be (however such a signal is defined). Far from being a detriment to measurement, random time variations in a signal can often give insight to the processes that drive some physical event. Less often, noise can even enhance the behavior of a system. This thesis will present the results of an experiment on stochastic resonance, a phenomenon that falls into this latter category.

This paper is organized as follows: chapter 1 will discuss an overview of noise and includes a brief introduction to stochastic resonance. Chapter 2 will present an in-depth overview of stochastic resonance, as well as the relevant theory for noise, and some background on the magnetic system we use in our experiment. In chapter 3, we will discuss the experimental methods used to both make and measure our samples. In chapters 4 and 5, we will present our results, both with regards to stochastic resonance and other effects that we observed in our system. Finally, in chapter 6, we will discuss what conclusions can be drawn from our work, as well as future directions we would like to go with this research.

1.1.1 Types of noise

While all noise is inherently random, there are several classifications of noise that can be distinguished mathematically. Four of these are shown in Fig. 1.1(a)-(d). While it is apparent from the time data that they are different, it can be difficult to describe in words exactly how they are different. For this reason, it is common in the field of noise to work in the frequency domain by applying a Fourier transform to obtain the noise power spectrum $S(\omega)$, as shown in Fig. 1.1(e)-(h), where such differences become more quantitative.

The first type of noise shown is white noise, called such because its power spectral density (PSD) is constant in frequency. White noise is a manifestation of any signal where each sample is uncorrelated in time with all other samples. It typically follows a Gaussian distribution of sample density, although other distributions (e.g., uniform) are possible. Common examples of white noise in physical systems include shot noise on an electrical current, caused by the discrete charges that make up such a current,[1] and Johnson-Nyquist noise on a resistor,[2] caused by thermal motion of charges. The second of these will be of importance in this study when we discuss the limitations of our measurement equipment in chapter 3.

The second type of noise depicted is $1/f$ noise, also known as pink or flicker noise. It is characterized by a PSD that follows a $1/f$ curve at low frequencies. (It is common to plot $S(\omega)$ with logarithmic scales for both axes, so a $1/f$ spectrum appears as a slope of -1.) At high frequencies, any real spectrum will eventually be dominated by the white noise background, which can be seen in Fig. 1.1(f) near 10^2 Hz. $1/f$ noise has been observed in an incredibly broad range of systems, including electronic amplifiers, stock market prices, flood levels, traffic movement, and musical works.[3] As yet, there is no universal explanation for it, although it is theorized[4,5] that it may arise from a collection of uncorrelated two-level oscillators, as discussed below.

The type of noise that will be most fundamental to our study is two-level noise, also known as random telegraph noise (RTN). RTN arises in a system that has two stable states and is undergoing random transitions between the two. These random transitions are driven by thermal (white) fluctuations of the underlying mechanism, so RTN is never seen without an associated white noise component. RTN is sometimes referred to as $1/f^2$ noise, because its PSD follows a $1/f^2$ dependence on frequency for part of

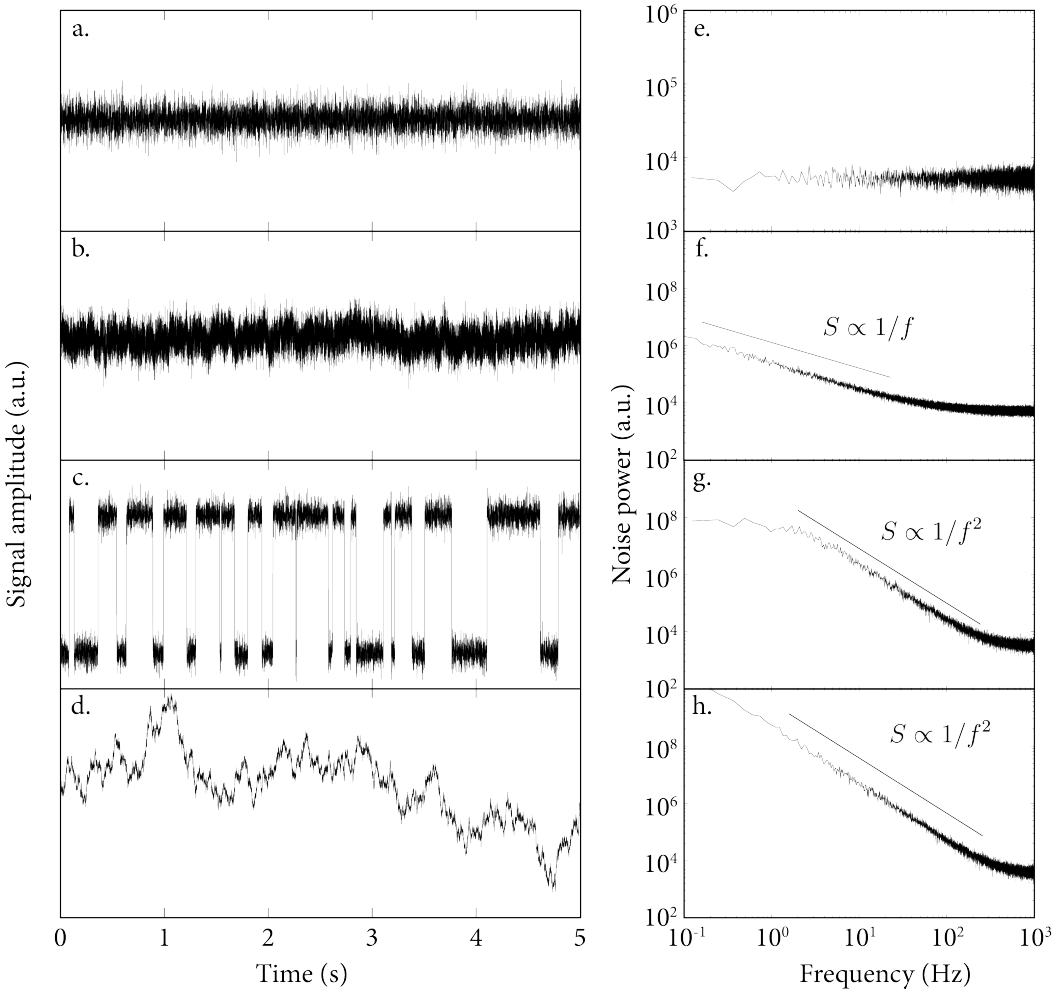

Figure 1.1: Different examples of noise. (a)-(d) show four different examples of noise with the corresponding PSD plotted in (e)-(h). From top, types of noise shown are white noise, $1/f$ noise, RTN, and Brownian noise.

the spectrum,[1] as shown in Fig. 1.1(g). We caution, however, that this is somewhat deceptive since there are other types of noise that also show a $1/f^2$ dependence. Brownian noise, also known as random-walk or red noise is one such class and is shown in Fig. 1.1(h). In the time domain, however, Brownian noise appears qualitatively different, and it arises from a different phenomenon (time integration of a white noise signal). It has been shown theoretically[4] that a set of uncorrelated RTN oscillators with a flat spectrum of activation energies will give rise to pink noise, but this has not been shown experimentally to be the source of pink noise in real systems.

1.1.2 Beneficial noise

Noise is generally thought of as a detriment to any measurement system because it obscures the signal being measured. There are a few specialized cases, however, where the addition of a small amount of noise can actually make the signal more apparent.

Dither noise: When a signal is digitized by a measurement device with finite resolution, the analog input is forced to a quantized series of levels, either by truncating digits or by rounding. This can have spurious effects for low-level signals where the total signal only spans a few bits of resolution because the process of digitization can produce a result that looks very unlike the original. A solution is to artificially introduce dither noise to the signal before digitization.[6] This creates a noisier output, but an output that looks more analog, as shown in Fig. 1.2. In effect, we are reducing the signal cleanliness in order to obtain better accuracy of the overall signal shape. Dithering is a commonly used technique in both image and audio processing to correct for artifacts such as high-frequency whine (in audio) or color banding (in images).

Stochastic resonance: Stochastic resonance is a phenomenon that can occur in two-level systems subject to some AC driving force. If the driving force is insufficient to induce transitions of its own accord, the system can still display correlated switching behavior, so long as there is enough thermal noise present to induce RTN. The magnitude and phase lag (relative to the drive signal) of this switching is determined, in part, by the ratio of the drive frequency to the characteristic frequency of RTN. Stochastic resonance has been observed in a number of

Figure 1.2: The author's cat. (a) shows original image, while (b) and (c) are both rendered in 1-bit black and white. (c) shows the effects of dithering. Adding random noise to the image before processing retains a greater amount of detail and gives the effect of an analog grayscale, rather than a binary filter.

> biological systems, as well as in Schmitt trigger circuits, and is theorized to drive natural phenomena such as the ice ages.[7]

Stochastic resonance and dithering are not the same effect, but they do share some commonalities. Both arise in strongly nonlinear systems with some degree of quantization and both involve the system's response to a low-level signal. We can set up analogous equations for the two systems to determine the conditions where noise is beneficial. In the case of dithering, this is that

$$\Delta A_{sig} < nA_{lev}, \tag{1.1}$$

where ΔA_{sig} is the total range of signal amplitude, A_{lev} is the range of a single discretation level, and n is some small integer (typically less than 10). The equivalent condition for stochastic resonance is that

$$F_{drive} < F_{switch}, \tag{1.2}$$

where the two quantities are the magnitude of the driving force and the force necessary to switch the system, independent of any noise. Eqs. 1.1 and 1.2 express the necessary conditions for a small amount of excess noise to be beneficial to the system. Noise can still be present when they are not satisfied, but its effect will be to obscure, rather than to improve, the system response.

1.2 Magnetic noise

Magnetic systems can exhibit noise as fluctuations in either the magnitude or direction of their net magnetization. White noise and $1/f$ noise have both been reported in magnetic samples,[5,8] but magnetic systems are most commonly associated with RTN. This is because many magnetic systems are anisotropic in energy as a function of magnetization direction, so they naturally have two or more stable states. Our work will focus on a system with a single magnetic particle that we can engineer to have two stable states. We will be primarily interested in using the RTN of the particle to drive stochastic resonance in the magnetization.

Chapter 2

Background and theory

2.1 Micromagnetics

2.1.1 Energetics of magnetism

The structure of a ferromagnet is governed by the desire to minimize the energy from two competing effects: the exchange interaction and dipole coupling to the local magnetic field. The first of these, exchange, is purely a quantum mechanical effect and is responsible for the existence of ferromagnetism. Exchange can occur when two electrons' wavefunctions overlap in space. This overlap costs a certain amount of Coulomb energy since both have charge e^-, but the system can minimize this energy by restricting the two electrons to different momentum eigenstates, reducing their spatial overlap. This affects the magnetization because the electrons are forced into the same spin eigenstate in order to maintain the overall antisymmetry of the paired wavefunction. Exchange forces can then be thought of as the result of the Coulomb interaction, combined with the Pauli exclusion principle. They are most commonly encountered in magnetics, but can show up in any system of charged fermions where there are two or more degenerate (or near-degenerate) eigenstates.

Because exchange forces require wavefunction overlap, they are not a long-range interaction and it is typical to approximate them as only occurring between nearest

neighbors within a lattice. The total energy due to exchange forces can be written as

$$E = -2J \sum_{i,j} \mathbf{S}_i \cdot \mathbf{S}_j, \tag{2.1}$$

where the summation in i is taken over the entire lattice of spins and the summation in j is taken over the set of nearest neighbors to each spin $\mathbf{S}_i$. The quantity J is a coupling constant that, by definition, is positive for ferromagnets.

Interactions between individual spins and the local magnetic field provide the second constraint on magnetic structure, and form a less straightforward calculation. Fundamentally, the energy of a magnetic dipole in a magnetic field (in cgs units) is given by

$$E_i = -\mu_B \mathbf{S}_i \cdot \mathbf{H}_i, \tag{2.2}$$

and one can sum over all i as before. This is complicated, however, by the fact that a local field $\mathbf{H}_i$ can arise from a number of sources, such as an externally applied field, the spin-orbit interaction, or other dipoles within the sample. This means that $\mathbf{H}$ is almost always position-dependent and often nontrivial to calculate. To simplify matters, it is customary to break $\mathbf{H}$ into its constituent parts and deal with each separately. The first contribution, from an external field, is easiest to work with since an external field typically can be approximated as uniform. The total external-field (Zeeman) energy, then, is just

$$E_z = -\boldsymbol{\mu} \cdot \mathbf{H}_{ext}, \tag{2.3}$$

where $\boldsymbol{\mu} \equiv \sum \mu_B \mathbf{S}_i$.

Fields that arise out of spin-orbit interactions cause crystalline anisotropy, i.e., the tendency of the magnetization to prefer certain directions relative to the crystal orientation of the lattice. They are of immense importance for commercial magnets because they determine the material's resistance against demagnetization. For our study, however, a crystalline anisotropy would be an undesirable complication, and so we have specifically selected materials where this effect is negligible.

Dipole-dipole fields (also termed demagnetization fields) will be the most interesting for our study because they, along with the exchange force, will determine the internal magnetic structure of our samples in zero applied field. Ostensibly, it is possible to evaluate the demagnetization field by summing the field of all individual dipoles

$$\mathbf{H}(\mathbf{r}) = \frac{1}{4\pi}\int_V \frac{3(\mathbf{M}\cdot\hat{\mathbf{r}})\hat{\mathbf{r}} - \mathbf{M}}{|\mathbf{r}-\mathbf{r}'|^3} d^3\mathbf{r}', \tag{2.4}$$

with $\hat{\mathbf{r}} \equiv (\mathbf{r}-\mathbf{r}')/|\mathbf{r}-\mathbf{r}'|$. In practice, however, it is typically easier[9] to split the integral into volume and surface components:

$$\mathbf{H}(\mathbf{r}) = \frac{1}{4\pi}\int_V \frac{(\nabla'\cdot\mathbf{M})d^3\mathbf{r}'}{|\mathbf{r}-\mathbf{r}'|^3}(\mathbf{r}-\mathbf{r}') + \frac{1}{4\pi}\int_A \frac{(\mathbf{n}'\cdot\mathbf{M})d^2\mathbf{r}'}{|\mathbf{r}-\mathbf{r}'|^3}(\mathbf{r}-\mathbf{r}'). \tag{2.5}$$

The benefit of this form is that for a magnetic structure with no divergence, the first integral drops out and one only needs to sum over surface charges. Examining the second part of Eq. 2.5 we can see that the only contribution to the dipolar field (and by extension the energy) is from areas where $\mathbf{n}'\cdot\mathbf{M}$ is nonzero. Put another way, this means that the system can lower its energy if the magnetization is parallel to a surface. This leads to a phenomenon known as shape anisotropy whereby a particle with uniform magnetization prefers to have that magnetization oriented along a particular direction because doing so lowers its dipolar coupling. As an example, consider a thin film of area A and thickness l, where $l \ll A^{1/2}$. If the magnetization is oriented normal to the plane, Eq. 2.5 can be evaluated to give $\mathbf{H} = -4\pi\mathbf{M}$ inside the film. If the magnetization is oriented in-plane, however, the dipolar field is negligible because the only contribution is from surface charges along the vanishingly small edge. Our magnetic structures are not infinitely thin films, but this approximation still holds to the extend that we expect the out-of-plane component of $\mathbf{M}$ to be negligible in our samples.

2.1.2 Configurational anisotropy

In the ideal scenario, a magnetic structure should be able to minimize its dipolar energy by having the magnetization conform to all edges. For a finite sample, however, this requires curvature of the magnetization, which will cost exchange energy. Configurational anisotropy arises when a sample adopts some internal magnetic structure in order to balance these two competing effects. It is strongly dependent on sample shape, but it differs from a shape anisotropy in that it relies on an inhomogeneous magnetization rather than just the dipole field from the edges. Because of this, it can be difficult *a priori* to predict what the ground state structure should be for a sample of a given shape. The ground state also can differ for two samples with identical aspect ratios, but

different absolute sizes. There are, however, two general statements that can be made regarding configurational anisotropy:

> *Larger samples tend to form magnetic vortices or domains.* This occurs because a magnetic vortex has a local exchange energy density that drops off as $1/r^2$ for large r, where r is the distance from the vortex core. This means that, beyond a certain radius, the exchange energy cost per spin is negligible. The exchange energy for a domain wall is proportional to the length of the wall, which is expected to scale linearly with the sample radius. By contrast, a magnetization configuration that is quasi-uniform will have a dipole energy cost that grows quadratically with sample radius in a thin film (linear in sample volume). Above a certain critical size, therefore, the dipole energy will surpass the exchange energy and the system will prefer a vortex or multidomain configuration. This critical size is both material and shape dependent and the distinction between a vortex and a multidomain state can be poorly defined for materials with low crystalline anisotropy.
>
> *Shape symmetries are preserved.* A sample with twofold symmetry in its shape must show the same twofold symmetry in its anisotropy. This only applies to the symmetry axes, however; it does not say anything about where minima or maxima will be.

For our study, we need at least two symmetric energy minima where the energy maximum separating the two can be tuned so that it is comparable to thermal energies. We have found that the easiest way to accomplish this is by making samples that are square (fourfold symmetry) and then control the height of the interwell maximum by applying an external Zeeman field (see Fig. 2.1). Other studies[10–17] have seen magnetic RTN using the same basic method in samples with twofold anisotropy—typically crystalline—but we have found that a fourfold symmetry arrangement is easier to fabricate in very small samples and allows for finer control of the barrier height.

2.1.3 Anisotropic magnetoresistance

Directly observing the magnitude and direction of a magnetization is very difficult in individual small samples. Most conventional measurement techniques rely on observing

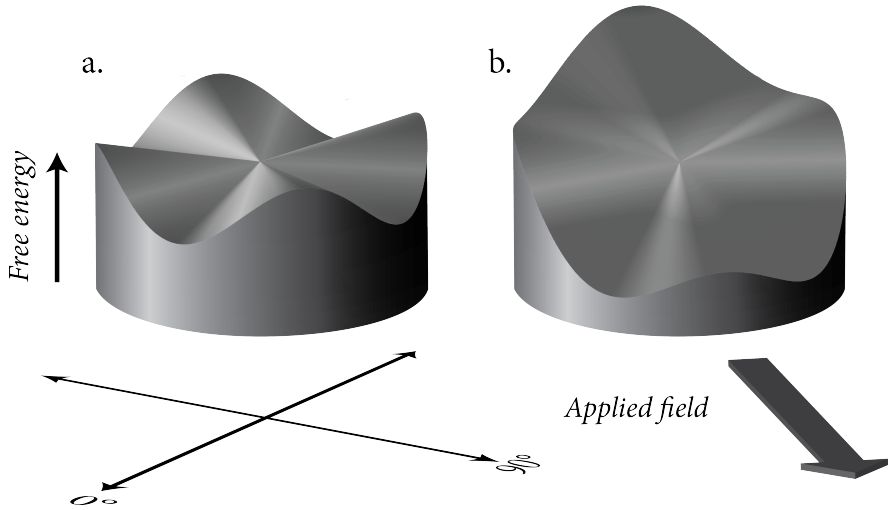

Figure 2.1: Free energy surface for a particle with fourfold symmetry and fourfold configurational anisotropy. With no applied field, as in (a), the free energy can be approximated as a $\cos(4\phi)$ function that has four symmetric wells. With the application of an external field along the 45° direction, as in (b), the entire surface will be tilted to favor two wells with a single energy barrier separating them. The barrier height is tunable by adjusting the magnitude of **H**.

the dipole flux created by a magnet with a macroscopic probe. This is accomplished either using the Lorentz force, as in a vibrating sample magnetometer or Hall probe, or by observing the flux directly, as in a superconducting quantum interference device (SQUID). Both of these, however, lack the sensitivity to accurately characterize a nanoscale sample. A commercial SQUID such as the Quantum Designs MPMS 3 has an ultimate resolution of 5×10^{-8} emu.[18] For comparison, a permalloy sample measuring 250 nm × 250 nm × 10 nm should be expected to have a moment of 6×10^{-12} emu if it is uniformly magnetized.

Other techniques such as magnetic force microscopy or spin-polarized scanning tunneling microscopy can have the necessary sensitivity to observe the field from a nanoscale sample. A problem with these methods, however, is that they both observe a local field rather than the net magnetization of a sample, as well as introducing other complications. In the case of magnetic force microscopy, the interaction between sample and probe is inherently perturbative, i.e., an interaction that is strong enough to alter the resonance properties of the probing cantilever should also be strong enough to affect the

magnetization dynamics at the conditions for RTN. Spin-polarized scanning tunneling microscopy should be nonperturbative, but because it uses a density-of-states measurement, it can be difficult to separate the magnetic properties of the bulk from those at the surface. The bulk spins are the primary component of the net magnetic moment, but a tunneling measurement will involve a large percentage of electrons tunneling to and from surface states in both the sample and the probing tip. This can lead to false characterization if the two are qualitatively different.

For our study, we observe the magnetization indirectly by measuring the anisotropic magnetoresistance (AMR). This allows us to take advantage of the extremely high sensitivity of a pure voltage measurement. In addition, AMR should be relatively nonperturbative since no external field is necessary and it maps easily to magnetization angle, provided one knows the direction of the source current. (There are still second-order effects that will be discussed in section 5.3.)

Phenomenologically, AMR is a change in electrical resistivity for a ferromagnet that, to first order, varies sinusoidally with the angle ϕ' between the magnetization direction $\mathbf{M}$ and the current $\mathbf{I}$. It can be expressed as

$$\rho(\phi') = \rho_0 + \delta\rho \cos^2 \phi'. \tag{2.6}$$

The quantity $\delta\rho$ is usually positive, meaning that the sample shows the highest resistance when the current and magnetization are collinear.

AMR differs from ordinary magnetoresistance because it is not observed in nonmagnetic materials with the application of an external field. It requires a nonzero magnetization and not just a total flux $\mathbf{B}$ because it is an entirely quantum process that arises from asymmetric scattering cross sections rather than the Lorentz force. In a ferromagnet, the total current can be modeled as a mix of spin-up and spin-down currents which are further divided into s and d wave subcurrents.[9] These spin and angular momentum states are largely conserved as electrons move through the lattice, but there can be spin-flip scattering processes via the the spin orbit interaction, or other, higher-order effects. Any change in the scattering rate for these spin-flip processes will then affect the overall electrical resistivity as electrons scatter into conduction states with a higher or lower electrical resistance.

For a $3d$ ferromagnet, the primary spin-flip process is from a spin-up s state into

a spin-down d hole.[19,20] The likelihood of this process will be determined, in part, by the incoming electron having total angular momentum similar to that of the final state. If such an electron is moving in the $\hat{z}$ direction, it will have an angular momentum relative to a scatterer that is a linear combination of L_x and L_y. If the magnetization is also oriented along $\pm\hat{z}$, there will be a large number of empty states with angular momentum L_x or L_y and the electron can scatter easily into these states. (We have assumed there is a strong imbalance of occupied states favoring $\mathbf{L} \parallel \mathbf{M}$.) By contrast, if the magnetization is oriented along $\hat{y}$, there will be relatively few empty L_y states and scattering in this direction will be suppressed. A configuration with $\mathbf{M} \perp \mathbf{I}$, therefore, will have fewer overall scattering events and a correspondingly lower resistivity.

2.2 Theory of RTN

2.2.1 One-dimensional problem

The theoretical framework for RTN was first presented by Kramers,[21] who treated the problem as one of diffusive mechanics. That is, the average rate of transition for a single system from state A to state B should be equivalent to the current from A to B for a collection of uncorrelated systems, all in thermodynamic equilibrium and scaled by the number of systems initially in state A. For simplicity, consider the scenario shown in Fig. 2.2, where we have a number of particles confined in an initial (physical) well and we can ask what their rate of escape is over the barrier.

Such a collection of particles should be expected to obey the Smoluchowski diffusion equation†

$$\frac{\partial \sigma}{\partial t} = -\frac{1}{\eta}\frac{\partial}{\partial x}\Big[F(x)\sigma\Big] + \frac{T}{\eta}\frac{\partial^2 \sigma}{\partial x^2}, \tag{2.7}$$

where $\sigma(x,t)$ is the spatial distribution function, $F(x)$ is the force felt by a particle at location x, T is the temperature, and η^{-1} is the relaxation time due to viscous effects. Physically, the first term on the right in Eq. 2.7 expresses the tendency for drift effects to bias the population density toward areas of low energy, while the second term represents the tendency of diffusion to move particles from areas of high density to areas of low density.

† for ease of notation, we have set $k_B = 1$ throughout this chapter, so that T has units of energy

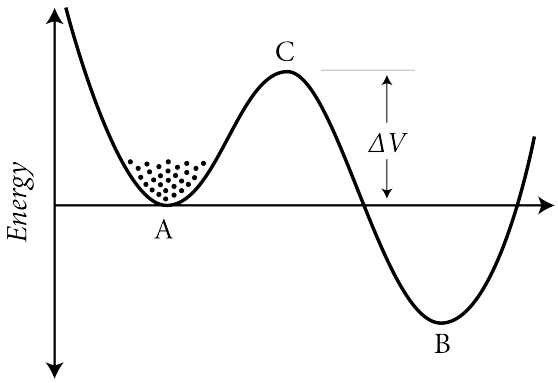

Figure 2.2: Double well system. The particles confined at A are all in thermodynamic equilibrium, but confined to a local minimum. Their rate of escape to the global minimum B is limited by classical hopping of the energy barrier ΔV.

Since we are concerned with a steady-state solution, we can set $\dot{\sigma} = 0$ and integrate to obtain

$$j = \frac{F(x)\sigma}{\eta} - \frac{T}{\eta}\frac{\partial \sigma}{\partial x}, \tag{2.8}$$

where j is the diffusion current between two points that are, for now, unspecified. In order to turn this into a more useful form, we note that Eq. 2.8 is equivalent to

$$j = -\frac{T}{\eta} e^{-U/T} \frac{\partial}{\partial x}(\sigma e^{U/T}), \tag{2.9}$$

with $-U' = F$. Because j is assumed to be constant in both time and space, this can be recast as

$$j = T\left(\sigma e^{U/T}\Big|_B^A\right)\left\{\eta \int_A^B e^{U/T} dx\right\}^{-1}. \tag{2.10}$$

Physically, the term $\sigma e^{U/T}|_B^A$ in Eq. 2.10 states that the diffusion current should be proportional to the imbalance of particles between the two locations A and B scaled by the relative likelihood of being in those two locations. In addition, the integral term represents the likelihood of a particle visiting every state between A and B, a necessary condition for current flow.

For the problem of escaping from an energy well we assume that the number of particles at B is vanishingly small so that the first term reduces to σ_A (taking $U = 0$ at A). The integral is simplified by assuming that all values of x not very close to the top

of the peak will be negligible because of the exponential term. If we then approximate the energy in the region of C as

$$U \approx \Delta U - \frac{1}{2}\omega_C^2 (x - C)^2, \tag{2.11}$$

the integral in Eq. 2.10 takes the familiar Gaussian form

$$\int_A^B e^{U/T} dx \approx e^{\Delta U/T} \int_{-\infty}^{\infty} e^{-\omega_C^2 \frac{(x-C)^2}{2T}} dx = \sqrt{\frac{2\pi T}{\omega_C^2}} e^{\Delta U/T}. \tag{2.12}$$

Inserting Eq. 2.12 into Eq. 2.10 gives the particle current across the barrier, but if we are concerned with escape rate, we still need to scale by the number of particles initially near A:

$$n_A = \int_{A-\delta}^{A+\delta} \sigma e^{U/T} dx, \tag{2.13}$$

which, by the same argument as before, also reduces to a Gaussian integral

$$n_A = \sigma_A \int_{-\infty}^{\infty} e^{-\omega_A^2 \frac{(x-C)^2}{2T}} dx = \sigma_A \sqrt{\frac{2\pi T}{\omega_A^2}}. \tag{2.14}$$

Combining these two equations gives the Kramers result[21,22] for the escape frequency $f_A = j/n_A$:

$$f_A = \frac{\omega_A \omega_C}{2\pi\eta} e^{-\Delta U/T}. \tag{2.15}$$

Two points should be made regarding Eq. 2.15. First, if there is more than one degenerate path over the barrier, the integral in Eq. 2.10 should be scaled by the multiplicity Ω of the paths:

$$\int_A^B e^{U/T} dx \longrightarrow \frac{1}{\Omega} \int_A^B e^{U/T} dx, \tag{2.16}$$

which is equivalent to measuring the barrier height in free energy $\Delta U \to \Delta U - T\Delta S$.[23] Second, the preceding work is only valid in the limit of high damping since Eq. 2.7 assumes that we are only concerned with long-time behavior for which motion on the

order of η^{-1} can be neglected. If this is not the case, it can be shown[22] that a more general form arises, where

$$f_A = \frac{\omega_A}{2\pi\omega_C}\left(\left[\frac{\eta^2}{4}+\omega_C^2\right]^{1/2}-\frac{\eta}{2}\right)e^{-\Delta U/T}. \tag{2.17}$$

In the limit of $\eta \gg \omega_C$, this reduces to Eq. 2.15. In the opposite limit of very low damping (or a sharply peaked barrier), however, it has the simplified form

$$f_A = \frac{\omega_A}{2\pi}e^{-\Delta U/T}. \tag{2.18}$$

This illustrates why the Arrhenius prefactor is referred to as the attempt frequency, since, in a frictionless well, we expect the escape rate to be equal to the natural resonance frequency of the well, multiplied by the Boltzmann probability that any given particle has the energy ΔU necessary to clear the barrier.

2.2.2 Application to magnetic systems

In magnetic systems, it is necessary to work in three dimensions, but, for simplicity, we will restrict the system to a single magnitude of magnetization M. The magnetization can be temperature dependent, but it is independent of the direction of $\mathbf{M}$. The problem then becomes radially symmetric and we can consider only rotational changes. As before, we seek a steady-state current density j between two points on the unit sphere. In this case, however, it is simpler to write the current in the form

$$j = \sigma\mathbf{v} - k'\nabla\sigma, \tag{2.19}$$

with $\mathbf{v}$ as the net velocity of points on the unit sphere due to non-diffusive forces, i.e., $\mathbf{v} = (d\mathbf{M}/dt)/M$. The benefit here is that $d\mathbf{M}/dt$ can be expressed by the Landau-Lifshitz-Gilbert equation:[24,25]

$$\frac{d\mathbf{M}}{dt} = \mathbf{M}\times\left(\gamma\mathbf{H}_{\text{eff}} - \frac{\lambda}{M^2}\left[\mathbf{M}\times\mathbf{H}_{\text{eff}}\right]\right), \tag{2.20}$$

with γ and λ representing the gyromagnetic ratio and damping constant. Note that in this notation λ has units of time rather than inverse time from before. The effective

field, $\mathbf{H}_{\text{eff}}$, includes both Zeeman contributions and magnetic anisotropy, and can be represented in terms of the energy as

$$\mathbf{H}_{\text{eff}} = -v^{-1}\frac{\partial U}{\partial \mathbf{M}}. \tag{2.21}$$

In addition, it can be shown[23] that the constant k' has a similar form as the one-dimensional case:

$$k' = \frac{\lambda T}{M^2 v}. \tag{2.22}$$

Inserting Eq. 2.20 into Eq. 2.19 gives the following full form of the particle current j:

$$j = \frac{\mathbf{M}}{M} \times \left(\gamma \mathbf{H}_{\text{eff}} - \frac{\lambda}{M^2}\left[\mathbf{M} \times \mathbf{H}_{\text{eff}}\right]\right)\sigma - k'\nabla\sigma. \tag{2.23}$$

This generally cannot be directly solved even with an exact expression for $U(\mathbf{M})$, but if we limit ourselves (for now) to the uniaxial case where there are two minima at $\theta = 0, \pi$ it has the greatly simplified form for the linear current density j_θ:

$$j_\theta = -\frac{k'}{T}\frac{\partial U}{\partial \theta}\sigma - k'\frac{\partial \sigma}{\partial \theta}. \tag{2.24}$$

The total current between the two poles is found by integrating around all ϕ: $I_{AB} = 2\pi j_\theta \sin\theta$. Then, multiplying both sides of Eq. 2.24 by $e^{U/T}$ and integrating by parts yields

$$\frac{I}{2\pi k' T}\int_{\theta_A}^{\theta_B}\frac{e^{U/T}d\theta}{\sin\theta} = \sigma e^{U/T}\Big|_{\theta_A}^{\theta_B}, \tag{2.25}$$

which is an exact analog to Eq. 2.10. Again, it is sufficient to approximate the integral by the Taylor series expansion near the maximum of U since the exponential will kill off any contribution of points far from this maximum. By identical math as in 2.2.1, this can be evaluated to give an overall particle current

$$I = \sigma_A k' \sin\theta_m \sqrt{2\pi U''_m T}\, e^{\Delta U/T} \tag{2.26}$$

and transition rate

$$f = k' U''_A \sin\theta_m \sqrt{\frac{U''_m}{2\pi T}}\, e^{\Delta U/T}, \tag{2.27}$$

where U_A'' and U_m'' represent the second derivative of energy in the initial well and at the top of the barrier, respectively. Eq. 2.27 represents the two-dimensional analog to Eq. 2.15 where the ω_i have been replaced by the energy derivatives U_i''.

In the more general case where we do not have axial symmetry, it is not possible to separate the two directions ϕ and θ in Eq. 2.23. Nevertheless, the same technique can be used to show that the switching frequency is given by

$$f = \frac{\lambda\gamma^2\sqrt{c_1^{(A)}c_2^{(A)}}}{2\pi M^2}\frac{\left(c_2^{(m)}-c_1^{(m)}\right)+\sqrt{(c_1^{(m)}+c_2^{(m)})^2+4c_1^{(m)}c_2^{(m)}/\zeta^2}}{\sqrt{c_1^{(m)}c_2^{(m)}}}e^{\Delta U/T},$$
$$\zeta \equiv \frac{\gamma\lambda M}{\gamma^2M^2+\lambda^2}, \tag{2.28}$$

where the $c_i^{(A,m)}$ represent the Taylor series coefficients of energy in the two direction cosines, α_1 and α_2, at the initial point and at the barrier.[23,26](See Fig. 2.3)

Eq. 2.28 was derived in the high damping limit ($\lambda^{-1} \gg c_i^{(m)}\gamma/M$). Successive work has focused on extending this to intermediate and low damping.[26–30] The results follow the pattern established in Eq. 2.17, such that a change in the damping parameter tends to modify the functional dependence on λ, and $c_i^{(m)}$, but leaves the dependence on the

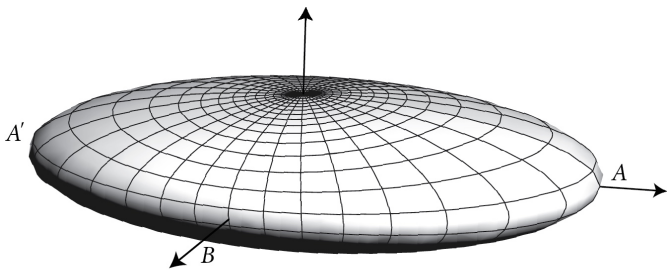

Figure 2.3: Typical well depth $\delta U(\theta,\phi)$ plotted as a function of magnetization direction for a thin-film magnetic particle with uniaxial anisotropy. The total energy is given by $E_{\text{tot}} \equiv U_0 - \delta U$. Points A and A' are energy minima; points B and B' (not shown), are saddle points with a minimum in θ and a maximum in ϕ. Near these points the energy can be approximated as $U = U_0^{(i)} + 1/2(c_1\alpha_1^2 + c_2\alpha_2^2)$.

shape of the well unchanged. In general, therefore, we can say that for an arbitrary double-welled system, we expect that

$$f_i = \frac{\gamma\sqrt{c_1^{(i)}c_2^{(i)}}}{2\pi M}\xi(\lambda, M, U_m)e^{\Delta U/T}, \tag{2.29}$$

where $\xi(\lambda, M, U_m)$ is some function that depends on the damping coefficient, the magnetization, and the shape and entropy of the barrier. Finally, if $M = M_s$, where M_s is the saturation magnetization, we have

$$f_i = \frac{\omega_{\text{FMR}}^{(i)}}{2\pi}\xi(\lambda, M_s, U_m)e^{\Delta U/T}, \tag{2.30}$$

since $\omega_{\text{FMR}}^{(i)} = \gamma c_{avg}^{(i)}/M_s$ defines the ferromagnetic resonance frequency of the energy minimum.[9]

2.3 Stochastic resonance

2.3.1 Phenomenology

Stochastic resonance is a well-known perturbative effect that can occur in a two-level system that displays RTN. Normally, such a system has a response function that has a $1/f^2$ spectrum. Or, if the measured quantity is denoted by $\chi(t)$, the Fourier transform $S_\chi(f)$ has a lineshape that goes as[1]

$$S_\chi(f) = \frac{4\Delta\chi^2}{(f_A^{-1} + f_B^{-1})\left[(f_A + f_B)^2 + 2\pi f^2\right]}. \tag{2.31}$$

The continuous nature of this power spectrum is a reflection of the fact that, even though there is a characteristic escape frequency f_i for the two wells, the individual switching events are uncorrelated (a pure square wave will also have a $1/f^2$ spectrum, but will be represented by a series of spikes, rather than a smooth curve). If, however, a two-level system is subjected to some small driving force

$$F(t) = A_0\cos(\omega_D t), \tag{2.32}$$

it can begin to show correlated switching at the driving frequency ω_D, even if the drive amplitude A_0 is much less than what would be necessary to switch the system

independently. Put another way, if we consider the system to be a rudimentary amplifier that is responding to the input signal $F(t)$, at low temperature, the response of the system will be almost 0 since the driving force is not sufficient to induce transitions. Raising the temperature and increasing the transition rate will then have the effect of drastically increasing the drive amplification. This is very different from the behavior of a typical amplifier for which increasing the random noise (temperature) of the system will only decrease the signal response.

Stochastic resonance was first proposed as a method for explaining the apparent periodicity of the global ice ages,[31] since the only known drive mechanism with a comparable periodicity is the variation in solar flux caused by perturbations in Earth's orbit. This variation is on the order of 0.1%, however, which is much too small to account for the observed climate effects, unless it is only serving to correlate what is fundamentally a stochastic process. More recently, stochastic resonance has been observed in a number of bistable systems including nonlinear optoelectronics, particles in a double laser trap, superconducting quantum interference devices, bistable chemical reactions, and sensory neuron stimulation.[7]

2.3.2 Approximate theoretical treatment

To obtain a quantitative expression for the amplification of a stochastic resonator system, we begin by setting up the master equation for the system:[32]

$$\frac{dn_A}{dt} = \tilde{f}_B n_B - \tilde{f}_A n_A, \tag{2.33}$$

where the n_i represent the probabilities of being in each of the two wells, and $\tilde{f}_i$ are the (time dependent) transition rates out of each well. Making note of the fact that $n_A + n_B = 1$, this can be rewritten as

$$\frac{dn_A}{dt} = \tilde{f}_B - (\tilde{f}_B + \tilde{f}_A) n_A. \tag{2.34}$$

This is an ordinary differential equation with the solution

$$\begin{aligned} n_A(t) &= g(t)^{-1} \left[n_A(t_0) + \int_{t_0}^{t} \tilde{f}_B(t') g(t') dt' \right], \\ g(t) &= \exp\left(\int_{t_0}^{t} \left[\tilde{f}_B(t') + \tilde{f}_A(t') \right] dt' \right). \end{aligned} \tag{2.35}$$

Normally, the integrals in Eq. 2.35 cannot be analytically evaluated, but if we assume that the driving force has a low enough amplitude that the Arrhenius law still holds, we have

$$\tilde{f}_i = f_0^{(i)} \exp\left[\frac{\Delta U_i + U_0 \cos(\omega_D t)}{T}\right]. \tag{2.36}$$

To second order in U_0/T, this is approximated as

$$\tilde{f}_i = f_i \left[1 \pm \frac{U_0}{T}\cos(\omega_D t) + \left(\frac{U_0}{T}\right)^2 \cos^2(\omega_D t) \pm \ldots\right], \tag{2.37}$$

where f_i represents the original, time-independent switching rate. If we make the further simplification of assuming a symmetric well such that $f_A = f_B$, the integrals can be evaluated to give (taking $n_A(0) = 1$ as an initial condition)

$$n_A(t) = e^{-2f_A t}\left(\frac{1}{2} - f_A \frac{U_0}{T}\frac{\cos\varphi}{\sqrt{4f_A^2 + \omega_D^2}}\right) + \frac{1}{2} - f_A \frac{U_0}{T}\frac{\cos(\omega_D t - \varphi)}{\sqrt{4f_A^2 + \omega_D^2}}, \tag{2.38}$$

with

$$\varphi \equiv \arctan\left(\frac{\omega_D}{2f_A}\right). \tag{2.39}$$

Inspecting Eq. 2.38, it is clear that the first term is a transient that dies out exponentially as the system loses information about its initial state. This makes sense given that, in the absence of a driving force, the long term behavior of the system should tend toward $n_A = n_B = 1/2$. The final term represents the probability response function to the driving force. If we are interested, then, in the overall state of the system at this driving frequency, we can multiply n_A by the zero-drive amplitude (ZDA) of the measured variable (in our case, a magnetization) and read off the amplitude and phase lag:

$$\mathscr{M}(T, \omega_D) = \mathrm{ZDA}\frac{U_0}{T}\frac{2f_A}{\sqrt{4f_A^2 + \omega_D^2}} \tag{2.40}$$

$$\varphi(T, \omega_D) = \arctan\left(\frac{\omega_D}{2f_A}\right), \tag{2.41}$$

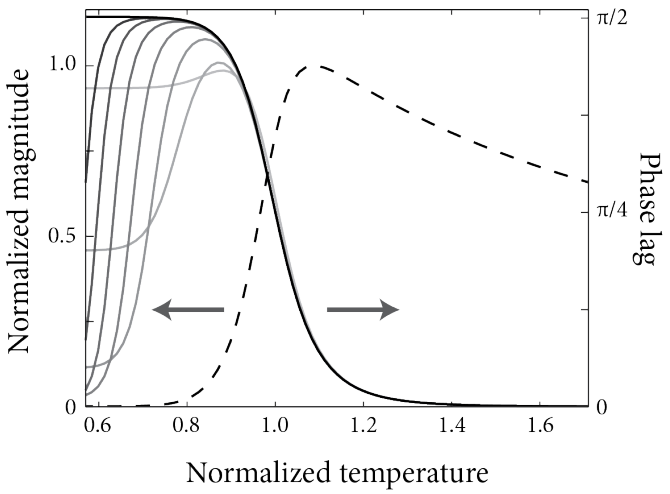

Figure 2.4: Amplitude (dashed) and phase lag (solid) for $\mathscr{M}$ as a function of normalized temperature $T/\overline{T}$ where $\overline{T}$ is defined by $\omega_D = 2f_A(\overline{T})$. For the phase, the black line shows φ with no corrections (Eq. 2.41), while the shaded lines show the effect of progressively stronger intrawell oscillations, as discussed in 2.3.3.

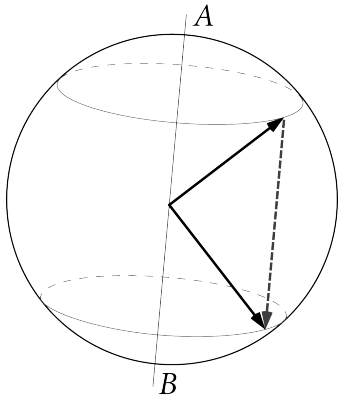

Figure 2.5: Vector modulation $\mathscr{M}(T, \omega_D)$ for a uniaxial particle. Solid vectors represent the expectation values $\langle \mathbf{M}_A \rangle$ and $\langle \mathbf{M}_B \rangle$ at the frequency ω_D if the actual $\mathbf{M}_A$ and $\mathbf{M}_B$ are at the two poles. $\mathscr{M}(T, \omega_D)$ is given by the magnitude of the dashed vector.

where the prefactor ZDA is defined as the time expectation value of the absolute deviation of $\mathbf{M}$, or ZDA $\equiv \langle|\mathbf{M} - \overline{\mathbf{M}}|\rangle$ with no driving field.

The functional form of Eqs. 2.40 and 2.41 is plotted in Fig. 2.4. We emphasize that the quantity $\mathscr{M}(T, \omega_D)$ represents a rotation of the vector $\mathbf{M}$ at the frequency ω_D as shown in Fig. 2.5. It is not a change in the magnitude of magnetization M (which is still assumed to be constant), and it represents a change in $\mathbf{M}$ that is less than that of the total RTN signal, $\mathbf{M}_A - \mathbf{M}_B$. Also, the peak in $\mathscr{M}(T, \omega_D)$ happens near the natural resonance of the system, but it is not exact (the peak is determined by solving the transcendental equation formed from taking $d\mathscr{M}/dT = 0$).

2.3.3 Expansion to linear response

It is natural to question the approximation in Eq. 2.37, where it was assumed that the driving amplitude is much less than thermal energies $U_0 \ll T$. Physically, this simplification is equivalent to assuming that the recovered signal is entirely due to interwell transitions rather than oscillations around a single minimum. This is reasonable at high temperatures, but it cannot be the case in the limit of $T \to 0$, because the exponential dependence on T will suppress the interwell transitions, and small oscillations will be the dominant contribution to $\mathscr{M}(T, \omega_D)$. To do better, we need a continuous model that allows the particle to take on any value between the wells A and B. There are several methods[7] of extending the two-state approximation of Sec. 2.3.2 into this regime, but we will only deal with linear-response theory here, since it provides an intuitive framework for working with the measurable quantities in our experiment.

In linear response, one considers the frequency-dependent response function $\chi(\omega)$, which is related to the amplitude and phase of oscillations by

$$\mathscr{M} = U_0|\chi(\omega_D)|, \qquad \varphi = \arctan\left(\frac{\mathrm{Im}\chi(\omega_D)}{\mathrm{Re}\chi(\omega_D)}\right). \tag{2.42}$$

If we assume that all relaxation modes for the system are independent (separate processes cause each possible mode of relaxation), it is possible[33,34] to write this response function as

$$\chi(\omega) = \frac{\mathrm{ZDA}}{T}\sum_k \frac{w_k}{1 + i\omega\tau_k}, \tag{2.43}$$

where τ_k are the relaxation times for the system and w_k are weighting coefficients that represent the internal order of the system at a given drive amplitude and noise power. Note that Eq. 2.43 should not be surprising since it follows the same form as an undamped harmonic oscillator with drive frequency ω. In the two state approximation, we allow for only one eigenvalue $\tau_1 = 1/2f_A$ with weight $w_1 = 1$ to exactly recover the result of Eqs. 2.40 and 2.41. More generally, however, we should retain terms out to $k = 3$ since the system will have the primary (interwell) relaxation mode as well as two additional modes from direct relaxation within each well. Also, it cannot be assumed that the coefficients w_k are constants in T, since with increasing thermal energy, the system is able to reach states where the linear approximations for τ_2 and τ_3 are no longer valid. (This is equivalent to relaxing the requirement that the integral in Eq. 2.12 becomes negligibly small while x is still small.[23])

For the one-dimensional case, where the potential is given by a pure (symmetric) quartic function, it can be shown that[34,35] the susceptibility takes the approximate form

$$\chi(\omega_D) \approx \frac{\mathrm{ZDA}}{T}\left[f_A \frac{1+\tilde{T}/\Omega_0}{f_A + i\omega_D} + \frac{\tilde{T}}{\Omega_0 + i\omega_D}\right], \tag{2.44}$$

where Ω_0 is the natural resonance frequency of the damped well and $\tilde{T}$ is the temperature-scaled frequency of thermal oscillations, i.e., $\tilde{T} = \gamma T/\mu$ for a magnetic system with moment μ. Note that while Ω_0 is related to the prefactor on f_A, they are not necessarily the same, since f_A depends nontrivially on damping.

Including the corrections for intrawell motion has only a small qualitative effect on the magnitude of oscillations $\mathscr{M}$. Generally, it tends to decrease the sharpness of the peak and move it to higher temperatures. By contrast the effect on the phase is dramatic, particularly at low temperatures. Examining the phase as defined by Eqs. 2.42 and 2.44 (approximated to lowest order in ω_D/Ω_0)

$$\varphi = \arctan\left(\frac{\omega_D}{\Omega_0}\frac{\Omega_0^2 f_A + \omega_D^2 \tilde{T}}{\Omega_0 f_A^2 + \omega_D^2 \tilde{T}}\right), \tag{2.45}$$

we can see that at low temperatures where f_A is exponentially suppressed, the system tends toward a phase lag $\varphi \approx \arctan(\omega_D/\Omega_0)$. This is not only independent of temperature, it should be expected to be close to zero, since $\omega_D/\Omega_0 \ll 1$ for reasonable drive and

relaxation parameters. The phase is relatively unaffected at temperatures high enough to drive interwell transitions since this signal will dominate that of intrawell motion and we still recover that $\varphi \to 0$ for $T \to \infty$ as before. Given this, it follows that there must be some crossover regime where the susceptibility moves from primarily intrawell to primarily interwell motion and, in this region, the phase lag will peak at a value less than $\pi/2$. This behavior is shown in the shaded plots of Fig. 2.4 and is starkly different from the case for which intrawell motion is ignored. It should be noted that, while it is difficult to measure the intrawell motion directly, it can have a pronounced effect on the returned signal phase if the Arrhenius exponent U_0/T is low enough that transitions are observable at a few tens of Kelvin.

Chapter 3

Methods

3.1 Sample preparation

3.1.1 Overview

Samples are all fabricated in-house using our self-maintained UHV sputtering system, as well as tools in the Minnesota Nano Center (MNC). A cartoon of our samples is shown in Fig. 3.1, where the central square pillar is the magnetic structure. Structures are built additively on silicon substrates and require a fabrication process with three major steps. First, we create the macroscale electrical contacts and a set of marks that will be used to align subsequent layer geometries (see Fig. 3.2). The second step is to create the magnetic dot, and the third is to build a set of microvias that connect the macroscale contacts to the dot.

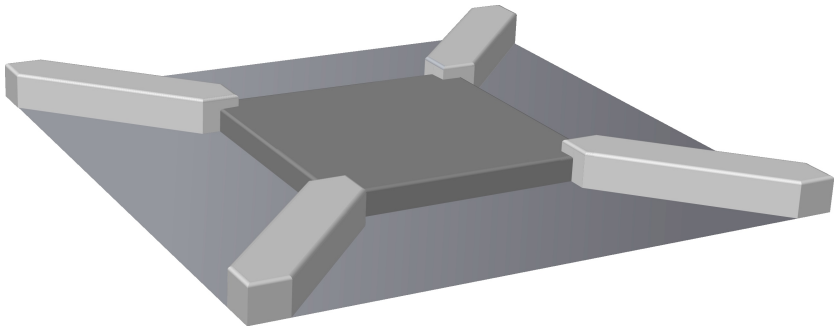

Figure 3.1: Cartoon of magnetic sample. Central square structure is the magnetic dot.

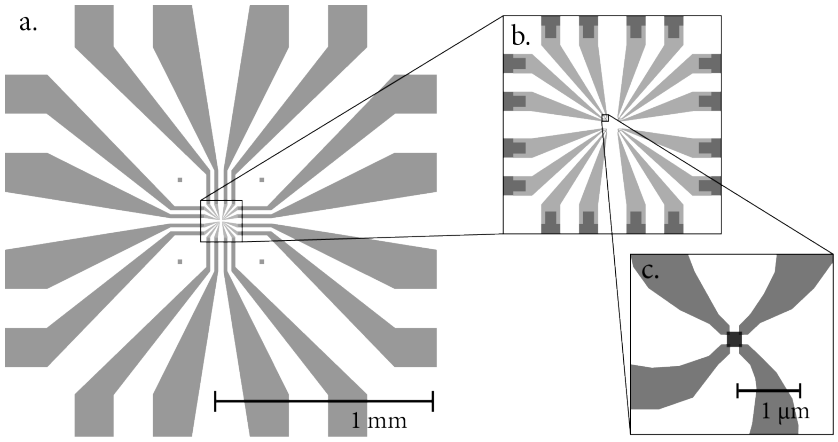

Figure 3.2: (a) Contact geometry for a single area. Each chip contains 9 areas for a total of 36 samples. Inset view (b) shows microvias that are created with electron beam lithography during the third processing step. Inset (c) shows magnetic dot and contacts. Full contact arrangement is sized to allow for wirebonding from mounting block to contact pads.

3.1.2 Sample geometry

We create the two preferred states of our system through a configurational anisotropy that relies on the demagnetization field and the structure geometry to create energy minima. This type of rectangular structure has been predicted theoretically by Cowburn et al. to have a fourfold angular anisotropy,[36] which has been experimentally verified by our lab.[37] From the phase diagram shown in Fig. 3.3, it is clear that there are several distinct magnetization states that the system prefers, depending on side length and film thickness. Of these, the "flower" and "buckle" states are the most desirable for this experiment because they have a magnetization structure where the net moment will be parallel to one edge. By contrast, for a system displaying a vortex state, there is no net moment across the dot and it is therefore very difficult to characterize such a state using AMR. In the "leaf" state, the net magnetization lies along the diagonal. While this is not useful for this study since the $+45°$ and $-45°$ states are symmetric with respect to current direction, it is possible that a different contact geometry would allow us to observe RTN in a sample jumping between two leaf states.

Our lab has studied permalloy dots of varying sizes[37] and observed similar transitions as predicted in Fig. 3.3. Specifically, for a structure 10 nm thick, we see a transition

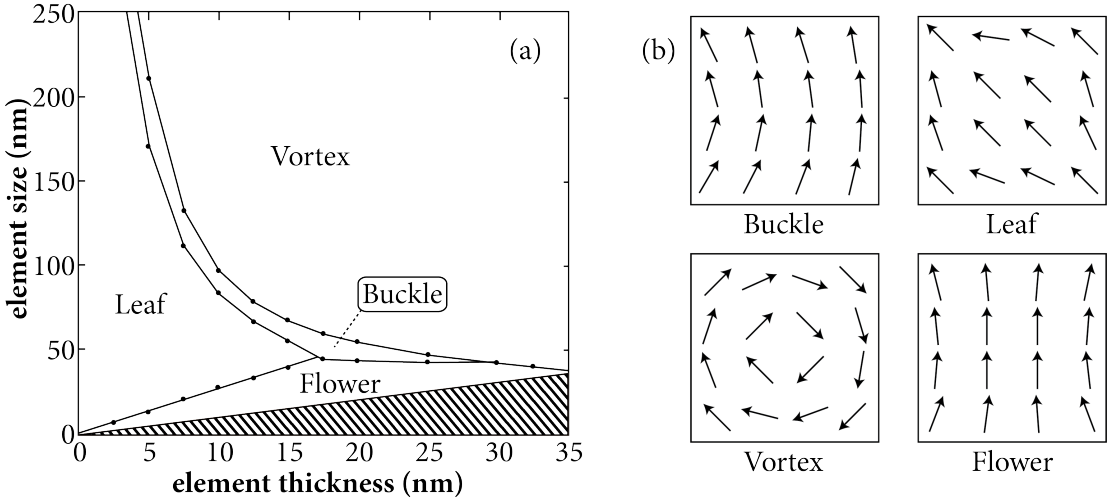

Figure 3.3: (a) Phase diagram showing the ground state magnetic structure for a thin square of permalloy as a function of sample geometry. Reprinted, with permission from [36]. (b) Cartoons of magnetic domain structure for each of the four states.

from vortex to buckle ground state as the side length of the dot is decreased. In our system, this transition typically occurs between side lengths of 250-300 nm. This is larger than the predicted transition point around 100 nm seen in Fig. 3.3. We attribute this discrepancy primarily to processing imperfections that may lead to features such as corner rounding.

3.1.3 Contact geometry

When designing contacts that will connect to the dot, the primary concern is minimizing contact resistance while still maintaining reliability. The contact resistance provides the primary source of the Johnson-Nyquist noise that will ultimately determine the limits of resolution, and so it is advantageous to minimize this resistance as much as possible by having a large cross-sectional current path and large overlaps between contacts and dot. There is a limit here, though, when dealing with very small dots, because a large overlap necessarily means that the contacts are closer together. In very tight contact geometries, an electron beam lithography system will naturally tend to overdose fine features and this can lead to resist collapse and shorted or broken leads. In our setup, we have achieved the best signal-to-noise ratios using contacts that are 212 nm wide at

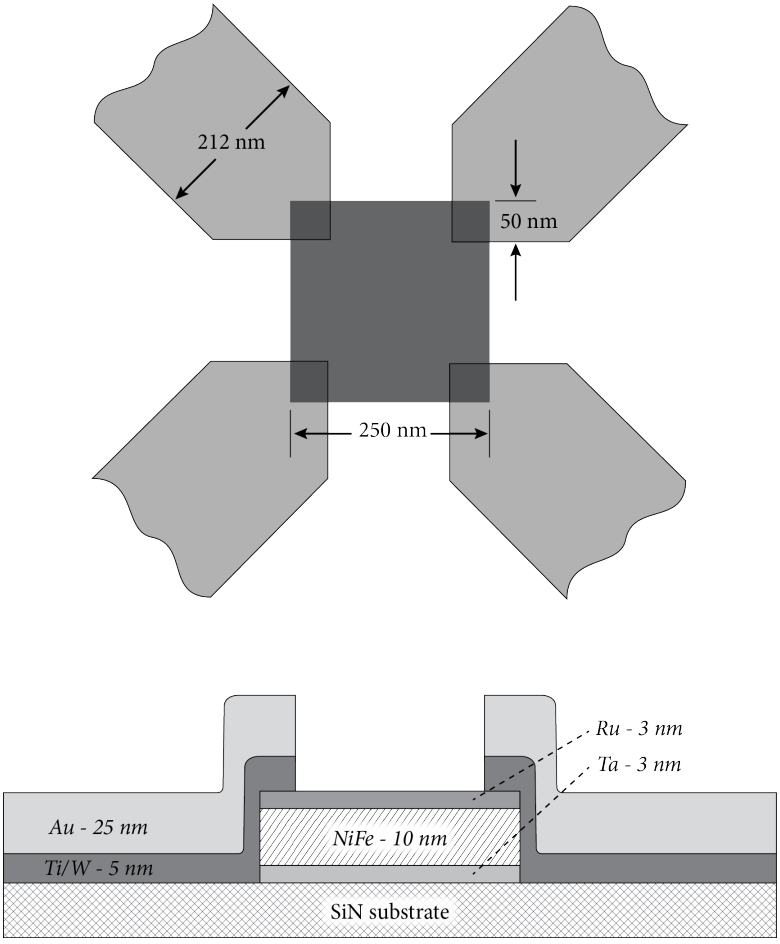

Figure 3.4: Geometry of 250 nm dot (top) and cross-sectional view (bottom, not to scale) showing the thicknesses and order of layers. Dot and contact structures are deposited in separate steps with ex-situ processing between them.

their narrowest point and have 50 nm × 50 nm overlap with the dot as shown in Fig. 3.4. With this geometry, our two-terminal contact resistances are between 150 Ω and 200 Ω.

3.1.4 Materials considerations

Our experiment relies on configurational anisotropy to create a tunable energy surface. Accordingly, the magnetic material must have minimal crystalline anisotropy. A class of materials that satisfies this is permalloy, the alloy formed from Ni_xFe_{1-x}, which displays an approximately uniform energy surface for x near 0.75. A further benefit of permalloy is that in a similar range of stoichiometry, it displays a large peak in anisotropic magnetoresistance with values as high as $\Delta\rho/\rho = .05$ for $x = 0.9$.[9] Throughout this study, we have used $Ni_{81}Fe_{19}$ with a purity of 99.95% as the source material for magnetic structures.

Two additional layers are used for the magnetic structure as shown in Fig. 3.4. The first is a seed layer that is required because of permalloy's poor adhesion to insulating substrates. For this layer, we have used tantalum, chosen not only for its adhesive properties, but also because it has little to no interdiffusion with permalloy.[38] A final capping layer is also required because deposition of magnetic structures and contacts cannot be performed in-situ. Specifically, if the permalloy were left uncapped, it would oxidize, altering its magnetic properties drastically. In addition, the formation of an oxide at the surface can create an electrical barrier, raising the two-terminal resistance to the point where the sample becomes unmeasurable. For optimal results, the capping layer needs to fulfill several criteria: it should have minimal oxidation, it should not interdiffuse readily with permalloy, and it should have a relatively low conductivity to avoid shunting too much of the current away from the magnetic layer. The second two requirements eliminate a material such as gold from being a viable option, because, while gold does not oxidize, it has a very low resistivity relative to permalloy (2.06 μΩ cm for gold[39] versus 16 μΩ cm for bulk permalloy[40]) and will readily interdiffuse.[38] We have found that a thin layer of ruthenium provides the best compromise within these constraints. While it readily oxidizes, its primary oxidation state, RuO_2, is itself metallic with a resistivity of 36 μΩ cm and does not easily diffuse.[41] For this reason it has been commonly proposed as a potential diffusion barrier between electrodes in semiconductor

work.[42–44]

The primary constraints on the electrical contacts are that they should not affect the magnetic properties of the dot, should themselves be nonmagnetic, and should have high electrical conductivity to minimize Johnson-Nyquist noise. We have tried a number of different materials for this, including tantalum, a bilayer of molybdenum/gold and a bilayer of chromium/gold. Our best results, however, have been with bilayers of titanium/gold and bilayers of tungsten/gold. In both cases, the gold provides the primary path for electrical current and the titanium or tungsten are used for their adhesive properties. The success of the titanium recipe is somewhat surprising since titanium is known to readily interdiffuse with permalloy.[45] It is possible, though, that titanium impurities in the permalloy have a beneficial effect by inhibiting electromigration. This will be discussed in section 5.3.2.

3.1.5 Substrate preparation

Our sample substrates are 100 mm commercial Si wafers, purchased from NVE Corporation, that have been coated with 500 nm of amorphous Si_3N_4 to increase their resistivity and avoid current shunting. Prior to all three processing steps, they are cleaned with an acetone/methanol/isopropanol rinse and baked at 180° C to remove trace water molecules. After fabrication of the macroscale contacts, but before patterning the magnetic structures, the wafer is diced to 10 mm × 10 mm. To do this, we first coat the entire wafer in a layer of Microposit 1800 series photoresist for protection and then make the cuts with a Disco 2D/6HT diamond blade wafer saw. Individual chips can then be re-cleaned using the above recipe to prepare them for subsequent processes.

3.1.6 Lithography

The three deposition steps that are required to fabricate our samples all require a lithographic mask. For the first step we use a photolithographic process to define coarse features down to 20 µm on a side. Our process uses a bilayer resist with a sacrificial base layer of polydimethylglutarimide (PMGI) followed by a layer of Microposit 1800 series photoresist. If a pattern is then defined in the 1800 series resist, the PMGI can be developed separately to form the same pattern, but with a slight undercut for good

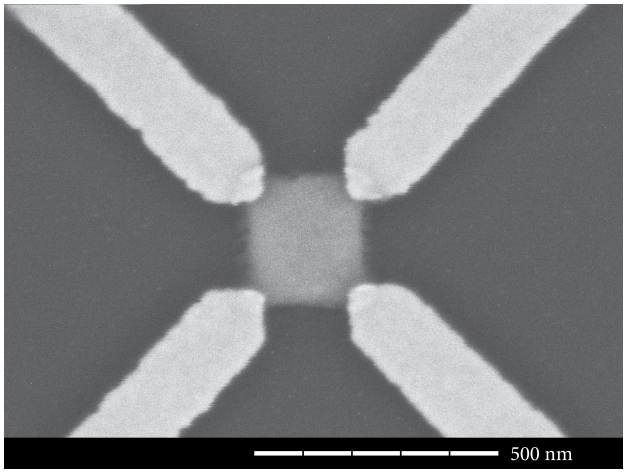

Figure 3.5: Scanning electron micrograph of dot and contacts showing limits of resolution for a 250 nm sample. Image taken with Hitachi S-4700 SEM at UMN Characterization Facility.

film liftoff. Film exposure is performed in a Karl Suss MA-6 contact aligner, which uses a 350 W mercury lamp ($\lambda \approx 350\,\text{nm} - 450\,\text{nm}$) to selectively expose the resist through a chrome mask.

Defining structures at length scales smaller than the wavelength of UV light requires electron beam lithography. To do this, we use a 100 kV EBPG-5000 system built by Vistec that can define features down to ∼5nm (see Fig. 3.5). Our resist is polymethylmethylacrylate (PMMA) that is dissolved in chlorobenzene before being spun onto the substrate. Typical resist thicknesses are on the order of 100nm, which should be at least 3-4 times thicker than the film being deposited for good liftoff. Thicker films can be accommodated either by altering the solvent concentration to make a thicker resist, or by adding an underlayer such as PMGI. It should be noted that adding a PMGI layer will decrease the resolution of the PMMA slightly because the extra development step adds stress to the PMMA film. For this study, we found that we were able to make optimal features with a single layer of PMMA.

3.1.7 Deposition methods

Two primary methods are available for deposition of metals and they have different limitations related to attainable resolution and the range of materials that can be applied.

Evaporative methods work by heating a source material until individual molecules are vaporized and adsorb to the substrate. The heating can either be accomplished by an electron beam or by Joule heating of a tungsten crucible. As a line-of-sight deposition process, evaporation can give very high spatial resolution and good control of film thickness, but it also has two major drawbacks. First, it is very difficult to accurately deposit alloyed source material because the constituent metals will have different melting temperatures and will therefore deposit at different rates. This means that the deposited film will have a different stoichiometry than the original source and, with time, the concentration of the source will also change as different components are depleted. One can avoid this issue by having a co-deposition system that heats multiple pure elements simultaneously, but for this experiment, we did not have access to such a system. The second drawback to evaporative processing is that metals with very high sublimation temperatures such as molybdenum or tantalum give drastically reduced resolution because molecules coming off of the source have kinetic energy high enough to damage or penetrate resist when they impact the sample substrate.

The second method of deposition, sputtering, uses low pressure argon gas to facilitate sublimation of the source material. In a sputtering system, a high voltage is applied between a cathode and the source material in order to ionize the argon molecules. The resulting plasma is then contained magnetically by permanent magnets and the positive argon ions are accelerated into the source with enough kinetic energy to knock out molecules of the source material, which can then adsorb onto a sample substrate. Because sputtering relies on impact-assisted sublimation, it avoids the problem of depositing alloyed source material since different sublimation temperatures will not affect the sputtering rate of the constituent materials. In addition, it is possible to deposit hard materials without sacrificing resolution because, although an individual molecule will have a very high kinetic energy when it leaves the source, it will thermalize with the gas before it impacts the substrate. This thermalization, however, does not come without cost. The reduced mean free path in the deposition chamber means that sputtering is a conformal, rather than line-of-sight process and the resulting film will either have decreased resolution or fencing edges if it is deposited on top of a resist layer (see Fig. 3.6).

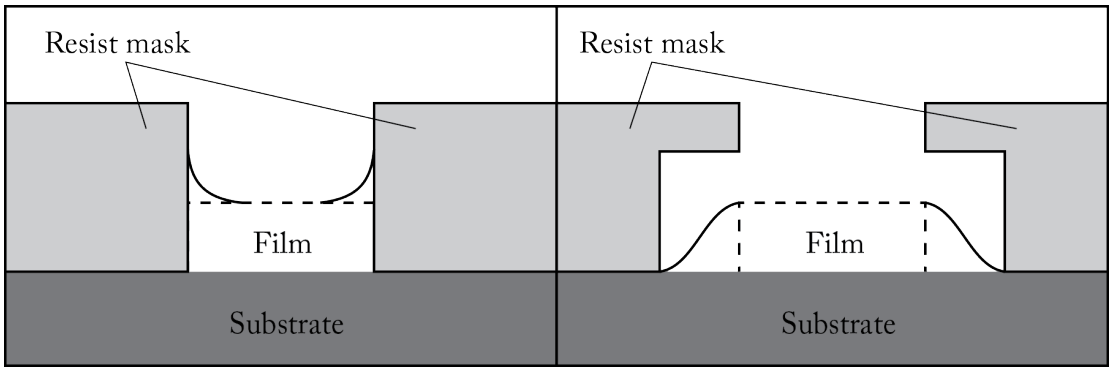

Figure 3.6: Artifacts of sputter coating. For a monolayer resist (left), conformal coating creates fencing at edges of pattern, while a bilayer resist (right) will result in overspray edges. In both cases, the dotted outline designates the ideal pattern to be deposited.

For this project, sputtering was used for the magnetic structures and W/Au contacts. Electron beam evaporation was used for Ti/Au contacts. In all cases a single layer of PMMA was used to define the mask. In previous studies, a bilayer stack of PMGI/PMMA has been used,[37] but we have found this gives suboptimal resolution of the magnetic structures. Our process does give a certain amount of fencing that can cause the magnetization to form intermediate states, which we interpret as vortices (see Fig. 3.8). To avoid these fencing vortices, we mill the magnetic structures post-deposition, using an Intlvac Nanoquest ion mill system at a 15° angle relative to the substrate. This removes the fencing edges, leaving a clean square structure.

3.2 Experimental setup

Our experiment relies on observing changes in the angle of the net magnetic moment as a function of applied external field and thermal noise. Accordingly, we need methods of controlling the sample temperature, as well as the magnitude and angle of our applied field. The first of these is achieved by placing the sample in a 4 K refrigerator, which will be discussed in detail in section 3.4. The external magnetic field is provided by two electromagnets. The primary field is created with a Cenco 79637 electromagnet mounted on a rotary table. We have fabricated a set of iron cores that can be easily inserted without moving or disassembling the magnet to allow for both high fields (with the cores

inserted) and maximum field stability (with the cores removed). This electromagnet is powered by a Kepco 36V-6A bipolar amplifier that can be controlled by the experimental computer to allow for field sweeping. This electromagnet has a maximum field of 315 G without the cores and is used to control the height of the energy barrier. Our secondary electromagnet is a pair of ELWE Teknik coils that are attached directly to the vacuum shroud of the refrigerator by means of a Teflon yoke. These are mounted perpendicular to the field of the primary electromagnet and can be powered by both DC and AC currents. A DC current can be manually controlled with a Keithley 220 milliamp current source, which allows for much finer control over the angle of the net H_{DC} than is possible with the rotary table. At the same time we can source an AC current using a Pasco function generator, which allows us to provide the energy well modulation that is necessary to observe stochastic resonance.

We quantify the DC and AC fields through several different methods. Mounted internal to the primary electromagnet is a Bell 5080 gaussmeter. While this allows us to directly read the field (of the primary coil), it has two drawbacks. First, it is necessarily mounted off-center in order to have room for the refrigerator shroud and as a result, it will differ from the actual field by a constant scaling factor. Second, this gaussmeter has an ultimate resolution of 0.1 G and is typically only stable to within 0.2-0.3 G. Both of these are too large to precisely quantify the field. Instead, we track the approximate field with the gaussmeter and also measure the current in the coil directly with a reference resistor. This gives us much higher resolution and we can linearize the current reading so that it scales with the gaussmeter. This is necessary when using iron cores, because hysteresis effects will cause the field to be nonmonotonic in current, so the current alone is not a meaningful measurement.

The gaussmeter probe is mounted outside the secondary coils, so a current measurement is the only option to quantify the transverse field. We have manually calibrated the coils and found that they give $H_{DC} = 13$ G/A. At nonzero frequencies, there will be some inductive loss from eddy currents that are set up in the vacuum shroud and cold finger of the refrigerator. In this case, we are able to achieve $H_{AC} \lesssim 9$ G/A for a driving frequency of 100 Hz. This is an upper limit since the inductive loss from the cold finger will be temperature dependent.

We measure the average magnetization direction using a four-terminal resistance

technique. Because we are interested in a range of noise frequencies, we use a DC measurement instead of the more common AC resistance technique (see, for example, [46]). This does mean, however, that we are sensitive to outside interference and need to take care to reduce the noise in our experimental setup. Our current source is provided by a 1.5 V cell, in series with a load resistor (typically 5-15 kΩ). Our effective resistance of a sample in the configuration shown in Fig. 3.5 is ∼4 Ω and a typical measured AMR of such a sample is

$$\frac{\delta\rho}{\rho} = 2\%. \tag{3.1}$$

Combining all of these gives a change in resistance on the order of 10 µV, which is sent through two preamplifiers before measurement. Our initial stage amplifier is a Stanford Research 552 bipolar preamplifier that has an input noise of 1.5 nV/$\sqrt{\text{Hz}}$, and has been modified to be DC coupled and give a constant ×50 gain. The second stage amplifier is a Stanford Research 560, which has an input noise of 4.5 nV/$\sqrt{\text{Hz}}$, and can give anywhere from ×1 to ×10^4 gain, depending on the desired output voltage. This amplifier also has a set of digital filters that can be used to reduce the RMS voltage of the Johnson-Nyquist background noise (see 3.3.4). Both preamplifiers are battery powered to avoid 60 Hz noise from the power circuitry. Finally, the amplified and buffered signal can be digitized with any combination of digital voltmeter, storage oscilloscope, spectrum analyzer, or lock-in amplifier, depending on the specific measurement.

Typically, a Keithley 2000 digital voltmeter is used to take field sweeps and characterize the field-dependent magnetization since it has the dynamic resolution to capture the entire signal and see changes without needing to subtract the DC offset. All other instruments require some amount of AC coupling to avoid clipping the signal, and while it is possible to use the internal coupling, it limits the range of measurable signals since most instruments have a coupling frequency on the order of 10 Hz. It would be possible to use a resistance bridge to remove the DC offset without any frequency loss, but there is still the issue that the offset varies slightly with temperature. Instead, we have found that the best compromise is to insert a discrete first-order highpass filter with a 10 s time constant, post-amplification.

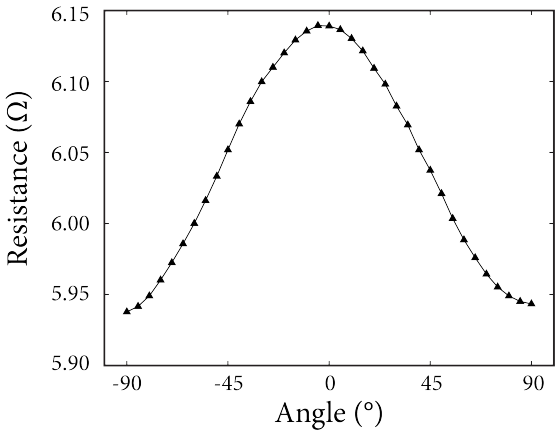

Figure 3.7: High field resistance at room temperature as a function of field angle. All data are taken with applied field of 300 Oe.

3.3 Characterization of magnetic domain structure

3.3.1 Anisotropic magnetoresistance measurement

When measuring magnetization indirectly with AMR, we perform a number of measurements to ensure consistency. The net AMR of our samples is approximately 2% at 300 K, which can be determined by applying a constant field at varying angles as shown in Fig. 3.7. At low temperature, the AMR ratio is enhanced since it is inversely proportional to the total resistance, which decreases with decreasing field. In addition, the absolute magnetization varies with temperature as[9]

$$\frac{\Delta M(T)}{M_s(0)} \propto -T^{3/2}, \tag{3.2}$$

which creates a slight enhancement of the AMR voltage. When these are combined, we observe an AMR up to 3.25% at $T < 50\,\mathrm{K}$. At all temperatures, however, the measured AMR for an RTN signal will be less than that of the high-field sweep since, under the conditions for RTN, the magnetization will not be switching between two fully orthogonal states. In addition, at low fields the magnetization will have some curving that reduces the net moment and lowers the AMR accordingly.

To characterize the energetics of our system, we can use field sweeps as shown in Fig. 3.8. The field sweep here was taken in the 90° direction and shows clear hysteresis.

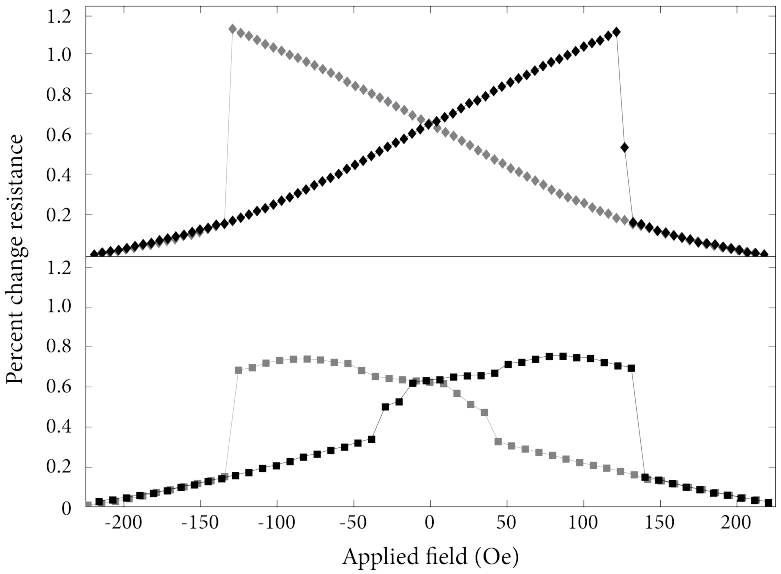

Figure 3.8: Field sweep in the 90° direction for a clean dot (top, diamonds) and a dot showing vortices (bottom, squares). Samples are 250 nm × 250 nm × 10 nm. In both cases, the initial trace is shown in black and the retrace is shown in gray. Direction of field sweep is from negative to positive field for initial trace.

Both sweeps are assumed to start at high fields with the sample in the buckle state from Fig. 3.3. As the field is reduced, the magnetization structure becomes more and more buckled, which is manifest as a reduction in the AMR signal (in the graphs shown, the net change in resistance is negative, so a reduction in AMR causes an increase in resistance). The data plotted with squares shows a transition at ±50 Oe (before crossing zero), which we attribute to switching into a vortex state. The sample plotted with diamonds does not show this, but rather continues to show greater and greater domain curvature until it reaches its ultimate coercivity near ±130 Oe. This represents the field at which the magnetostatic energy from configurational anisotropy is equivalent to the Zeeman energy of the applied field. This technique can be used to quantify the height of the energy barrier as in [37].

Both samples shown in Fig. 3.8 were measured at room temperature. Reducing the temperature has the effects of increasing the coercivity field and adding a secondary transition at high fields. We attribute the increase in coercivity primarily to reaching the condition where it is not enough to have $E_{\text{Zeeman}} = E_{\text{anisotropy}}$, since there is not

enough thermal energy to induce a transition to the global minimum if the initial state is still a slight local minimum. In this case, a more stringent criterium must be satisfied, namely

$$\frac{\partial^2 E_{\mathrm{Z}}}{\partial \phi^2} = -\frac{\partial^2 E_{\mathrm{ani}}}{\partial \phi^2}. \tag{3.3}$$

It should be noted that while the above quantities appear similar to the coefficients of curvature, $c_i^{(A,m)}$, from Eq. 2.28, we do not believe there is a simple relationship between the two since they may have qualitatively different magnetization structures. We believe that the observed high-field transition is a crossover from the flower state into the buckle state, which is consistent with micromagnetic simulations, as discussed below.

3.3.2 Comparison to simulation

We have performed simulations of field sweeps to confirm the magnetic behavior seen in our dots. All simulations were made using LLG-v2 Micromagnetics software on a 250 nm $\times$ 250 nm $\times$ 10 nm square of permalloy. The cell size used for simulation was 5 nm, which is comparable to the accepted exchange length for permalloy. Magnetoresistance was calculated with a 100 µA current that entered and exited the sample from adjacent corners. While this current mimics the real scenario, the induced voltage does not, since it is calculated by integrating the resistivity from source to drain (two-terminal). By contrast, our samples measure the voltage nonlocally by contacting the two unused corners of the dot. It is possible that this gives a qualitatively different resistance curve due to the effect of the magnetization structure, but this is assumed to be a small effect that will not alter the basic structure of the magnetoresistance curve.

At zero temperature, a sweep parallel to one of the edges shows similar hysteresis and AMR to our low-temperature measurements as shown in Fig. 3.9 and Fig. 3.10. The transitions from buckle to flower state in Fig. 3.9 that occur between (a)$\rightarrow$(b) and between (c)$\rightarrow$(d) are notable because they imply that the buckle state is a more stable minimum at low fields. Our measured samples show similar switches, though with the secondary transition occurring at a higher relative field. At higher temperatures, as in the inset of Fig. 3.10 or Fig. 3.8, we do not see this transition. This could either be because the flower state is no longer stable above certain temperatures, or because

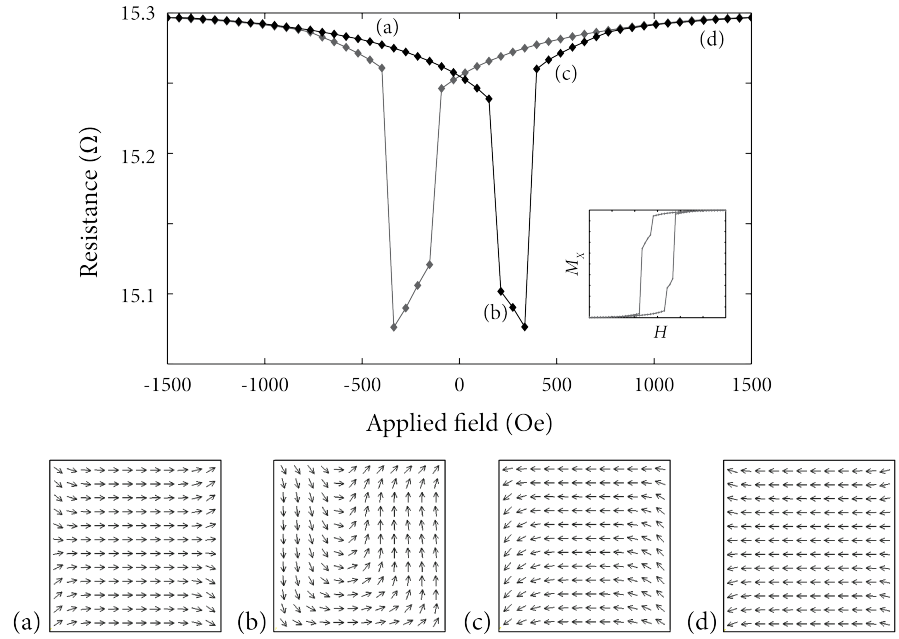

Figure 3.9: Simulated magnetoresistance for a field sweep in the 0° direction. (a)-(d) show magnetic structure at the marked location in the hysteresis loop. Inset shows hysteresis loop for x component of magnetization. Primary transition between (b) and (c) occurs by nucleating a vortex, which then propagates across the dot. This transition is expected to occur on a very short timescale (nanoseconds). Direction of field sweep is from negative to positive for pictured domains.

thermal fluctuations wash out the sharp transition between the two states so that it is not visible on a magnetoresistance plot.

For a field applied at an oblique angle, a new state is obtained as shown in Fig. 3.11. We will refer to this as the S state magnetization. Note that while this state is similar to the leaf configuration at the edges of the dot, it is not similar near the middle, where the net magnetization prefers to lie parallel to one of the edge. Most importantly, the S state is not symmetric with respect to the 45° direction, so it is possible to detect hopping between two different orientations of the S state with a magnetoresistance measurement. This is easily seen by sweeping the field primarily along the 45° direction, but with a small transverse component, such that the total field becomes slightly elliptical as in Fig. 3.12. The transverse field will then break the symmetry of the problem so that the magnetization picks different configurations of the S state along the trace and retrace

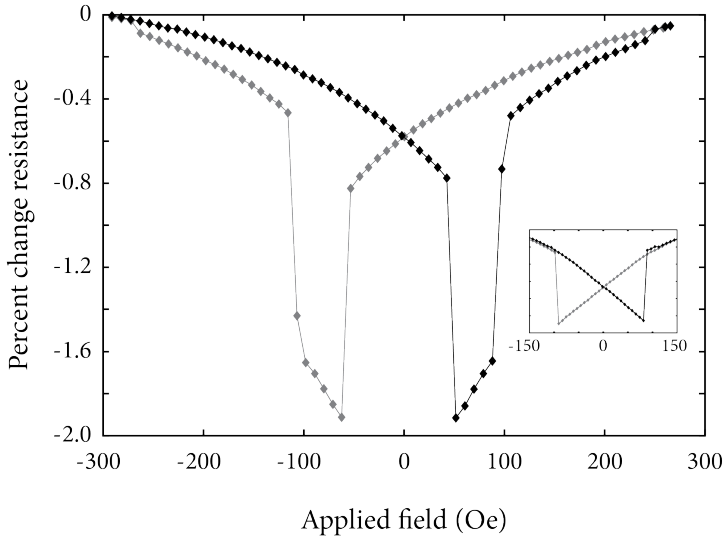

Figure 3.10: Measured magnetoresistance for a field sweep in the 0° direction at 60 K. Inset shows the same sample at room temperature. Initial trace (negative to positive) plotted in black with retrace plotted in gray.

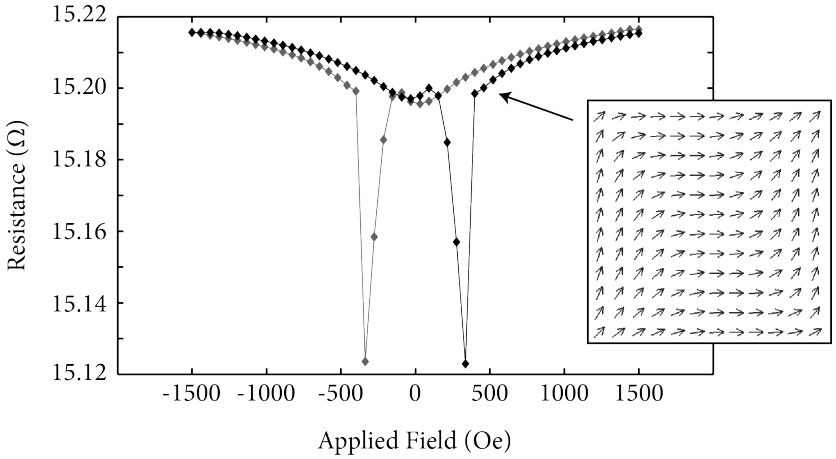

Figure 3.11: Simulated magnetoresistance for a field sweep in the 30° direction. At low fields the magnetization structure moves from a leaf state to the S state depicted.

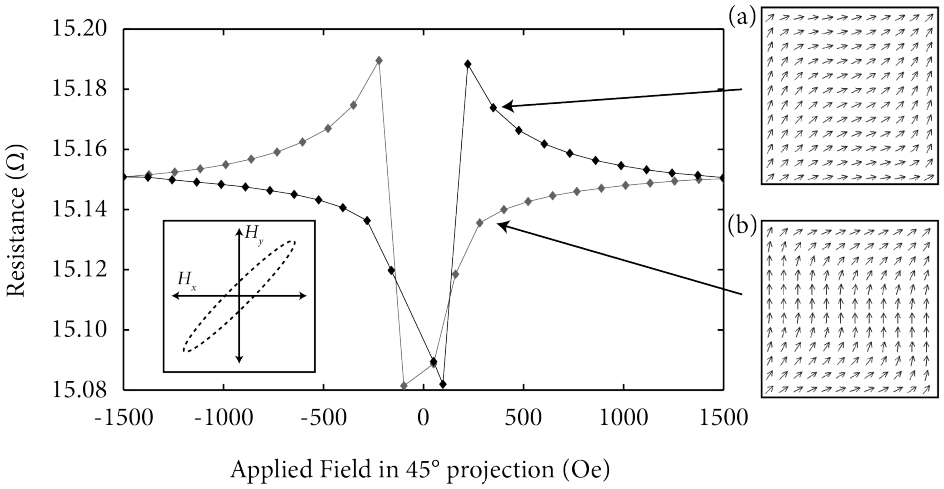

Figure 3.12: Simulated magnetoresistance for an elliptical field sweep where the primary axis is along the in the 45° direction. (a) and (b) show the bistable leaf states where (a) corresponds to the initial trace (field negative to positive) and (b) occurs on the retrace. Total applied field vector is plotted in inset.

direction, with correspondingly different values of magnetoresistance. In order to see RTN, therefore, we can apply a field along the 45° direction to control the barrier height, and then adjust the temperature until there is enough thermal energy present to induce magnetic transitions between the two bistable S states.

3.3.3 Measurement of RTN

With appropriate tuning of the applied field and temperature, it is possible to reach a state where the magnetization switches randomly between two states (assumed from simulation to be S type) at a constant value of applied field as shown in Fig. 3.13. This typically occurs with the field applied near the 45° direction, but this can vary widely, particularly at room temperature where we have seen samples that exhibit noise with the field applied at angles as wide as 30° or 60°. The range of angles over which noise is observable is typically large at room temperature (5°-10°) and narrows with decreasing temperature. At low temperatures the range of angles that produce noise is exceptionally narrow—a few arcminutes at 30 K—and requires the use of the secondary field coil to adequately tune the field. This is a reflection of the fact that the exponent in the Arrhenius law contains a factor of T^{-1}. For small angular changes $\delta\phi$, the depth

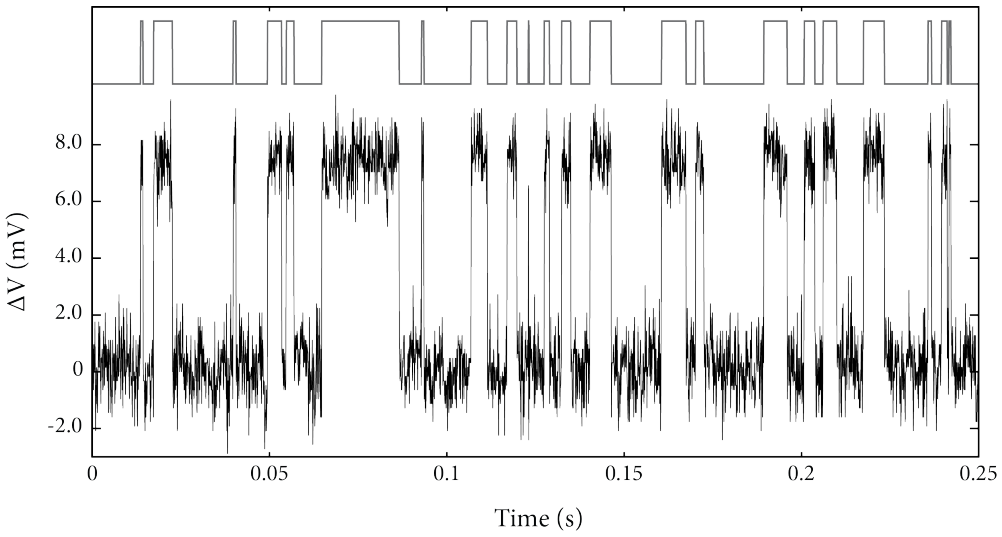

Figure 3.13: Raw data (bottom) and reconstructed trace (top, not to scale) showing two-level RTN caused by magnetic transitions at a constant field. Plotted data represent approximately one tenth of total record length for a single trace.

of the well goes as $\Delta E = \Delta E_0 - \delta\phi MH \sin\alpha$, where α is the angle between the well minimum and the applied field. The relationship between switching frequency and a change in well depth is given by

$$\frac{\partial f}{\partial \Delta E} = \frac{f_0}{T} e^{\Delta E/T}. \tag{3.4}$$

For a given change in angle $\delta\phi$, therefore, the relative change in frequency dies off as $1/T$. In addition, higher temperatures require a higher energy barrier to balance the thermal energies and produce noise at a measurable frequency. This equates to a lower magnitude of applied field, which will reduce the change in energy for a given change in angle. For the same reason, the range of field magnitudes that will produce noise is wide at room temperature and narrows in the cryogenic regime. Typically we can see noise in the range of 30-60 Oe at 300 K and near 100 Oe at 30 K

The trace shown in Fig. 3.13 has two main noise components: an 8 mV RTN signal and a $\sim$2 mV white noise background. Of these, only the first is of interest for our study, so we filter the broad-spectrum noise from the signal before measuring transition times. This can be done to a certain extent with a scanning lowpass filter, but this has

the undesirable effect of decreasing the slope of transitions and attenuating transitions with very short dwell times. A better solution is to use a bilateral filter that preserves peaks and edges by weighting each nearby point according to how close its measured value is to that of the point in question:

$$V_{\text{filt}}(t) = \frac{1}{\tilde{N}} \sum_i V_i w_i \exp\left\{-\frac{(t_i - t)^2}{\tau_m^2}\right\}, \tag{3.5}$$

where τ_m is the maximum timespan for filtering, w_i is a weight function, and $\tilde{N}$ is a normalization constant. With $w_i \equiv 1$, this reduces to a standard lowpass filter with cutoff frequency $1/\tau_m$. In order to preserve edges, we can set the weight function to a Gaussian such as $w_i = \exp\{-[V(x_i) - V(x)]^2/\tilde{V}^2\}$ where $\tilde{V}$ is the RMS value of the voltage noise. With this, samples that are far away in voltage are assumed to be part of a transition and do not count toward the sum.

After filtering, the data are reconstructed using one of two algorithms. (Note: data processing algorithms are discussed in detail in appendix A.) For relatively clean data such as those shown in Fig. 3.13, we can use a digital comparator that assigns a state according to some threshold voltage. For data with a longer characteristic time, however, this does not work because the highpass filter used to block the DC component of

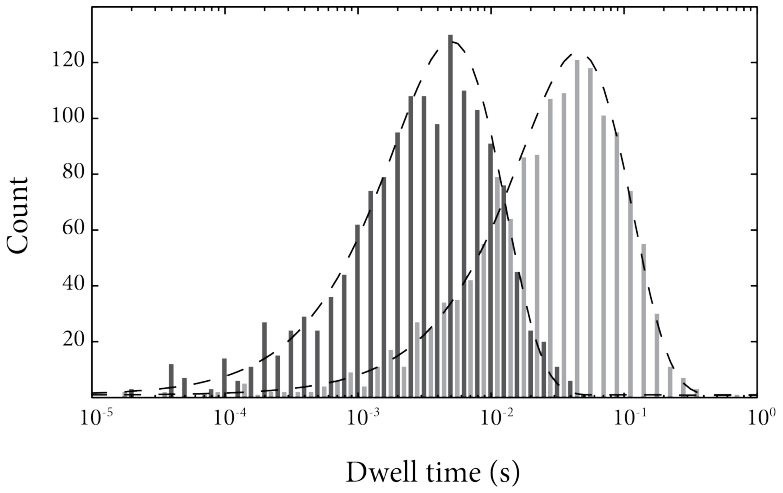

Figure 3.14: Histogram of dwell times for high-resistance state (dark) and low-resistance state (light). Data are taken from 50 traces at constant field and temperature. Dashed lines show fit to a Poisson distribution.

voltage will distort the trace and trigger false transitions. In this case we use a more sophisticated algorithm that looks for peaks in the first time derivative. This method is more robust at the cost of computer time. Once the trace has been reconstructed, we can extract the dwell time for individual transitions. The probability density function of these dwell times should follow a Poisson distribution as shown in Fig. 3.14. Following standard statistics, we can then say that the characteristic time, τ_0 is just the mean of all the times τ_i, and the uncertainty in that characteristic time is given by

$$\sigma_\tau = \frac{\tau_0}{\sqrt{N}}, \tag{3.6}$$

where N is the number of transitions measured under identical conditions.

3.3.4 Frequency limitations

RTN should, in theory, exist at frequencies all the way up to that of the Arrhenius prefactor. In our setup, however, Johnson-Nyquist noise provides a fundamental limit that prevents us from measuring noise above a few hundred kilohertz. In order to reliably distinguish RTN signal from background noise, we require that

$$\Delta V_{RTN} \geq v_J, \tag{3.7}$$

where v_J is the RMS voltage of the background noise. This voltage is related to the maximum bandwidth through Nyquist's equation:[2]

$$v_J = \sqrt{4k_B T R \Delta f}. \tag{3.8}$$

Equation 3.8 indicates that in order to measure an RTN signal with a given ΔV_{RTN} it is necessary to send the measured voltage through a lowpass filter to limit Δf such that Eq. 3.7 is satisfied. The power spectral density of the Johnson-Nyquist noise for our setup is typically 2 nV/$\sqrt{\text{Hz}}$ at 100K. This, combined with a value of $\Delta V_{RTN} \approx 10$ mV at $I = 200\,\mu$A, results in a maximum theoretical bandwidth of 25 MHz. In practice, however, this is rarely achieved as other effects tend to limit the highest measurable frequency.

The above analysis assumes that a nonlinear filter is able to reduce the noise in processing and distinguish transitions from momentary noise spikes. At frequencies near

the maximum bandwidth, however, this is not possible since a transition can happen on the same timescale as a noise fluctuation. In this case, Eq. 3.7 is no longer sufficient and we instead require that

$$\Delta V_{RTN} \geq v_P, \tag{3.9}$$

where v_P is the *peak* voltage of the background noise. This peak voltage will be much larger than v_J. The ratio v_P/v_J for white noise is a function of measurement time since v_P can reach arbitrarily large values if one waits long enough,[47] but it is typical to use a factor of

$$v_P = 3.3 \times v_J, \tag{3.10}$$

which will be valid for 99.9% of measurements. (This follows from the fact that white noise has a Gaussian distribution.) Furthermore, higher frequencies must be present to distinguish a clean transition because a square wave has higher harmonics, which die off as $1/f^2$. Truncating these higher frequencies will result in a signal with rounded transitions that cannot be digitized. If we combine these two limitations, we come up with a frequency limit that is 10-100 times smaller than our original estimate for the maximum bandwidth.

Finally, when performing a temperature sweep, it is natural for the duty factor of the RTN signal to shift if the two wells do not have equal depths. This can be problematic at high frequencies because the maximum measurable duty factor is limited by the trace length of the oscilloscope. If the duty factor has shifted to the extent that it is no longer possible to record several cycles while still ensuring that the higher frequency state lasts at least as long as a single time bin, the RTN cannot be digitized.

3.4 Low temperature techniques

3.4.1 Thermal mounting

Low temperature measurements were made in a Advanced Research Systems Inc. 4 K closed-cycle helium refrigerator. It was originally designed to mount a sample in the vertical plane, which gives the user control over an out-of-plane magnetic field. For our experiment, however, we care about the angle of an in-plane field. In order to have this control, we fabricated a mounting block out of copper that allows the sample to be held

horizontal with respect to the applied field. The mounting block was intentionally made as large ($\sim 1\,\mathrm{cm}^3$) as was reasonable within the confines of the refrigerator shroud, in order to maximize the thermal mass and increase thermal stability. It does not contact the cold finger directly, but is instead thermally linked via six copper braids that are approximately 2 cm long and have a cross-sectional area of $1\,\mathrm{mm}^2$. These braids are clamped to the block but can be detached in order to remove the block for sample mounting and wire bonding. With this arrangement we have a measured thermal lag of

$$\eta \approx 0.1 \frac{\Delta T}{\text{minute}}, \tag{3.11}$$

where η is the temperature ramp rate and ΔT is the constant temperature offset between the cold finger and mounting block.

3.4.2 Thermometry

The cold finger of our refrigerator has two separate thermometers for measuring temperature. The first thermometer is a calibrated GaAlAs diode that is thermally anchored to the cold head near the heater and is used to control the heater PID. The second thermometer is a calibrated Cernox resistor that is clamped to the sample mounting block with a layer of Apiezon-N grease and is used to record the sample temperature for measurements. There is always some uncertainty as to how closely the sample thermometer matches the true sample temperature (the sample thermometer can lag behind the control thermometer by several Kelvin during a temperature sweep) and we have therefore used the four-terminal sample witness as an on-chip reference to assess the validity of our temperature measurement. This witness resistor is a $75\,\mu\mathrm{m} \times 900\,\mu\mathrm{m}$ thin film that is patterned on-chip with the same materials as the microvias. When we monitor the resistance of this film and compare it to the sample thermometer reading, we see a linear relation as expected.[48] More critically, we observe no measurable hysteresis in the resistance measurement up to our highest rates of temperature ramping. This indicates that the thermal anchoring is good enough between the mounting block and the sample substrate to consider the recorded temperature equal to the actual sample temperature.

3.5 Grounding

As with any small-signal measurement, proper grounding and shielding are critical to maintaining signal integrity and minimizing interference from outside sources. Ideally, the ground used for the circuit and shielding should be isolated from any noise sources or outside power interference (such as large power supplies). In addition, there should be a single current path from any one point in the setup to ground so as to eliminate the possibility of inductive pickup via ground loops. In practice, however, these two conditions cannot always be met, so we have done work optimizing the grounding process to minimize the amount of extraneous noise measured.

The master ground for our setup is provided via instrument grounds in our laboratory. These are dedicated hookups that are independently connected via AWG-000 cable to a busbar on the floor level and from there, directly into the Ufer ground for the building. This busbar is isolated from the main power grounds and should therefore not have cross-contamination from high-current loads in other laboratories.

From the instrument ground receptacle, the ground is hardwired into a power strip on the instrumentation rack that provides power for all equipment except the power supply for the magnet and the closed-cycle refrigerator. The closed-cycle refrigerator would normally have a chassis ground that is supplied by its own power cable. This chassis ground provides the most critical shielding in the setup via the shrouds on the cold finger of the refrigerator. Because the compressor requires 208 V, single-phase power, however, it cannot be plugged directly into the same power strip as the rest of the instrumentation and needs to be run on "dirty" power. In order to avoid contaminating the grounds for the shielding, the compressor was therefore modified to take its ground directly from the instrument receptacle via a hardwired link rather than the main power cable.

Once ground has been supplied for instrumentation through the power strip, it is connected to the shields of all wiring. For this experiment, all connections are made with low-noise cabling such as Belden Beldfoil twisted-pair audio cable or Times AA-2992 coaxial cable. Care was taken to ensure that there were no ground loops in the shielding. This ground was also connected to the negative terminal of the first-stage preamplifier at the final cable connecting the preamplifier to the breakout box. In this way, the

negative terminal of the preamplifier as well as the circuit shields have grounds that are as close in potential as possible to provide optimum ballasting by the preamplifier. In addition to the cabling shields, a dedicated connection was provided from the circuit ground to the chassis of the closed-cycle refrigerator. While this does create a ground loop (since the refrigerator chassis is already grounded through its connection to the compressor), our tests have shown that the inductive pickup of this ground loop is negligible compared to the noise caused by having the circuit and refrigerator chassis at slightly different ground potentials.

In order to save data, some connection to a computer is required. This was made via USB connections for the oscilloscope and temperature controller and IEEE-488.2 GPIB interface (through a National Instruments GPIB/USB converter) for all other instruments. This connection will feed extraneous noise into the system from two sources: the contaminated computer ground and intrinsic noise generated inside the computer. Particularly egregious are 60 Hz and harmonics that can be attributed to the computer's power supply unit. In order to shield the system from these issues, a B&B electronics UHR304 USB isolation hub was used in line between the computer and instrumentation. With the above recipe, the only noise observable on a 150 Ω test resistor up to 100 kHz was the combined Johnson-Nyquist noise of the resistor and preamplifier.

Chapter 4

Results

4.1 Activated switching behavior

The RTN in our samples shows strong Arrhenius switching behavior across the broad range of temperatures and applied magnetic fields where RTN is observed. Fig. 4.1 shows an example of this behavior, with $f_{A,B}$ plotted as a function of $1/T$ for the two states A and B of the RTN oscillator. The data shown were taken with a constant applied field H_{DC} and no AC field. It is possible to extract an attempt frequency and well depth for the two wells by plotting the frequencies on a logarithmic scale and fitting them to the linear function

$$\log(f_{A,B}) = \log(f_0) + \Delta E \times (k_B T)^{-1}. \tag{4.1}$$

In this configuration, the well depth and attempt frequency correspond to the slope and y-intercept of the fit line, respectively.

Previous studies[10,12,14–16] have seen temperature-dependent, activated RTN behavior in magnetic structures, but none have separated the switching parameters for the two directions $A \to B$ and $B \to A$. In addition, there have been few attempts[16] to probe the attempt frequency f_0. It is most common to approximate the attempt frequency as 10^{10} Hz for all samples.[25] Section 5.1 will discuss the validity of this approximation.

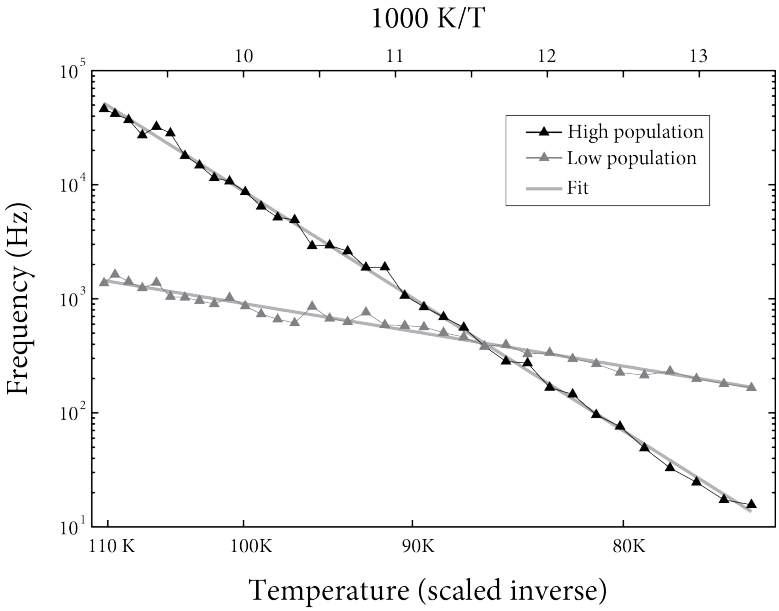

Figure 4.1: Switching frequency for high resistance state (black) and low resistance state (gray) as a function of inverse temperature. Data were taken with an applied field in the 45° direction of 113.6 Oe. Fit lines correspond to an attempt frequency of 2.2 THz and well depth of 166 meV for the high state, and an attempt frequency of 140 kHz and well depth of 43 meV for the low state.

4.2 Observation of stochastic resonance

In order to observe stochastic resonance, we apply an AC transverse field and vary the temperature so that the characteristic Arrhenius time passes through the condition $2f_A = \omega_D$. For this study, we have used a constant $\omega_D/2\pi$ =100 Hz, because this frequency is low enough that H_{AC} is not too heavily attenuated by the copper radiation shroud on the refrigerator, but remains high enough to allow for good quality measurements with a lock-in amplifier.

We expect the returned signal to be dependent on the ZDA, which will itself be a function of the duty cycle

$$\mathcal{D} = \frac{\tau_H}{\tau_H + \tau_L}, \tag{4.2}$$

where τ_H and τ_L are the characteristic dwell times for the high-resistance and low-resistance states. (For our results, we will use the subscripts H and L, rather than the

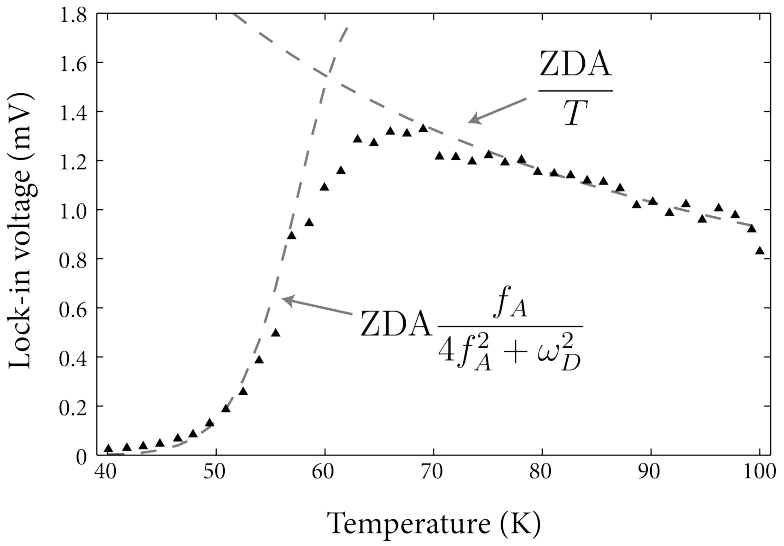

Figure 4.2: Amplitude of stochastic resonance signal. Dashed lines show fits to the two parts of Eq. 2.40, and the temperature regime for which each dominates.

equivalent markers A and B, when we wish to keep track of the orientation of the two states relative to 0°. In cases where $\mathcal{D} = 0.5$ and the two are equal, we will continue to use the subscript A.) It is typical for the duty cycle to shift as the temperature is varied, which can create false effects in a stochastic resonance measurement. To avoid this, we make small adjustments to the DC transverse field, so that the sample remains in a 50% duty cycle throughout the entire sweep. These adjustments are typically on the order of 100 mG, which equates to an effective rotation of the total $\mathbf{H}_{DC}$ of ~ 3.7 arcmin, and is within the range for which we have seen the attempt frequency to be effectively constant.

The amplitude of the signal at ω_D is shown in Fig. 4.2. It includes all of the hallmarks of stochastic resonance, such as a strong maximum in $d\mathscr{M}/dT$ near 55 K, a broad maximum in $\mathscr{M}(T)$ near 65 K and a gradual die-off at high temperature that follows a $1/T$ dependence. Near the maximum, there is a qualitative change in the magnetoresistance signal $R(t)$ as it changes from a purely stochastic signal with random residence times to a phase-locked signal as shown in Fig. 4.3.

Prior to this study, stochastic resonance has only been observed in a few magnetic

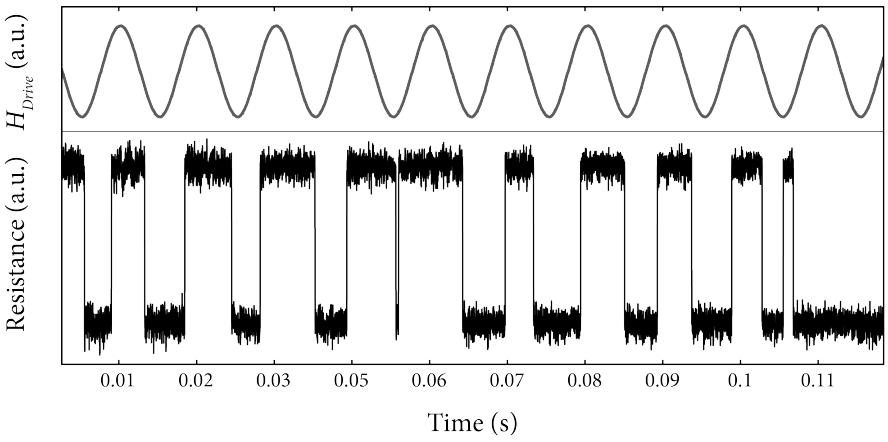

Figure 4.3: Transverse magnetic field (top) and resistance (bottom) as a function of time. Primary magnetic field of 130 Oe is tuned such that $2f_{H,L} \approx \omega_D$ at measurement temperature (300 K). This allows the system to lock the phase of the magnetic transitions to the phase of the driving field. Phase lag is approximately $\pi/4$ between field and magnetic signals.

systems. It was first seen in ferrite-garnet films with magnetic field noise that was generated externally using a current noise source and Helmholtz coil.[49] Later work[50] used the same experimental configuration, but with the noise provided by thermal fluctuations. Recently, it has been observed in iron nanoparticles[51] and spin-torque driven oscillators.[52,53] A common trait of these studies is that they observe stochastic resonance primarily as a series of peaks in a histogram of dwell times at odd multiples of π/ω_D. Only one study[52] observed a peak in the amplitude with changing temperature similar to that of Fig. 4.2.

It is not straightforward to translate our transverse field—AC or DC—into an energy modulation. This is because the approximation that M is constant breaks down in the regime of noise. Under these conditions, the magnetization is strongly curved and it is likely that a change in applied field only slightly modifies the total energy. To be clear, we do believe that assuming a constant M can give the correct form for $\delta E(H)$. To first order, it is only the magnitude of $\partial E/\partial H$ that is incorrect. As an example, we commonly drive our AC field at $H_{AC} = 100$ mOe$_{pp}$. If the sample were uniformly magnetized, this would correspond to an energy modulation of 260 meV, a result which is clearly incorrect, given that our samples typically have well depths that are <200 meV as

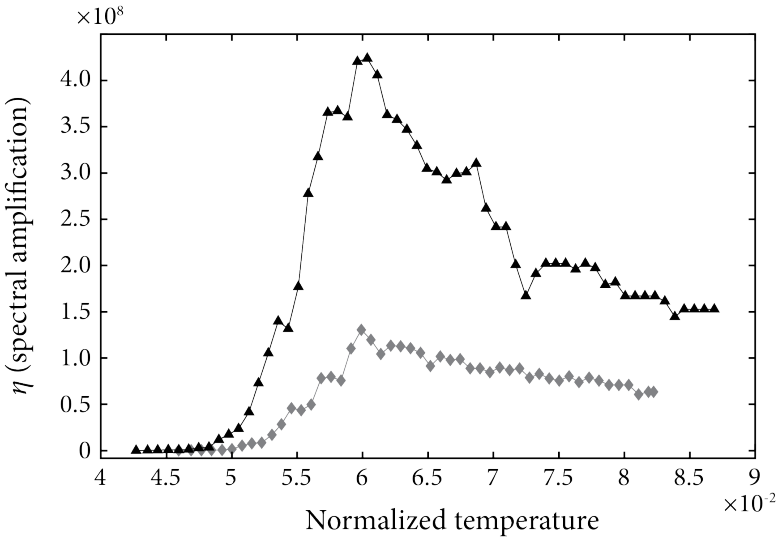

Figure 4.4: Spectral amplification η as a function of normalized temperature $T/\Delta V$, where ΔV is the depth of the well. Sweeps were taken on the same sample with a drive field of 300 mOe (diamonds) and 150 mOe (triangles). This particular sample was measured with a drive frequency of 4.78 Hz, which can account for the relatively large amount of noise in $\mathscr{M}(T)$ since the stability of the measured AC signal is limited by the time constant of the lock-in amplifier and the temperature ramp rate.

measured with an Arrhenius fit. A better model is to consider the angular modulation of the field. The 45° DC field necessary to induce RTN is around 90 Oe for temperatures below 100 K. This means that an AC field of 100 mOe is creating a net rotation of 3.7 arcmin in the applied field.

Without knowing the exact $\partial E/\partial H$ for well modulation, it is still possible to compare different magnitudes of H_{AC}. We define the unitless spectral amplification η as

$$\eta \equiv \left(\frac{\mathscr{M}(\omega_D, T)}{H_{AC}}\right)^2 = \left[\left(\frac{dV}{dM}\right)^{-1} \frac{V_{\text{LIA}}}{H_{AC}}\right]^2, \tag{4.3}$$

where V_{LIA} is the voltage measured by the lock-in amplifier and dV/dM can be estimated from field sweep data. The measured spectral amplification is plotted in Fig. 4.4 for the same sample with two different driving fields. We observe a reduction in spectral amplification at higher values of H_{AC}, which is consistent with theoretical predictions[54] and numerical simulation.[55]

4.2.1 Broad spectrum noise

The ultimate source of stochastic resonance signals, and RTN in general, are thermal fluctuations in the magnetization. Like their electric analog, Johnson-Nyquist noise, magnetic noise fluctuations are proportional to T, and they depend on the physical properties of the magnet. It can be shown[8,56] that the voltage noise power spectral density associated with magnetic fluctuations goes as

$$S_V^{(\mathrm{M})} = \left(\frac{dV}{dH}\right)^2 \frac{4k_B T\alpha}{\gamma M_s v}, \tag{4.4}$$

where v is the volume of the sample and α is the Gilbert damping parameter, e.g., $\alpha \approx 0.01$ for a 10 nm thick permalloy film capped with tantalum.[57] This noise is only white in the low frequency limit $\omega \ll \omega_{\mathrm{FMR}}$, but it is still common within the stochastic resonance community to define a signal-to-noise ratio (SNR) such that

$$\mathrm{SNR} = S_V(\omega_D)/S_V^{(\mathrm{M})}, \tag{4.5}$$

where $S_V(\omega)$ is the measured power spectral density of the driven system ($S_V^{(\mathrm{M})}$ is assumed to be measured under zero-drive conditions at a high enough frequency that $S_V^{(\mathrm{M})} \gg S_V^{(\mathrm{RTN})}$). The first term in Eq. 4.5 is simple to measure with a spectrum analyzer, as shown in Fig. 4.5. As the temperature is increased and the characteristic frequency $f_{H,L}$ moves through the driving frequency, a prominent peak is seen at 100 Hz, the height of which defines $S_V(\omega_D)$. Unfortunately, there is no way to directly measure the white noise $S_V^{(\mathrm{M})}$ within our setup. Using an estimated value of $dV/dH = 40\,\mu\mathrm{V/Oe}$ from field sweep measurements gives an expected white noise magnitude of 5×10^{-20} V^2/Hz at 100 K from fluctuations in the magnetization. By comparison, the nonmagnetic Johnson-Nyquist noise from our 200 Ω contacts is 1×10^{-18} V^2/Hz at the same temperature, so any measurement of the white noise spectrum in our setup is entirely dominated by Johnson-Nyquist fluctuations. To get around this, other groups have increased the factor dV/dH by using a spin-valve configuration[8] so that the noise fluctuations are visible above the Johnson-Nyquist floor. This is a possible direction of future research.

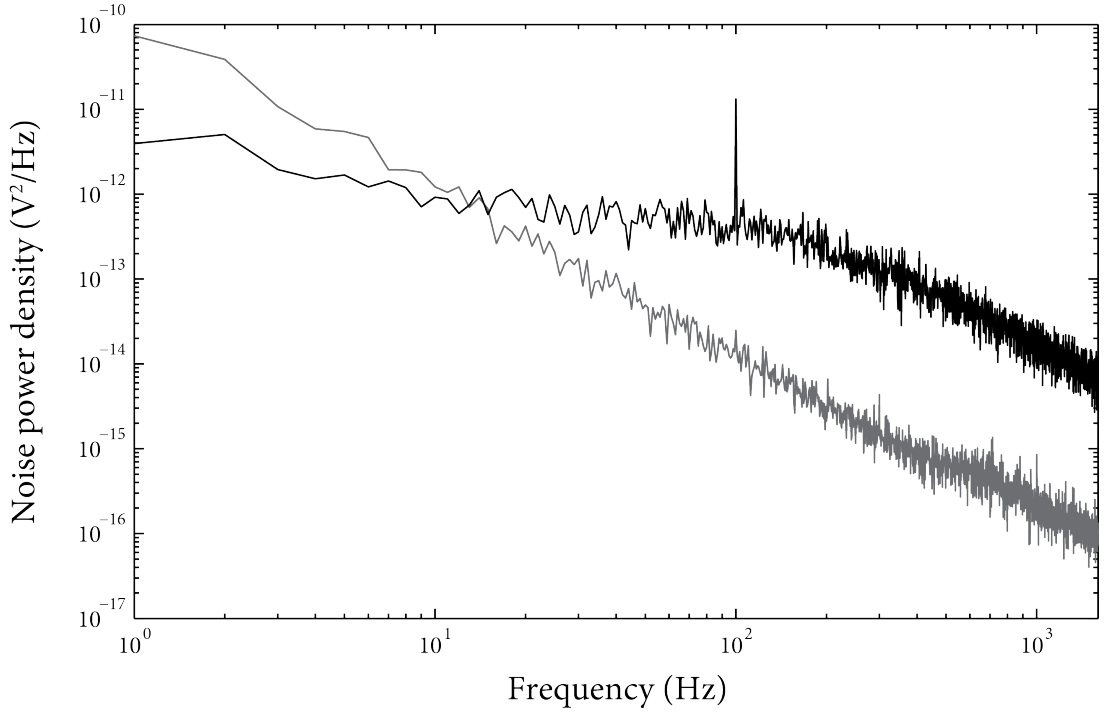

Figure 4.5: Voltage power spectral density for sample at low temperature (grey) and near resonance condition (black). In both cases, the high-frequency rolloff follows a $1/f^2$ spectrum. At low temperatures noise is almost entirely stochastic, with a smooth spectrum. At resonance, a large peak is seen at $\omega_D/2\pi$.

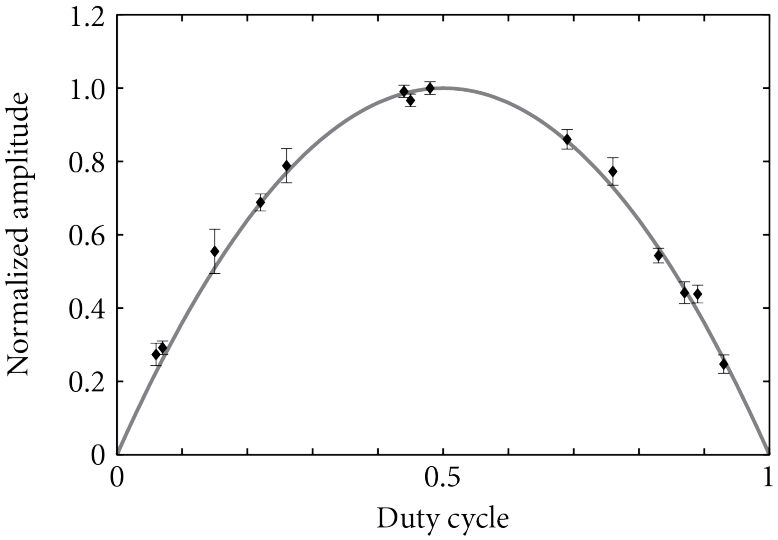

Figure 4.6: Stochastic resonance amplitude $\mathscr{M}(\omega_D)$ as a function of duty cycle $\mathcal{D}$ at conditions for resonance. Gray line shows fit to Eq. 4.6.

4.2.2 Effects of duty cycle on phase locking

As stated earlier, the prefactor ZDA in the resonance amplitude should be dependent on the duty cycle. It is calculated by the expectation value of $|\mathbf{M} - \overline{\mathbf{M}}|$ where $\overline{\mathbf{M}}$ is the average value of $\mathbf{M}$. For an RTN signal, with the two states $\mathbf{M}_A$, $\mathbf{M}_B$, and the duty factor $\mathcal{D}$ as defined in Eq. 4.2, straightforward algebra (see appendix B) gives

$$\text{ZDA} = 2|\mathbf{M}_A - \mathbf{M}_B|(\mathcal{D} - \mathcal{D}^2). \tag{4.6}$$

The easiest method of checking Eq. 4.6 is to manually shift the duty cycle by applying a small transverse H_{DC}. The effects of this are plotted in Fig. 4.6, along with the prediction of Eq. 4.6. A note to make is that the different H_{DC} were applied at equal intervals of 25 mOe, but the measured points are not equally spaced in $\mathcal{D}$. We attribute a certain amount of this noise to stray fields (see section 5.2), but we believe the cluster near $\mathcal{D} = 0.5$ is a manifestation of a different effect.

If the duty cycle is reasonably close to 0.5 already, applying an AC drive field can induce phase locking and shift $\mathcal{D}$ toward equal populations. The fact that Fig. 4.6 shows gaps between $0.3 \leq \mathcal{D} < 0.5$ and $0.5 < \mathcal{D} \leq 0.7$ suggests that there is a drive-dependent threshold for $\mathcal{D}$ at which configurations that would have $\mathcal{D} \neq 0.5$ at zero drive are all

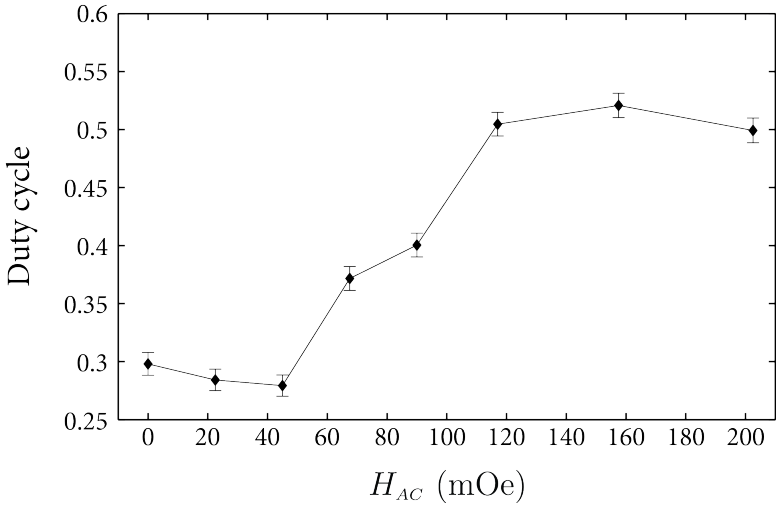

Figure 4.7: Duty cycle $\mathcal{D}$, as a function of applied field magnitude H_{AC}. At higher magnitudes of H_{AC}, system sees shift in $\mathcal{D}$ toward $\mathcal{D} = 0.5$ with onset of phase locking.

collapsed to $\mathcal{D} \approx 0.5$. We can observe this directly by applying a constant transverse H_{DC} such that the system has $\mathcal{D} \neq 0.5$ at zero drive. If we then turn on the AC drive field, we see the duty cycle shift, as in Fig. 4.7.

4.3 Comparison to models of internal order parameter

There have been several attempts[33,58,59] to model the weight coefficients w_i from Eq. 2.43 theoretically. We can test the validity of these methods by comparing them with our measured data for the amplitude $\mathscr{M}(\omega_D)$ and phase lag φ. Fig. 4.8 shows our measured data for $\mathscr{M}(\omega_D)$ in diamonds, along with the phase lag, in triangles. The first point to make is that there is a clear downturn in the measured phase at low temperature. This is very unlike the behavior predicted by the two-state model from 2.3.2, where the phase should go as

$$\varphi(T, \omega_D) = \arctan\left(\frac{\omega_D}{2f_A}\right), \tag{4.7}$$

which is shown on Fig. 4.8 as the wide gray fit line. In addition, the two-state model does not adequately describe the magnitude of oscillations at high temperatures, predicting a steeper die-off with increasing temperature than is actually observed.

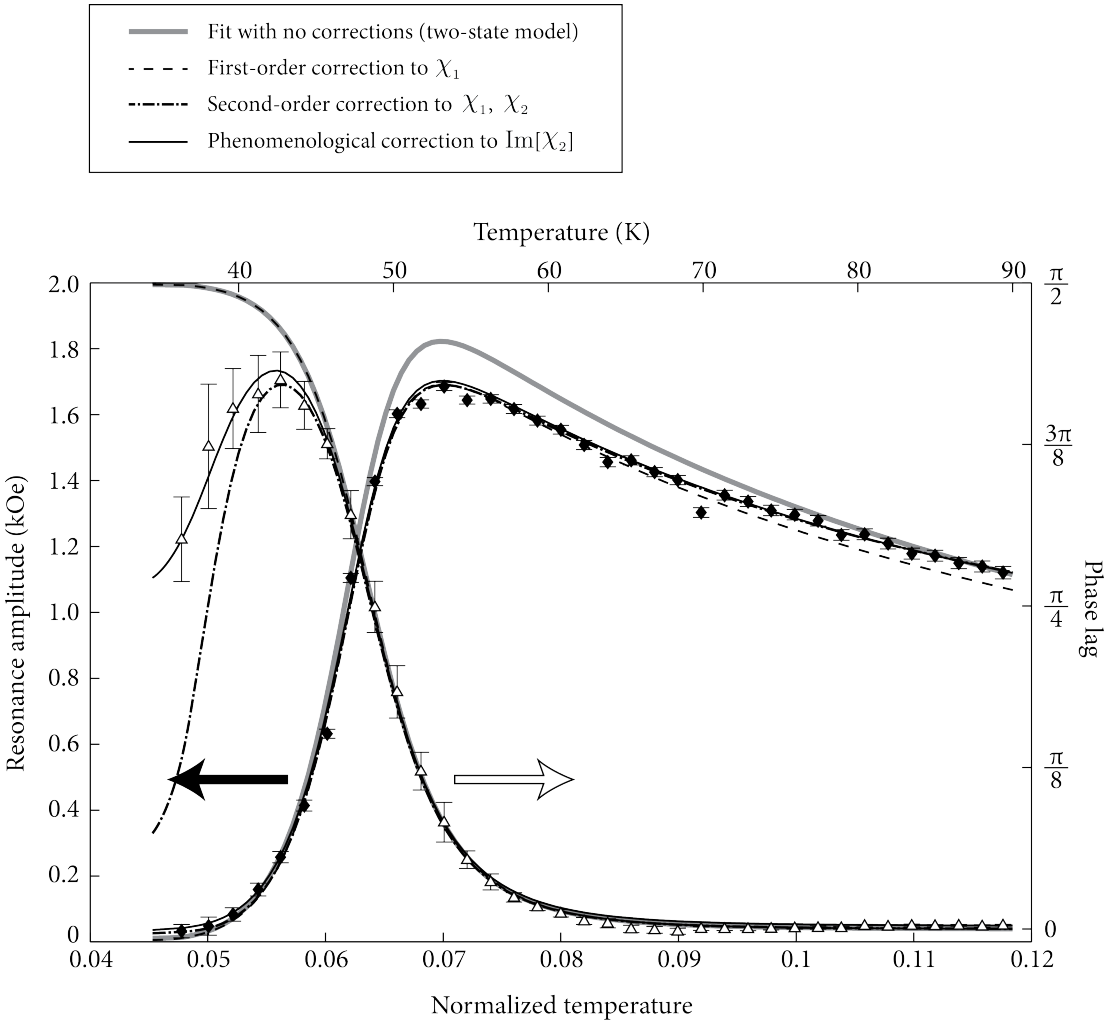

Figure 4.8: Stochastic resonance amplitude (diamonds, left axis) and phase (triangles, right axis) as a function of normalized temperature $\sigma^{-1} = k_B T/\Delta V$. Wide gray line shows two-state model (Eqs. 2.40, 2.41). Dashed line shows effects of including the internal order correction for χ_1 up to first order in σ^{-1} (Eq. 4.10, $\varepsilon_2^{(1)} = \varepsilon_2^{(2)} = 0$). Dot-dashed line includes corrections out to second order in σ^{-1} for χ_1, as well as a nonzero χ_2 (Eq. 4.10). Thin solid line shows fit to Eq. 4.11, with corrections to second order for both χ_1 and χ_2 and a phenomenological correction to $\mathrm{Im}[\chi_2]$. In all cases, the RTN attempt frequency and energy barrier for the model was determined from a separate Arrhenius fit, not a best fit to the resonance data.

To improve this, we will follow the method of [33, 58, 59], and modify Eq. 2.43 to allow for intrawell transitions, in addition to expanding the weight coefficients w_i in terms of a dimensionless energy parameter $\sigma \equiv \Delta E/k_B T$. To second order in σ^{-1}, the most general form for the susceptibility is

$$\chi(\omega,T) = \frac{\mathrm{ZDA}}{T}\Bigg\{ \left(\varepsilon_0^{(1)} + \frac{\varepsilon_1^{(1)}}{\sigma} + \frac{\varepsilon_2^{(1)}}{\sigma^2}\right)\frac{1}{1+i\omega\tau_1} + \left(\varepsilon_0^{(2)} + \frac{\varepsilon_1^{(2)}}{\sigma} + \frac{\varepsilon_2^{(2)}}{\sigma^2}\right)\frac{1}{1+i\omega\tau_2} + \left(\varepsilon_0^{(3)} + \frac{\varepsilon_1^{(3)}}{\sigma} + \frac{\varepsilon_2^{(3)}}{\sigma^2}\right)\frac{1}{1+i\omega\tau_3} + \mathcal{O}(\sigma^{-3})\Bigg\}, \quad (4.8)$$

where τ_1 is the interwell transition time, τ_2 and τ_3 are the characteristic relaxation times for the two wells, and the $\varepsilon_i^{(k)}$ are scalar coefficients that will be determined by fitting. For simplicity, we will refer to the three terms within the brackets of Eq. 4.8 as χ_1, χ_2 and χ_3.

It can be shown,[33] using asymptotic limits from [60], that Eq. 4.8 reduces for a particle with uniaxial anisotropy to

$$\chi(\omega,T) = \frac{\mathrm{ZDA}}{T}\Bigg\{ \left(1 - \frac{1}{\sigma} - \frac{3}{4\sigma^2}\right)\frac{1}{1+i\omega\tau_1} + \frac{1}{8\sigma^2}\left(\frac{1}{1+i\omega\tau_2} + \frac{1}{1+i\omega\tau_3}\right) + \mathcal{O}(\sigma^{-3})\Bigg\}. \quad (4.9)$$

Our situation differs in that we have fourfold rather than twofold anisotropy. In addition, [33] assumes a crystalline anisotropy, which can behave qualitatively differently from a configurational anisotropy because the anisotropy energy of each individual spin is only determined by its orientation with respect to the (static) lattice, rather than other spins. For these reasons, we do not expect the same coefficients $\varepsilon_i^{(k)}$ as in Eq. 4.9. Nevertheless, we can make some restrictions on Eq. 4.8 before attempting to fit.

First, we will take $\varepsilon_0^{(1)} = 1$ with no loss of generality since an overall scaling factor is included in the ZDA. Second, we will assume that the imaginary parts of χ_2 and χ_3 are both negligible. For the sample in question, the lowest attempt frequency, as measured with a separate Arrhenius fit, is 2.8×10^6 Hz. This gives a value for $\omega_D \tau_2$ of 3.5×10^{-5}, meaning that the imaginary part of χ_2 is five orders of magnitude smaller than its real

part. Making this approximation allows us to significantly clean up Eq. 4.8 because we can combine χ_2 and χ_3 and only fit for one set of $\varepsilon_i^{(2)}$. A third limitation can be made by enforcing the boundary condition that χ is finite at $T = 0$. This forces $\varepsilon_0^{(k)} = 0$ for all χ_k except χ_1. (τ_1 grows exponentially as $T \to 0$, so χ_1 can still satisfy the boundary condition with a finite $\varepsilon_0^{(1)}$.) Finally, the fact that $\varepsilon_1^{(2)}$ and $\varepsilon_1^{(3)}$ are both zero in Eq. 4.9 is a reflection of the fact that a shift in the expectation value of $\mathbf{M}$ within a well as the temperature is increased should not affect the response due to oscillations within that well.[61] This should apply equally to our situation with a general well shape. For now, we will leave $\{\varepsilon_0^{(2)}, \varepsilon_1^{(2)}\} = 0$ and later evaluate the validity of this approximation.

With the above approximations, Eq. 4.8 reduces to

$$\chi(\omega, T) = \frac{\mathrm{ZDA}}{T}\left\{\left(1 + \frac{\varepsilon_1^{(1)}}{\sigma} + \frac{\varepsilon_2^{(1)}}{\sigma^2}\right)\frac{1}{1 + i\omega\tau_1} + \frac{\varepsilon_2^{(2)}}{\sigma^2} + \mathcal{O}(\sigma^{-3})\right\}. \tag{4.10}$$

Initially, we will use only $\varepsilon_1^{(1)}$. The relaxation time τ_1 is given by $\tau_1 = (2f_0)^{-1}e^{\Delta E/k_B T}$, where the effective f_0 and ΔE were separately measured using an Arrhenius fit to be 1.9×10^9 Hz and 65.5 meV, respectively. We emphasize that the effective f_0 and ΔE are measured concurrently with a stochastic resonance measurement under conditions where the transverse H_{DC} varies with temperature. They are not the same as the actual f_0 and ΔE from Fig. 4.1, which are separately measured using a constant transverse H_{DC}. The resulting fit, with $\varepsilon_1^{(1)} = 0.7$, is shown by the dashed line in Fig. 4.8. While it improves the curvature of $\mathscr{M}$ at high T, it does not alter the phase at all, since we still have $\chi_2 = 0$.

A better fit is obtained with

$$\begin{aligned}\varepsilon_1^{(1)} &= 0.21\\ \varepsilon_2^{(1)} &= 3.5\\ \varepsilon_2^{(2)} &= 5,\end{aligned}$$

as shown with the dot-dashed line in Fig. 4.8. We note that, while $\varepsilon_1^{(1)}$ appears negligible compared to $\varepsilon_2^{(1)}$ and $\varepsilon_2^{(2)}$, the extra factor of σ^{-1} means that all three have corrections of similar magnitude. This model fits the amplitude very well and gives a peak in φ at the correct temperature. At very low temperatures ($\sigma^{-1} < .055$), however, it does

not seem to recreate the curvature in φ. This region has a large uncertainty in φ_{meas}, a consequence of the low amplitude, but the model still predicts a value well outside the experimental error.

To do better, we can relax the requirement that $\varepsilon_0^{(2)}$ is zero, and instead give it a small imaginary value, so that Eq. 4.10 becomes

$$\chi(\omega,T) = \frac{\mathrm{ZDA}}{T}\left\{\left(1+\frac{\varepsilon_1^{(1)}}{\sigma}+\frac{\varepsilon_2^{(1)}}{\sigma^2}\right)\frac{1}{1+i\omega\tau_1}+i\varepsilon_0^{(2)}+\frac{\varepsilon_2^{(2)}}{\sigma^2}+\mathcal{O}(\sigma^{-3})\right\}. \tag{4.11}$$

This model is plotted in solid black in Fig. 4.8, for the values

$$\begin{aligned} \varepsilon_1^{(1)} &= 0.21 & \varepsilon_2^{(1)} &= 3.5 \\ \varepsilon_0^{(2)} &= 0.009 & \varepsilon_2^{(2)} &= 4.4\,. \end{aligned}$$

We emphasize that Eq. 4.11 should be considered a phenomenological model. It follows the same form as Eq. 4.8, but it no longer satisfies the boundary condition for $T = 0$. In addition, we do not have a good explanation for why there should be an imaginary part to χ_2. Mathematically, it is straightforward to extract an imaginary part from the factor $(1 + i\omega\tau_2)^{-1}$ if $\tau_2 \sim \omega$, but this is not a physical scenario, given our measured values of ω_D and τ_2.

Another unresolved question regarding this model has to do with the behavior of φ at high temperatures. Near $\sigma^{-1} = 0.09$, the phase lag reaches a minimum near zero, before slowly rising. This behavior is not observed in any of our models for χ, and is best seen in a plot of the residual phase lag $\varphi_{model} - \varphi_{meas}$, as shown in Fig. 4.9. The region in question, from $0.07 \lesssim \sigma^{-1} \lesssim 0.11$ does not have a large residual error after fitting (less than 2% of the total range of φ), but it is still larger than the experimental error for the region. We have observed this effect in multiple samples, so a stronger model for χ should take it into account.

Returning to the other fitting parameters, a qualitative difference between our fit and Eq. 4.9 is that Eq. 4.9 has $\varepsilon_1^{(1)}, \varepsilon_2^{(1)} < 0$. By contrast, all of our fitting parameters are positive. We interpret this as being a reflection of the well shape. The model used to derive Eq. 4.9 assumed an energy potential of $U = -\cos 2\theta$ where θ is the angle of the magnetization with respect to the easy axis. Expanding this to fourth order in θ gives a negative correction to the fundamental harmonic well, i.e., $U = U_0(-1 + 2\theta^2 - 2\theta^4/3)$.

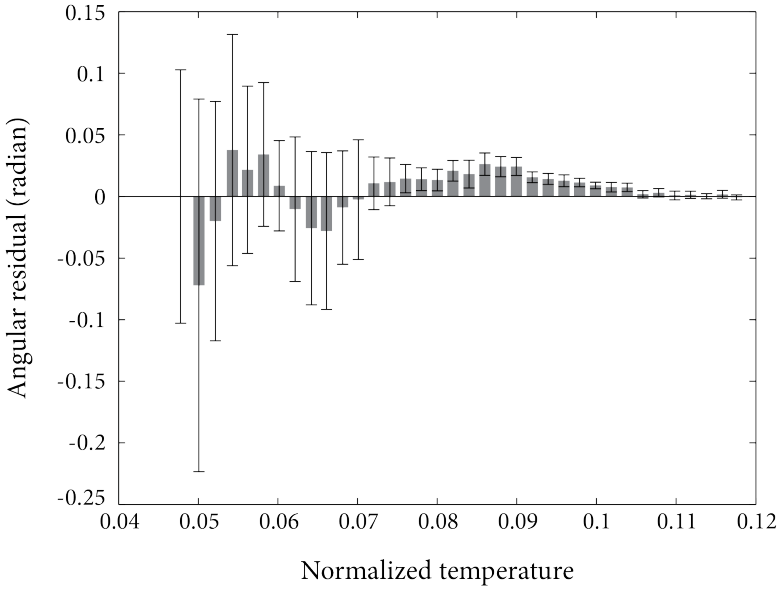

Figure 4.9: Residuals from fitting the phase lag of Eq. 4.11 to the measured data from Fig. 4.8. Plotted data show $\varphi_{model} - \varphi_{meas}$, along with measurement uncertainty on φ_{meas}.

The spectrum of relaxation times τ_k and weights w_k can be solved exactly if U is only taken to second order in θ, but higher orders of θ require the use of perturbation theory to calculate the expansion terms in Eq. 4.9. Since it is the correction terms in $U(\theta)$ that give rise to correction terms in χ, we infer that the energy surface of our samples should have a positive fourth-order correction to $U(\phi)$ to account for the positive $\varepsilon_1^{(1)}, \varepsilon_2^{(1)}$. Or,

$$U(\phi) = -U_0 + c_1\phi^2 + c_2\phi^4 + \mathcal{O}(\phi^6), \tag{4.12}$$

with c_1, $c_2 > 0$.

Physically, this is plausible, given what we know of the magnetic structure at the conditions for RTN. If the sample is in the S state, as shown in Fig. 4.10, it already has regions where the local $\mathbf{M}$ is in the $\phi = 0°$ and $\phi = 90°$ directions, with quasi-domain walls (regions with high local magnetic curvature) marked with dashed lines. It should not cost very much energy to rotate the net magnetization, then, since the sample only needs to shift these quasi- domain walls slightly to alter the ratio of spins with $\mu_{0°}$ versus $\mu_{90°}$. This only works for a limited range of $\delta\phi$, however, because the quasi- domain walls will either meet in the middle of the dot, or be confined to the

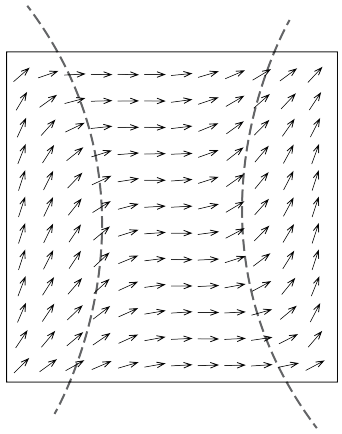

Figure 4.10: Magnetic structure for S state, with dashed lines as guides to the eye denoting quasi- domain walls where local magnetization shifts from being primarily oriented along the 0° direction to the 90° direction.

edges. When this happens, the sample must tighten the width of the quasi- domain walls in order to achieve a further rotation in the net magnetization. This should cost a significant amount of exchange energy, and a sudden increase in $\partial U/\partial\phi$, hence the positive correction to the curvature of $U(\phi)$.

4.4 Phase peak effects

An outstanding question is what effect the external field H_{DC} has on the order parameter. One method of investigating this is to look at the location of the peak in the phase lag, φ_{max}, under different measurement conditions. Even though Eq. 4.10 needs to be solved numerically for the location of φ_{max}, on inspection, we can see that this maximum should be constant in normalized temperature for an arbitrary energy barrier as long as the rest of the well parameters are unchanged. This happens because the phase is only dependent on χ_1 and χ_2; it is not affected by the factor of ZDA/T outside the brackets. To test this, we made several stochastic resonance measurements on a single sample, varying the 45° field between temperature sweeps to change the effective well depth. If χ_1, χ_2 are truly functions only of the unitless parameter σ, the peak should be constant for different values of field. There is a slight complication here since the large changes in applied field also affect the attempt frequency, but this can be accounted

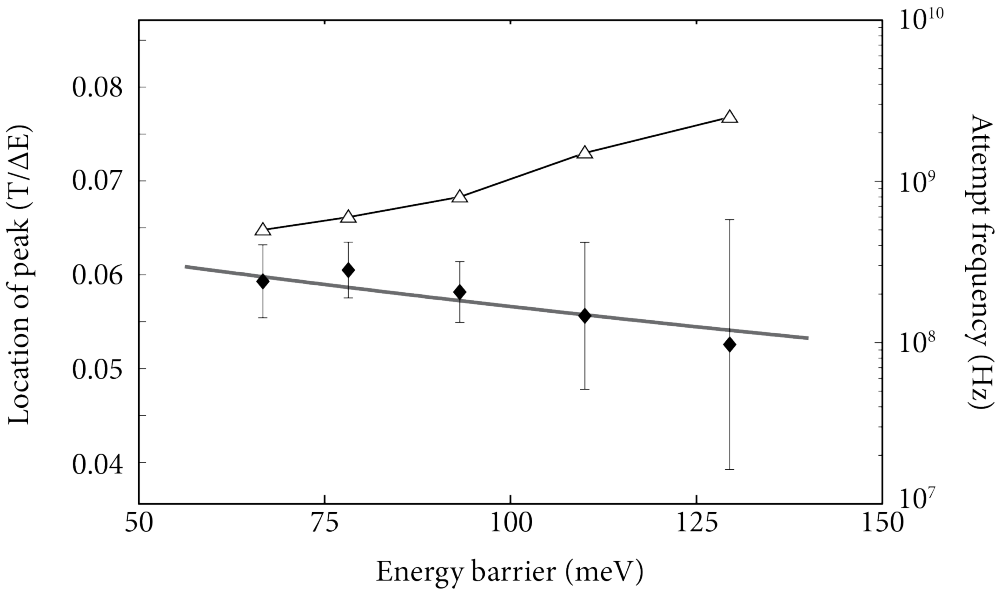

Figure 4.11: Location of peak in phase (diamonds, left axis) as a function of energy barrier. Peak location is plotted in terms of unitless temperature $T/\Delta E$. Gray line shows prediction from solving Eq. 4.10 numerically for the phase peak. Attempt frequency used for calculation is determined using a phenomenological fit of the measured attempt frequency (triangles, right axis) to the energy barrier using an exponential form.

for by fitting an exponential relationship between f_0 and ΔE and including this in the model for $\varphi_{max}(\Delta E)$. The results are shown in Fig. 4.11. We observe a slight decrease in the normalized temperature of φ_{max} with increasing well depth, which is mirrored by the predicted location found by solving Eq. 4.10 numerically. While not conclusive, this is consistent with the model that the χ_i are only dependent on the normalized (not absolute) temperature, and that the order parameter is largely independent of well depth.

Chapter 5

Other effects

5.1 Spread of attempt frequencies

Throughout this study, we have observed a broader range of attempt frequencies than would be expected from Eq. 2.30. Typically, ferromagnetic resonance frequencies are assumed to be on the order of 10^{10} Hz. In our samples, however, we have seen attempt frequencies that range from 10^5 Hz to 10^{15} Hz. Moreover, we have seen dots where the ratio of attempt frequencies f_0^H/f_0^L is as high as 10^7 (as shown in Fig. 4.1). This would seem to suggest that there is a more complicated mechanism than just the ferromagnetic resonance that determines the attempt frequency, and if we examine the spread of attempt frequencies plotted in Fig. 5.1, we can see a trend that gives insight into this underlying mechanism. Specifically, there appears to be a correlation between f_0^H and f_0^L such that the geometric mean of the two falls between 10^9 Hz and 10^{10} Hz in the majority of our samples. This suggests that there is an intrinsic resonance frequency around 10^{10} Hz, which is scaled by some factor α, α^{-1} for the high and low well, respectively.

To test the validity of this, we can calculate an approximate ferromagnetic resonance frequency for our samples. Following [62], this is done by finding normal modes of the equation

$$\frac{\partial \mathbf{M}}{\partial t} = \gamma(\mathbf{M} \times \mathbf{B}), \tag{5.1}$$

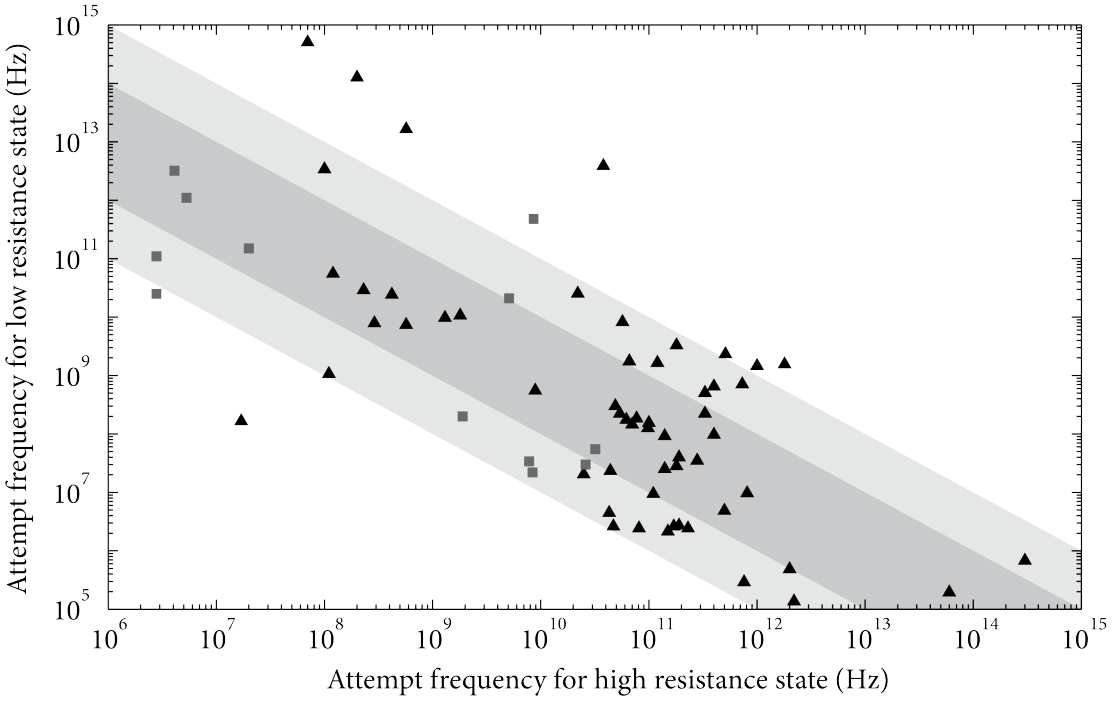

Figure 5.1: Measured attempt frequencies plotted as f_0^L vs. f_0^H. Black triangles represent samples made with Ti/Au contacts, while gray squares represent W/Au samples. Shaded region denotes spread of the geometric mean $\bar{f}_0$ of the two frequencies. Dark shading corresponds to 10^9 Hz $\leq \bar{f}_0 \leq 10^{10}$ Hz, while light shading corresponds to 3.3×10^8 Hz $\leq \bar{f}_0 \leq 3.3 \times 10^{10}$ Hz.

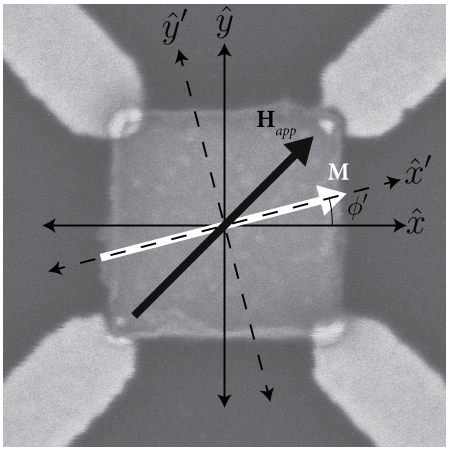

Figure 5.2: Coordinate transform for FMR calculation. Magnetization and applied field directions are shown with white and black arrows.

where the total field is given by the sum of applied and demagnetization fields

$$B_i = H_i - N_i M_i. \tag{5.2}$$

This calculation is complicated somewhat by the fact that neither the applied field $\mathbf{H}$ nor the net magnetization $\mathbf{M}$ are exactly along one of the three directions $\hat{x}, \hat{y}, \hat{z}$. In addition, there is an effective field from the anisotropy, $\mathbf{H}_A$, which needs to be included. In order to make things simpler, we can shift into a new coordinate system $\hat{x}', \hat{y}', \hat{z}$, as shown in Fig. 5.2, where $\hat{x}'$ is aligned with the magnetization and makes an angle ϕ' with $\hat{x}$. The demagnetization factors in this projection then become

$$N_x' = \sqrt{N_x^2 \cos^2\phi' + N_y^2 \sin^2\phi'}, \qquad N_y' = \sqrt{N_x^2 \sin^2\phi' + N_y^2 \cos^2\phi'}. \tag{5.3}$$

We assume for simplicity that $\mathbf{H}_A \parallel \hat{x}$ and $\mathbf{H} = H_0(\hat{x} + \hat{y})$. Then, inserting Eq. 5.3 into Eq. 5.1 and making the approximations $\dot{M}_x' = 0$, $M_x' = M$ gives two coupled equations for the precession of $\mathbf{M}$ in $\hat{y}'$ and $\hat{z}$:

$$\begin{aligned}
\dot{M}_y' &= \gamma M_z \Big[(H_0 + H_A)\cos\phi' + H_0 \sin\phi' + M(N_z - N_x') \Big] \\
\dot{M}_z &= -\gamma M_y' \Big[(H_0 + H_A)\cos\phi' + H_0 \sin\phi' + M(N_y' - N_x') \Big] \\
&\qquad + \gamma M \Big[H_0 \cos\phi' - (H_0 + H_A)\sin\phi' \Big].
\end{aligned} \tag{5.4}$$

In the equation for $\dot{M}_z$, we can use the restriction that $\langle \dot{M}_z \rangle = 0$ to find a relationship between H_0, H_A, and ϕ', since the second term will cause $\dot{M}_z$ to grow indefinitely unless it sums to zero. Using this, and solving for the normal modes of Eq. 5.4 gives

$$\omega_0 = \gamma \sqrt{\left[H_0 \csc\phi' + M_s(N'_y - N'_x)\right]\left[H_0 \csc\phi' + M_s(N_z - N'_x)\right]}. \tag{5.5}$$

In order to go further, we need to know the demagnetization factors N_i. As an approximation, we can assume that they are proportional to the surface area of the corresponding sample face, i.e.,

$$\frac{N_z}{\ell^2} = \delta \frac{N_x}{t\ell} = \delta^{-1} \frac{N_y}{t\ell} = \frac{\tilde{N}}{t\ell}, \tag{5.6}$$

where ℓ and t are the sample width and thickness. In Eq. 5.6, δ is a scaling factor to provide some asymmetry between N_y and N_x. Using our known sample dimensions, as well as the identity $\sum N_i = 4\pi$, gives

$$N_z = \frac{100\pi}{27}, \quad \tilde{N} = \frac{4\pi}{27}. \tag{5.7}$$

With these, and reasonable values for H_0, M_s, and γ, we can calculate the attempt frequencies for various values of δ as shown in Fig. 5.3. The angle $\phi' \approx 25^\circ$ for a typical dot can be estimated by comparing the AMR of an RTN signal with the AMR for saturation in the 0° and 90° directions.

Fig. 5.3 shows that an asymmetry in the demagnetization factors can cause the type of splitting in the ferromagnetic resonance that we observe in our attempt frequencies, and that, for small values of δ, the geometric mean of the two resonances is approximately constant. There is a clear discrepancy, however, in the magnitude of the splitting. In our calculation, there is less than a decade of splitting between the favored and unfavored states before the unfavored state becomes dominant and the approximation of a constant $\bar{\omega}_0$ is no longer valid. By contrast, we see factors as wide as 10^6 in our measured data that do not correlate with any reduction in $f_H f_L$. We attribute this to our approximation that anisotropy behaves like a uniform field balancing the applied field $\mathbf{H}$, which is likely invalid near the conditions for RTN. A more physical

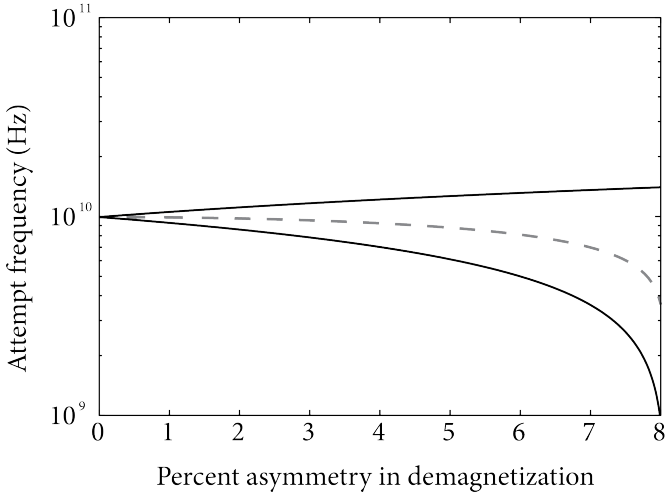

Figure 5.3: Calculated attempt frequencies for favored (top) and unfavored (bottom) wells as a function of well asymmetry $\delta/\tilde{N}$. Model assumes values of $H_0 = 65$ Oe, $M = 7$ kG, $\gamma = 2.9$ MHz/kG. Dashed line shows geometric mean of f_0^H and f_0^L.

picture would have stronger curvature in the anisotropy (which itself arises from the demagnetization and exchange fields). This is supported by comparing the splitting of attempt frequencies with the well asymmetry, as shown in Fig. 5.4. If unequal attempt frequencies are arising from the curvature of the anisotropy, they should correlate with the well depth since a deeper well will tend to be sharply curved. It is notable that the correlation between f_0^H/f_0^L and ΔE is much stronger than the link between f_0^H and f_0^L. This tends to suggest that the "intrinsic" frequency $\overline{f_0} = (f_0^H f_0^L)^{1/2}$ may be determined by a more complicated mechanism than anisotropy alone. If we write the attempt frequency of the two states as

$$f_0^H = \alpha \overline{f_0} \qquad\qquad f_0^L = \alpha^{-1} \overline{f_0}, \tag{5.8}$$

Fig. 5.4 shows a strong correlation between the well anisotropy and α, but Fig. 5.1 shows a wide spread of $\overline{f_0}$ with little correlation to anisotropy. This points to a different mechanism being the source for the observed range of $\overline{f_0}$.

One feature that this treatment does not account for is any low-frequency mode caused by magnetic pinning from shape imperfections. These low-frequency modes should not affect the attempt frequency since we expect hopping to be governed by the highest-frequency relaxation mode (other modes can still induce switching, but these

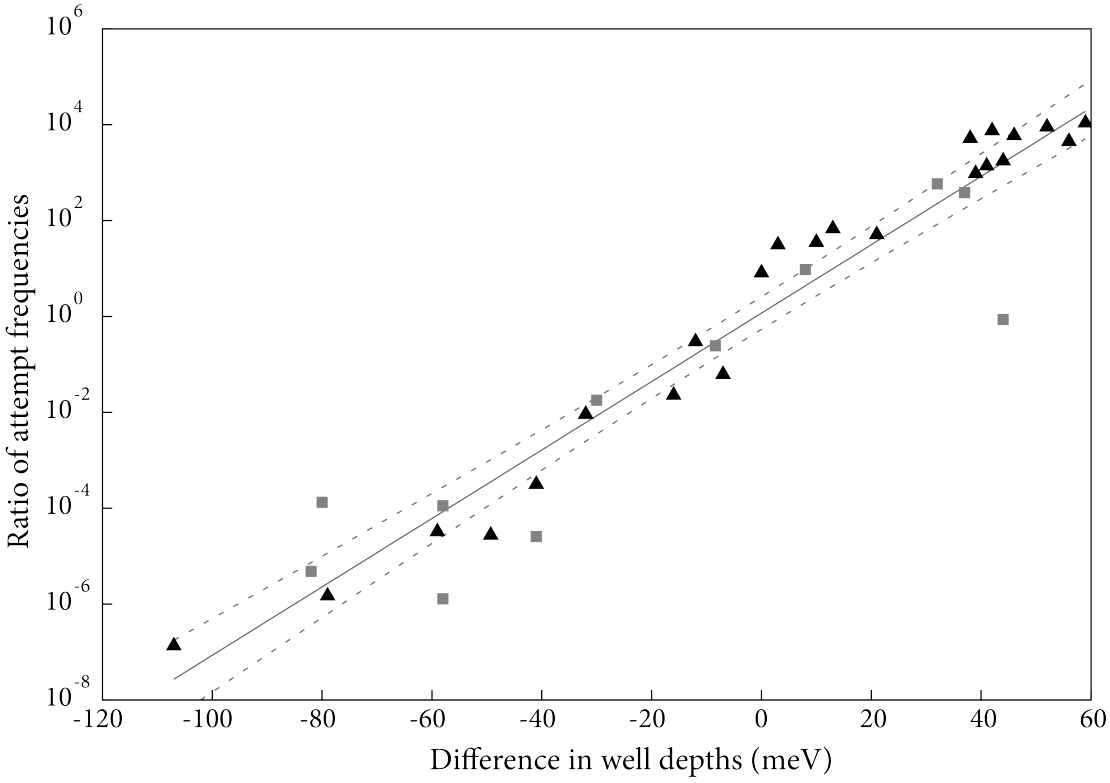

Figure 5.4: Ratio of attempt frequencies $\tilde{f} \equiv f_0^H / f_0^L$ plotted versus difference in well depths $\tilde{E} \equiv \Delta E_H - \Delta E_L$. Black triangles represent samples with Ti/Au contacts. Gray squares have W/Au contacts. Solid line represents fit to $\tilde{f} = 1.17 \times \exp[\tilde{E}/6]$.

transitions will not be observable on a laboratory time scale). One possible effect of low-frequency modes is that they could account for the phenomenological term in Eq. 4.11. If there are relaxation modes with $\tau \sim \omega_D^{-1}$ that do not contribute to observable transitions, they could result in a response that has a non-negligible imaginary part at low temperatures.

A good candidate for the mechanism controlling $\overline{f_0}$, is the barrier shape function $\xi(\lambda, M_s, U_m)$, from Eq. 2.30, since it will be symmetric for the two wells. It also has the potential to shift the intrinsic $\overline{f_0}$ to an anomalously high frequency if the sample in question has a high barrier entropy (the factor Ω from Eq. 2.16), or to an anomalously low frequency if the barrier has low curvature. The easiest method of checking this possibility would be to perform a direct ferromagnetic microwave resonance experiment in tandem with a switching experiment. If the ferromagnetic resonance differs from the attempt frequency, it would indicate that the spread of attempt frequencies is due to a mechanism within the switching process.

5.2 Stray field effects

At the conditions for RTN, our samples can serve as exceptionally sensitive compasses, capable of detecting a change in applied field of less than 25 mOe. This is best seen by tracking the dwell time distribution $\mathcal{N}(\omega)$ as shown in Fig. 5.5. Stray fields can be problematic when making measurements because our setup has no special shielding for static magnetic fields. Our laboratory is located on the basement corner of our building, and we have done our best to minimize movement around the refrigerator during measurement runs, but we can still see fluctuations in the duty factor, which we attribute to stray fields that originate either with movement of equipment on the floor above, or from the elevator located approximately 10 m down the hall.

Because our background for stray fields is relatively high, it is difficult to tell the exact sensitivity of the switching process and it is likely that we could have even higher resolution in a shielded environment. This effect is likely to be amplified near the conditions for stochastic resonance as discussed in 4.2.2 when the duty cycle is close to the threshold for phase locking. In this scenario, the system would be inherently unstable and a small change in the external field could induce large changes in the duty

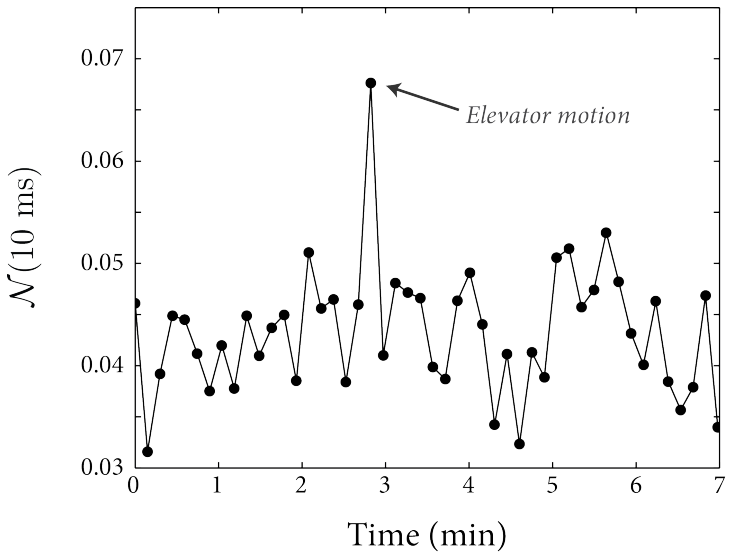

Figure 5.5: Ratio of individual dwell times that fall within 9 ms $< \tau <$ 11 ms as a function of time, with constant temperature and applied external field. Spike seen just before 3 minutes is from stray fields due to elevator motion.

cycle (and by extension the stochastic resonance amplitude) as the stochastic signal either becomes phase locked or dephased with respect to the drive signal.

5.3 Current effects

5.3.1 Spin-transfer torque

AMR was chosen as the probing technique in part because it is nonperturbative, i.e., the measurement does not depend on interaction with an applied field. This is only strictly true, however, in the zero-current limit. A finite current can still affect the magnetization, either by the current-induced Zeeman field or from spin-transfer torque. The first of these is relatively easy to account for and is shown in Fig. 5.6. The second effect, spin-transfer torque, is more complicated because it relies on a non-uniform magnetization and will therefore vary through a switching cycle.

Traditionally, spin-transfer torque is associated with a $FM_1/NM/FM_2$ heterostructure where the FM_i are ferromagnets with $\mathbf{M}_1 \nparallel \mathbf{M}_2$, and the center layer is a nonmagnetic spacer of thickness t_n. If a current is flowing from FM_1 to FM_2, it will become

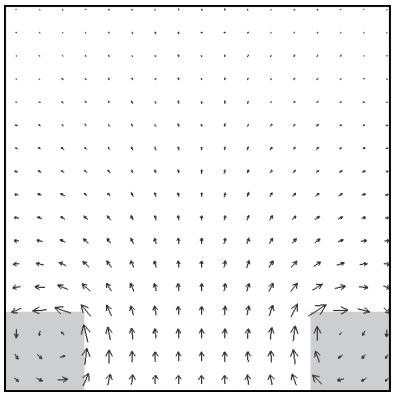

Figure 5.6: Local field map due to applied current. Shaded areas show location of current source and sink. Maximum local field has magnitude $|H| \approx 10$ G. Calculated using LLG Micromagnetics software.

spin-polarized as it passes through the initial layer. Assuming that the nonmagnetic spacer has a large spin diffusion length $l_{\uparrow\downarrow} \geq t_n$, this spin-polarized current will impart angular momentum into the second ferromagnet, causing either precession of the magnetization (for a constant current) or switching (for a pulsed current).[63,64] Although our dots only have a single layer, the magnetization is nonuniform between the current source and sink (see Fig. 3.12) so there will still be a net transfer of angular momentum from one side of the dot to the other. This is unlikely to induce switching events of its own accord, but can affect the characteristic switching frequencies of stochastic reversals as in Fig. 5.7. A similar effect can occur across a domain wall causing the wall to drift with the application of a in-plane current.[65] The hallmarks of spin-transfer torque are that it varies monotonically with current, but may not be symmetric about zero since the magnitude of the effect will depend on how strongly pinned the magnetization is near the sink electrode. For this reason, it is not easy to approximate spin-transfer torque as an effective field.

The effect of spin torque on the Kramers time of a superparamagnetic particle has been investigated numerically by [66], using the model system of a FM/NM/FM heterostructure. They found that the effective well depth goes as

$$\widetilde{\Delta E} = \Delta E \left(1 \mp \frac{I}{I_0}\right), \tag{5.9}$$

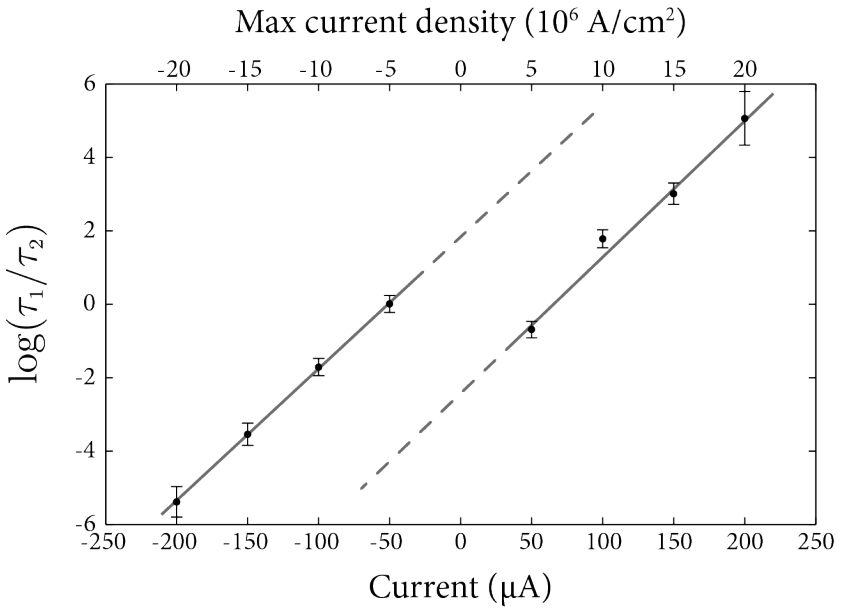

Figure 5.7: Log-ratio of the average dwell times as a function of current. Positive and negative current were taken with different applied fields in order to maximize the range of currents over which measurements could be taken. 50 μA is the minimum current necessary to observe RTN above the Johnson-Nyquist background for our setup.

where I_0 is a characteristic current that is less than the critical current I_c required for switching at zero temperature. In the low bias limit this form mirrors that of an effective field and is consistent with the data shown in Fig. 5.7. By contrast, the attempt frequency goes as

$$\widetilde{f_0} = f_0 \left(1 \pm \frac{I}{\tilde{I}}\right) \left[1 - \left(\frac{I}{I_c}\right)^2\right], \tag{5.10}$$

where $\tilde{I}$ is a (new) characteristic current that defines the current necessary to flatten the energy surface of the unfavored well to second order in angle. If the current modifies the attempt frequency differently than it does the well depth, it could create a slight global bias for one of the two wells when comparing the attempt frequency versus the well depth. This may be the origin of the slope of the data in Fig. 5.4; an unbiased system should have a exponential prefactor of 1, whereas the measured prefactor was 1.17. This discrepancy is still within the limits of our experimental uncertainty, however, so

we cannot say conclusively that the two are different. The effect of spin-transfer torque on RTN in our samples is an area of ongoing study that has not yet been resolved because of electromigration issues, as discussed below.

5.3.2 Electromigration

A difficulty when working with current-dependent noise is that high current densities can physically modify the materials forming the electrical conduit. This can happen either by local Joule heating of a weak point along the current path or by direct momentum transfer from the electron current to the lattice. This second method, known as electromigration, has been of interest for decades in the semiconductor industry[67,68] and can observed in our samples for high current biasing.

Electromigration occurs when enough momentum is present in the electron wind to move ions out of their original lattice positions. This is typically assumed to leave a vacancy in the lattice that is then nonconductive. A buildup of vacancies at one location can have a runaway effect (since the same amount of current now has fewer paths to take) leading to failure of the device.[69] For this reason, the most common figure of merit when discussing electromigration is the mean time to failure (MTTF). This follows the phenomenological law:[67]

$$\text{MTTF} \propto \frac{A}{J^2} e^{\varepsilon/k_B T}, \tag{5.11}$$

where A represents the cross-sectional area of the current path, J is the current density, and ε is a material-dependent activation energy. If we define an acceptable MTTF, for example 10 years, Eq. 5.11 allows us to calculate the critical current density and temperature that should not be exceeded.

While the above equation was originally formulated to account for vacancy migration in elemental metals, substitutional migration can also occur in alloys and across interfaces between materials. This is more interesting for our current scenario because device failure can be taken to have a broader meaning—a dot has "failed" when electromigration has altered its magnetic or resistive properties in any measurable way. This has been observed before in NiO films where current annealing with pure Ni contacts changed both the film resistance and the switching characteristics.[70] To date, there have not been many studies involving electromigration in permalloy; this is somewhat

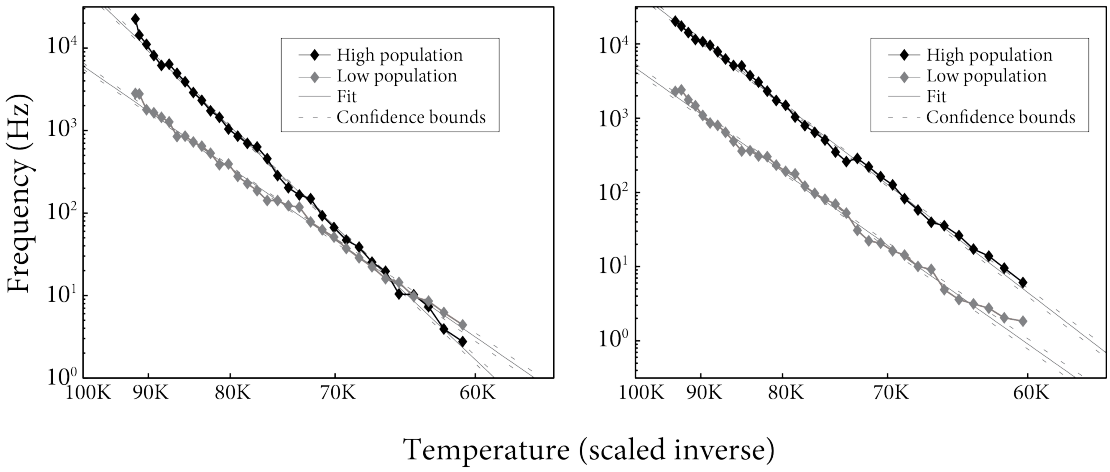

Figure 5.8: Arrhenius plots of switching before (left) and after (right) current annealing. Source current for measurement was 200 µA. Anneal was performed at 100 K with 300 µA for two hours. In both cases, multiple sweeps were taken that showed repeatable results.

surprising, given its importance in magnetoresistive sensors. Nevertheless, it has been seen that vacancy migration occurs on laboratory timescales ($t < 100$ h) with a current density of $J = 9 \times 10^7$ A/cm^2 and temperature of 453 K. By comparison, room temperature is the highest temperature our samples are ever measured (assuming local heating effects are negligible to first order). The maximum current density in the dot is difficult to calculate since it will be nonuniform, but if we approximate the current density as uniform across a surface that extends downward from the edge of the contacts to the substrate, we can calculate a maximum current density of 2×10^7 A/cm^2 for a typical current of 200 µA. Combining these gives an expected MTTF that is ∼200 times larger than that observed by [70], but this assumes that vacancy migration is the only process occurring.

In our samples, we have observed sudden catastrophic failure of the magnetic properties at high current densities, as well as slow, irreversible changes at medium current densities. The latter are plotted in Fig. 5.8, which shows noise measurements across identical field sweeps before and after high-current annealing. Because of the relatively high energy barriers for vacancy migration, we assume that this is primarily due to interstitial migration between the contacts and dot. In an ideal case, this process could

be suppressed by choosing a contact material with a very high activation energy ε, but we have not yet found a material that accomplishes this. Our best results have been with titanium and tungsten. The first of these is unexpected because the activation energy should be roughly correlated with the coefficient of diffusivity between the two materials and Ti will readily diffuse into permalloy.[45] Moreover, titanium can strongly affect the magnetic properties, so only a small number of impurities would be required to have a measurable effect. One possible explanation for the success of this recipe could lie in titanium's propensity for oxidation. It is known that contacts made from in-situ deposited Ti/Mo/Au will show strong diffusion of the gold into the underlying metal, despite the relative immiscibility of gold and molybdenum. If, however, vacuum is broken after deposition of titanium and the layer is allowed to oxidize, no interdiffusion occurs. It is theorized that the presence of oxygen and the composite MoTiO helps to "stuff" the barrier and prevent migration of the gold across grain boundaries in the molybdenum.[71]

In our samples, the Ti/Au contacts are deposited on top of a layer of ruthenium that has been allowed to partially oxidize ex-situ. Given this, it is possible that a similar process is able to take place at the $Ru/RuO_2/Ti$ interface. If this is the case, it is possible that tuning the effect by depositing the titanium under a partial atmosphere of oxygen or nitrogen would further reduce electromigration and allow us to probe samples at higher current densities.

Chapter 6

Conclusions and future work

6.1 Observation of stochastic resonance

Bistable magnetic systems are a rich physical system for the physics of stochastic resonance, in part because they naturally exhibit Ising characteristics that form the basis for both analytical models and numerical simulations of stochastic resonance.[72] Unfortunately, there is a distinct void in the literature of experimental studies on this model system. Our work on permalloy dots has helped to fill this void.

Critical to our work is the fact that we are using a system where we can both characterize the energetics of individual samples and tune the energies with an external field. This allows us to fully manipulate quantities such as well depth, well asymmetry, and the drive amplitude, and probe their effect on stochastic resonance. We have observed all of the major hallmarks of stochastic resonance in our system. Our data show a clear peak in the amplitude of the response that, to first order, dies off as $1/T$ at high temperature. The amplitude of this peak increases with increasing drive amplitude, but the amplification factor $\eta = (\mathscr{M}/H_{AC})^2$ decreases. At temperatures for which the Kramers time is near the matching condition $2f_A = \omega_D$, we see a shift away from stochastic behavior with a Poissonian distribution of dwell times toward driven behavior with phase-locked dwell times. The phase locking can be suppressed by applying a DC transverse field to intentionally drive the system away from a 50% duty cycle. At high driving amplitudes the phase locking can also alter the duty cycle of a system for which $\mathcal{D} \neq 0.5$ in zero drive.

6.2 Comparison to linear response models

Our work includes the first experimental results obtained from a physical system, rather than a bistable electronic circuit, where the data include enough detail to allow comparison to linear-response models. We have seen linear response effects in both the amplitude and phase of the resonant signal. Including linear-response terms in the model allows us to better match the curvature of the amplitude at high temperatures than with the two-state model alone. In our phase lag data, we have observed a low-temperature maximum below the time-scale matching condition $2f_A = \omega_D$. This peak is predicted by linear-response theory, though with a steeper $d\varphi/dT$ as $T \to 0$ than was observed. We have been able to closely match our observed data using a linear-response model with an additional phenomenological term, so that the combined model for the susceptibility χ goes as

$$\chi(\omega, T) \propto \frac{1}{T}\left\{ \left(1 + \frac{\varepsilon_1^{(1)}}{\sigma} + \frac{\varepsilon_2^{(1)}}{\sigma^2}\right) \frac{1}{1 + i\omega\tau_1} + i\varepsilon_0^{(2)} + \frac{\varepsilon_2^{(2)}}{\sigma^2} \right\}, \tag{6.1}$$

where τ_1 is the Kramers time for RTN, σ^{-1} is the unitless temperature $T/\Delta E$, and the $\varepsilon_i^{(k)}$ are all positive, scalar fit parameters. We infer from the fact that $\varepsilon_1^{(1)}$ and $\varepsilon_2^{(1)}$ are both positive that the first correction term to the harmonic approximation for the potential $U(\mathbf{M})$ is positive. This is the opposite of the expected behavior for a magnetic system with uniaxial crystalline anisotropy where the first (quartic) correction to $U(\mathbf{M})$ is negative (as a result of the sinusoidal dependence of energy on magnetization direction). This is a reflection of the fact that configurational anisotropy behaves in a qualitatively different manner from its crystalline counterpart, and it is not necessarily a valid approximation to treat it as an effective field with sinusoidal dependence on the direction of $\mathbf{M}$.

6.3 Future work

6.3.1 Outstanding questions related to attempt frequency

Throughout this study, we have encountered a number of unresolved questions related to the attempt frequency of RTN. To investigate further, we would like to do a direct

microwave resonance experiment to determine the actual FMR frequency of our samples. This would need to follow a somewhat different procedure than a traditional microwave resonance experiment, where a microwave field of constant frequency ω is applied to a film or bulk sample and the external DC field is varied to observe a peak in the absorbed microwave signal (see, for example, [73]). The first difficulty lies in our sample dimensions, which are too small to allow us to observe a peak from a single dot, since the absorbed power is so little. Instead, it is necessary to make an array of identical samples on a single chip and then measure the total absorption of the aggregate. This is a technique our lab is already exploring in order to perform Kerr microscopy on our samples. Second, we would need to invert the procedure of a traditional resonance measurement and hold the DC field constant while varying the frequency of the incident microwaves. This is a more complicated experiment to set up, but it is necessary because we are primarily interested in determining the resonance frequency near the conditions for RTN. If shape effects and magnetic structure are causing large variations to an intrinsic resonance frequency, we would like to be able to measure this frequency while the sample is in the same magnetic state as is necessary for RTN.

The dependence of attempt frequency on spin-transfer torque is an area of interest we have looked into, but we have been unable to obtain conclusive results because of electromigration issues. We have seen changes in the attempt frequency of the dot as the current is increased, but these data are not repeatable because performing a temperature sweep at high current densities for an hour has the effect of current annealing the dot and altering its RTN properties at lower currents. There are two routes we could take to overcome this difficulty. Ideally, we could prevent any form of electromigration. Assuming the mobile atoms are coming from the contacts, the best way to do this would be to pick a contact material with a very high activation energy for atomic migration. We have tried to do this in our investigations of deposition materials, hence the use of tungsten and tantalum. Even with a tungsten/gold bilayer, however, we still see some current annealing effects. It is possible that the tungsten is immobile, and the gold is able to diffuse through the tungsten into the magnetic stack. A method of checking this would be to use pure tungsten for the entire thickness of the contacts, with no gold layer. When trying this, it will be necessary to increase the thickness of the contacts to account for tungsten's reduced conductivity relative to gold.

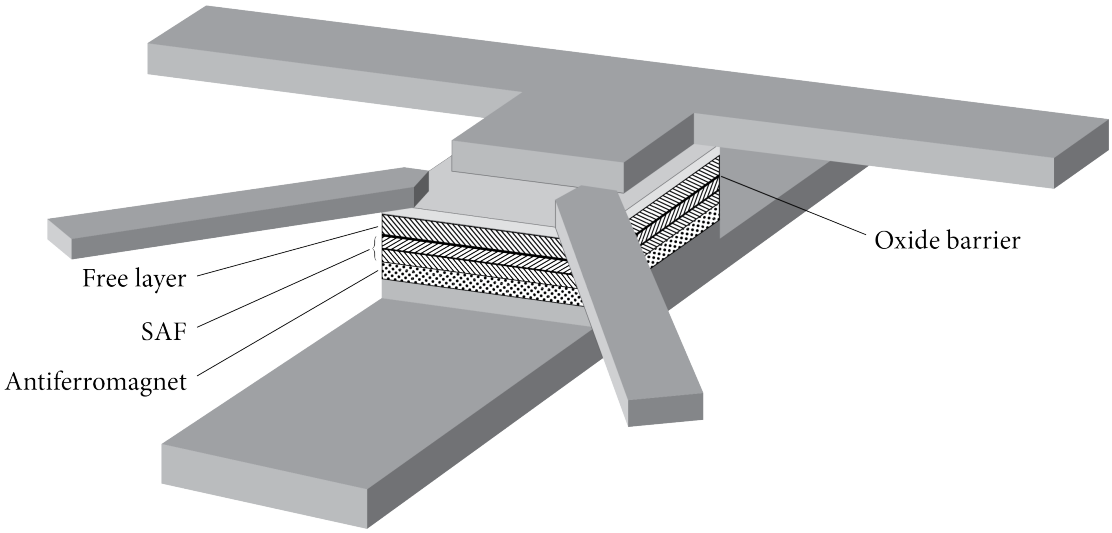

Figure 6.1: Magnetic tunnel junction. From bottom to top, layer stack is composed of bottom electrode, antiferromagnet, synthetic antiferromagnet (SAF), oxide barrier, free layer, and top electrode. SAF is composed of two ferromagnetic layers separated by a thin barrier of ruthenium with antiferromagnetic coupling mediated by the RKKY interaction. Probe current flows vertically through the stack from primary top electrode out the bottom electrode. Smaller top electrodes are for sourcing in-plane current through the free layer to induce spin-transfer torque effects.

If it turns out that electromigration at high current densities can never be entirely prevented, a different option would be to measure at lower current densities where it is negligible. We were unable to do so in this study because we are limited by the minimum current necessary to observe RTN above the Johnson-Nyquist background (see section 3.3.4). In Fig. 5.7, however, we can see that there are clear spin-transfer torque effects visible, even at our lowest measurable currents. If we could then find a way of measuring RTN at these currents, we could observe the attempt frequency across a range of current densities that are all low enough that electromigration is not a factor. One way to do this would be to use a magnetic tunnel junction (MTJ) or spin-valve configuration to measure the angle of the net magnetization through either the tunnel magnetoresistance or giant magnetoresistance effects, rather than with AMR.

For an MTJ structure, as shown in Fig. 6.1, we would source two different currents through the magnetic layer. The probing current would be sourced vertically with a very

small current density. Because of the large $\Delta\rho/\rho$ associated with tunnel magnetoresistance, only a small amount of current would be necessary to probe the magnetization angle, contributing a negligible amount of spin-transfer torque and electromigration. (For a good review of MTJ structures and tunnel magnetoresistance, see [74].) The secondary current would be applied between two corners of the dot exactly as it is in our samples and used to induce spin-transfer torque effects. This current is not being used to probe anything, and would therefore have no minimum current density necessary for measurement. Another benefit of using an MTJ configuration is that the enhanced sensitivity to the angle of $\mathbf{M}$ could allow us to directly observe the white noise fluctuations from section 4.2.1 by amplifying the associated voltage fluctuations above the Johnson-Nyquist background of our setup.

6.3.2 Double stochastic resonance

A recent report[75] claimed to see a stochastic resonance in a optomechanical torsion oscillator, but with a double peak in the amplitude. They attributed this double peak to their system having intrinsically asymmetric energy wells. Later numerical studies showed that such a system could produce an amplitude curve like the one seen with the torsion oscillator,[76] though with a much smaller effect than was claimed. It is an open question whether the effect seen was truly "double" stochastic resonance or a manifestation of the shifting duty cycle, a natural consequence of unequal wells as in 4.2.2. Our system is an ideal model in which to study this, as we have naturally asymmetric wells, but we can obtain equal well depths by tuning H_{DC}. In addition, we have been able to see stochastic resonance signatures using all of the standard measurement techniques (amplitude, phase, power spectral density, etc.), so we have the means to identify and account for the effect of duty cycle shifts in a measurement and potentially identify whether a double peak in amplitude should be considered indicative of multiple resonances.

References

[1] A. Ambrozy. *Electronic Noise*. McGraw-Hill, 1982.

[2] H. Nyquist. Thermal agitation of electric charge in conductors. *Physical Review*, 32(1):110–113, 1928.

[3] P. Handel and A. Chung. AIP conference proceedings. In *Noise in physical systems and 1/f fluctuations*, 1993.

[4] A. Van der Ziel. On the noise spectra of semi-conductor noise and of flicker effect. *Physica*, 16(4):359–372, 1950.

[5] M. Weissman. 1/f noise and other slow, nonexponential kinetics in condensed matter. *Reviews of Modern Physics*, 60(2):537–571, 1988.

[6] L. Schuchman. Dither signals and their effect on quantization noise. *IEEE Transactions on Communication Technology*, 12(4):162–165, 1964.

[7] L. Gammaitoni, P. Hänggi, P. Jung, and F. Marchesoni. Stochastic resonance. *Reviews of Modern Physics*, 70(1):223–287, 1998.

[8] N. Smith and P. Arnett. Thermal magnetization noise in spin valves. *IEEE Transactions on Magnetics*, 38(1):32–37, 2002.

[9] R. O'Handley. *Modern magnetic materials*. Wiley-Interscience, 2000.

[10] W. Wernsdorfer, E. Bonet Orozco, K. Hasselbach, A. Benoit, B. Barbara, N. Demoncy, A. Loiseau, H. Pascard, and D. Mailly. Experimental evidence of the Néel-Brown model of magnetization reversal. *Physical Review Letters*, 78(9):1791–1794, 1997.

[11] M. Tsoi, A. Jansen, J. Bass, W. Chiang, M. Seck, V. Tsoi, and P. Wyder. Excitation of a magnetic multilayer by an electric current. *Physical Review Letters*, 80(19):4281–4284, 1998.

[12] E. Myers, F. Albert, J. Sankey, E. Bonet, R. Buhrman, and D. Ralph. Thermally activated magnetic reversal induced by a spin-polarized current. *Physical Review Letters*, 89(19):196801, 2002.

[13] S. Urazhdin, N. Birge, W. Pratt, and J. Bass. Current-driven magnetic excitations in permalloy-based multilayer nanopillars. *Physical Review Letters*, 91(14):146803, 2003.

[14] L. Jaing, E. Nowak, P. Scott, J. Johnson, J. Slaughter, J. Sun, and R. Dave. Low-frequency magnetic and resistance noise in magnetic tunnel junctions. *Physical Review B*, 69(5):054407, 2004.

[15] J. Scola, H. Polovy, C. Fermon, M. Pannetier-Lecœur, G. Feng, K. Fahy, and J. Coey. Noise in mgo barrier magnetic tunnel junctions with cofeb electrodes: Influence of annealing temperature. *Applied Physics Letters*, 90:252501, 2007.

[16] S. Krause, G. Herzog, T. Stapelfeldt, L. Berbil-Bautista, M. Bode, E. Vedmedenko, and R. Wiesendanger. Magnetization reversal of nanoscale islands: how size and shape affect the Arrhenius prefactor. *Physical Review Letters*, 103(12):127202, 2009.

[17] A. Balan, P. Derlet, A. Rodríguez, J. Bansmann, R. Yanes, U. Nowak, A. Kleibert, and F. Nolting. Direct observation of magnetic metastability in individual iron nanoparticles. *Physical Review Letters*, 112(10):107201, 2014.

[18] www.qdusa.com.

[19] T. McGuire and R. Potter. Anisotropic magnetoresistance in ferromagnetic $3d$ alloys. *IEEE Transactions on Magnetics*, 11(4):1018–1038, 1975.

[20] J. Smit. Magnetoresistance of ferromagnetic metals and alloys at low temperatures. *Physica*, 17(6):612–627, 1951.

[21] H. Kramers. Brownian motion in a field of force and the diffusion model of chemical reactions. *Physica*, 7(4):284–304, 1940.

[22] S. Chandrasekhar. Stochastic problems in physics and astronomy. *Reviews of Modern Physics*, 15(1):1–89, 1943.

[23] W. Brown. Thermal fluctuations of fine ferromagnetic particles. *IEEE Transactions on Magnetics*, 15(5):1196–1208, 1979.

[24] B. Cullity and C. Graham. *Introduction to Magnetic Materials*. John Wiley, 2nd edition, 2009.

[25] W. Brown. Thermal fluctuations of a single-domain particle. *Physical Review*, 130(5):1677–1686, 1963.

[26] H. Suh, C. Heo, C. You, W. Kim, T. Lee, and K. Lee. Attempt frequency of magnetization in nanomagnets with thin-film geometry. *Physical Review B*, 78(6):064430, 2008.

[27] I. Klik and L. Gunther. First-passage-time approach to overbarrier relaxation of magnetization. *Journal of Statistical Physics*, 60(3):473–484, 1990.

[28] Y. Kalmykov, W. Coffey, B. Ouaria, and S. Titov. Damping dependence of the magnetization relaxation time of single-domain ferromagnetic particles. *Journal of Magnetism and Magnetic Materials*, 292:372–384, 2005.

[29] P. Déjardin, D. Crothers, W. Coffey, and D. McCarthy. Interpolation formula between very low and intermediate-to-high damping Kramers escape rates for single-domain ferromagnetic particles. *Physical Review E*, 63(2):021102, 2001.

[30] W. Coffey, D. Crothers, J. Dormann, Y. Kalmykov, E. Kennedy, and W. Wernsdorfer. Thermally activated relaxation time of a single domain ferromagnetic particle subjected to a uniform field at an oblique angle to the easy axis: Comparison with experimental observations. *Physical Review Letters*, 80(25):5655–5658, 1998.

[31] C. Nicolis. Long-term climatic transitions and stochastic resonance. *Journal of Statistical Physics*, 70(1):3–14, 1993.

[32] B. McNamara and K. Weisenfeld. Theory of stochastic resonance. *Physical Review A*, 39(9):4854–4869, 1989.

[33] Y. Raikher and V. Stepanov. Stochastic resonance and phase shifts in superparamagnetic particles. *Physical Review B*, 52(5):3493–3498, 1995.

[34] M. Dykman, R. Mannella, P. McClintock, and N. Stocks. Phase shifts in stochastic resonance. *Physical Review Letters*, 68(20):2985–2988, 1992.

[35] P. Jung and P. Hänggi. Hopping and phase shifts in noise periodically driven bistable systems. *Zeitschrift für Physik B*, 90(2):255–260, 1993.

[36] R. Cowburn and M. Welland. Phase transitions in planar magnetic nanostructures. *Applied Physics Letters*, 72(16):2041–2043, 1998.

[37] D. Endean. *The origin of magnetic noise in nanoscale square dots.* PhD thesis, University of Minnesota, 2014.

[38] M. Kitada, H. Yamamoto, and H. Tsuchiya. Reaction between permalloy and several thin metal films. *Thin Solid Films*, 122(2):173–182, 1984.

[39] C. Hampel, editor. *Encyclopedia of the chemical elements.* Chapman-Reinhold, 1968.

[40] A. Mayadas, J. Janak, and A. Gangulee. Resistivity of permalloy thin films. *Journal of Applied Physics*, 45(6):2780–2781, 1974.

[41] M. Steeves. *Electronic transport properties of ruthenium and ruthenium dioxide thin films.* PhD thesis, University of Maine, 2011.

[42] O. Chyan, T. Arunagiri, and T. Ponnuswamy. Electrodeposition of copper thin film on ruthenium. *Journal of the Electrochemical Society*, 150(5):C347–C350, 2003.

[43] M. Green, M. Gross, L. Papa, K. Schnoes, and D. Brasen. Chemical vapor deposition of ruthenium and ruthenium dioxide films. *Journal of the Electrochemical Society*, 132(11):2677–2685, 1985.

[44] M. Karunaratne and R. Reed. Interdiffusion of the platinum-group metals in nickel at elevated temperatures. *Acta Materialia*, 51(10):2905–2919, 2003.

[45] L. Chow, S. Decker, D. Pocker, G. Pendley, and J. Papadopoulos. Interdiffusion in titanium permalloy thin films. *IEEE Transactions on Magnetics*, 15(6):1833–1835, 1979.

[46] J. Adler and J. Jackson. System for observing small nonlinearities in tunnel junctions. *Review of Scientific Instruments*, 37(8):1049–1054, 1966.

[47] P. Chaikin and T. Lubensky. *Principles of condensed matter physics*. Cambridge University Press, 1998.

[48] G. White. *Experimental Techniques in Low-Temperature Physics*. Oxford University Press, 3rd edition, 1979.

[49] A. Grigorenko, P. Nikitin, A. Slavin, and P. Zhou. Experimental observation of magnetostochastic resonance. *Journal of Applied Physics*, 76(10):6335–6337, 1994.

[50] E. Reibold, W. Just, J. Becker, and H. Benner. Stochastic resonance in chaotic spin-wave dynamics. *Physical Review Letters*, 78(16):3101–3104, 1997.

[51] S. Pal and P. Sen. Thermal noise induced stochastic resonance in self organizing Fe nanoparticle system. *Materials Research Express*, 1(4):045035, 2014.

[52] X. Chen, C. Boone, J. Zhu, and I. Krivorotov. Nonadiabatic stochastic resonance of a nanomagnet excited by spin torque. *Physical Review Letters*, 105(4):047202, 2010.

[53] N. Locatelli, A. Mizrahi, A. Accioly, R. Matsumoto, A. Fukushima, H. Kubota, S. Yuasa, V. Cros, L. Pereira, D. Querlioz, J.-V. Kim, and J. Grollier. Noise-enhanced synchronization of stochastic magnetic oscillators. *Physical Review Applied*, 2(3):034009, 2014.

[54] P. Jung and P. Hänggi. Amplification of small signals via stochastic resonance. *Physical Review A*, 44(12):8032–8042, 1991.

[55] P. Jung and G. Mayer-Kress. Spatiotemporal stochastic resonance in excitable media. *Physical Review Letters*, 74(11):2130–2133, 1995.

[56] N. Smith. Modeling of thermal magnetization fluctuations in thin-film magnetic devices. *Journal of Applied Physics*, 90(11):5768–5773, 2001.

[57] Y. Tserkovnyak and A. Brataas. Enhanced Gilbert damping in thin ferromagnetic films. *Physical Review Letters*, 88(11):117601, 2002.

[58] J. García-Palacios and F. Lázaro. Langevin-dynamics study of the dynamical properties of small magnetic particles. *Physical Review B*, 58(22):14937–14958, 1998.

[59] A. Perez-Madrid and J. Rubi. Stochastic resonance in a system of ferromagnetic particles. *Physical Review E*, 51(5):4159–4164, 1995.

[60] B. Storonkin. The theory of dielectric-relaxation in nematic liquid-crystals. *Kristallografiya (Soviet Physics Crystallography)*, 30:841, 1985.

[61] B. Storonkin. Orientation relaxation in the case of a strong induced dipole interaction with an external field. *Teoreticheskaya i Matematicheskaya Fizika*, 41(3):1098–1104, 1978.

[62] C. Kittel. *Introduction to Solid State Physics*. John Wiley, 1986.

[63] J. Slonczewski. Current-driven excitation of magnetic multilayers. *Journal of Magnetism and Magnetic Materials*, 159(1):L1–L7, 1996.

[64] M. Stiles and J. Miltat. Spin transfer torque and dynamics. In *Spin Dynamics in Confined Magnetic Structures III*. Springer, 2006.

[65] L. Berger. Prediction of a domain-drag effect in uniaxial, non-compensated, ferromagnetic metals. *Journal of Physics and Chemistry of Solids*, 35(8):947–956, 1974.

[66] T. Taniguchi, Y. Utsumi, and H. Imamura. Thermally activated switching rate of a nanomagnet in the presence of spin torque. *Physical Review B*, 88(21):214414, 2013.

[67] J. Black. Electromigration–a brief survey and some recent results. *IEEE Transactions on Electron Devices*, 16(4):338–347, 1969.

[68] P. Ho and T. Kwok. Electromigration in metals. *Reports on Progress in Physics*, 52(3):301–348, 1989.

[69] I. Blech and E. Meieran. Direct transmission electron microscope observation of electrotransport in aluminum thin films. *Applied Physics Letters*, 11(8):263–266, 1967.

[70] C. Lee, B. Kang, M. Lee, S. Ahn, G. Stefanovich, W. Xianye, K. Kim, J. Hur, H. Yin, Y. Park, and I. Yoo. Electromigration effect of Ni electrodes on the resistive switching characteristics of NiO thin films. *Applied Physics Letters*, 91(082104), 2007.

[71] M.-A. Nicolet. Diffusion barriers in thin films. *Thin Solid Films*, 52:415–443, 1978.

[72] Z. Néda. Stochastic resonance in Ising systems. *Physical Review E*, 51(6):5315–5317, 1995.

[73] W. Yager and R. Bozorth. Ferromagnetic resonance at microwave frequencies. *Physical Review*, 72(1):80–81, 1947.

[74] E. Tsymbal, O. Myrasov, and P. LeClair. Spin-dependent tunneling in magnetic tunnel junctions. *Journal of Physics: Condensed Matter*, 15(4):R109–R142, 2003.

[75] F. Mueller, S. Heugel, and L. Wang. Optomechanical stochastic resonance in a macroscopic torsion oscillator. *Physical Review A*, 79(3):031804, 2009.

[76] M. Borromeo and F. Marchesoni. Double stochastic resonance over an asymmetric barrier. *Physical Review E*, 81(1):012102, 2010.

[77] S. Paris, P. Kornprobst, J. Tumblin, and F. Durand. Bilateral filtering: theory and applications. *Foundations and Trends in Computer Graphics and Vision*, 2009.

[78] E. Billauer. Peakdet: peak detection using MATLAB. Online access via www.billauer.co.il/peakdet.html, 2012.

Appendix A

Data processing algorithms

A major step in our data processing is converting our raw oscilloscope data into a list of dwell times. This can be done any of several ways, but all require converting the raw oscilloscope trace to a vector of identical length with only two values of voltage V_H and V_L. (Note: throughout this appendix, we will use the phrase "digitize" to refer to the process of extracting this binary vector from the raw oscilloscope trace.) Three different oscilloscopes were used in the course of this study: a Tektronix 2230 with a 4096 point record length, a Tektronix TDS 2012c with a 2500 point record length, and a Tektronix DPO 4034b that was used on the 100 kilopoint setting (the 4034b has a maximum record length of 20 megapoints). With the last of these, file size and computer time can become a real concern, given that a typical temperature sweep spanning 40 K involves several thousand traces. As an example, the raw data that were used to fit the Arrhenius law for Fig. 4.8 totaled 5.3 GB. Accordingly, we have explored a number of different algorithms for processing our data in an attempt to balance speed and sophistication. The signal processing software MATLAB was used for all work.

In our early algorithms, data were binned to a histogram of voltage values as shown in Fig. A.1. This histogram was then fit to two Gaussian peaks to determine windows that define the high and low voltage values. An algorithm then scanned the length of the trace to determine which voltage window each individual sample belonged in. For samples that did not fall into either window, the algorithm assigned the voltage value of the previous sample, i.e., if the algorithm did not know which value to assign to t_i, it assigned the same value as for t_{i-1}. This method worked well for most data, but it

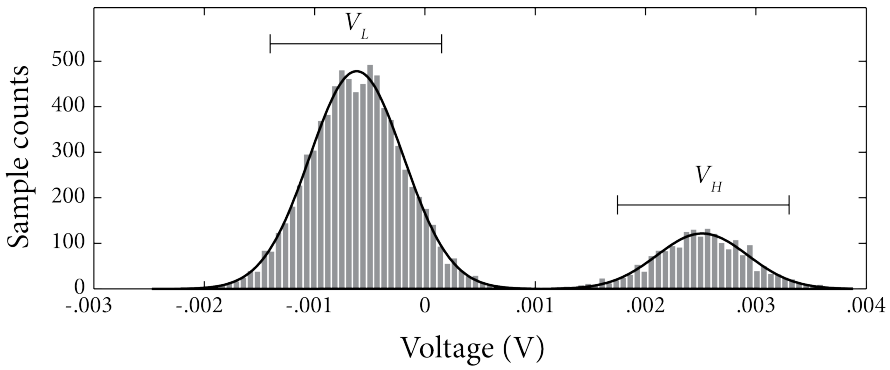

Figure A.1: Histogram of voltage samples. Black line shows fit to double Gaussian. V_L and V_H denote windows used for digitizing individual samples.

had a number of issues. First, it tended to glitch for traces where the duty cycle heavily favored one well. This happens because only a small number of points exist around the second voltage, so the fitting algorithm cannot find two clear Gaussian peaks. We can prevent this from affecting the rest of the digitization process by including a clause that will discard traces if the fitted ΔV is significantly different than the known ΔV for the transition. The problem remains, though, that these data are undigitizable. In addition, this algorithm runs slowly in MATLAB because it is inherently linear, i.e., the computer cannot assign a value to t_i until it knows the result of t_{i-1}. Even a compiled version of the low-level digitizer required > 10 s per trace for data taken with the 4034b.

A faster option is to use a digital comparator that only looks at each sample's relationship to the midpoint voltage. For this to work, though, we need to clean up the raw data, otherwise the digitization algorithm can register false transitions from the white noise background. We do this using a bilateral filter, represented mathematically as

$$V'(t_i) = \frac{\sum_k V_k \exp\left[-\frac{(t_k - t_i)^2}{\sigma_t^2}\right] \times \exp\left[-\frac{(V_k - V_i)^2}{\sigma_V^2}\right]}{\sum_k \exp\left[-\frac{(t_k - t_i)^2}{\sigma_t^2}\right] \times \exp\left[-\frac{(V_k - V_i)^2}{\sigma_V^2}\right]}. \tag{A.1}$$

Or, if we define

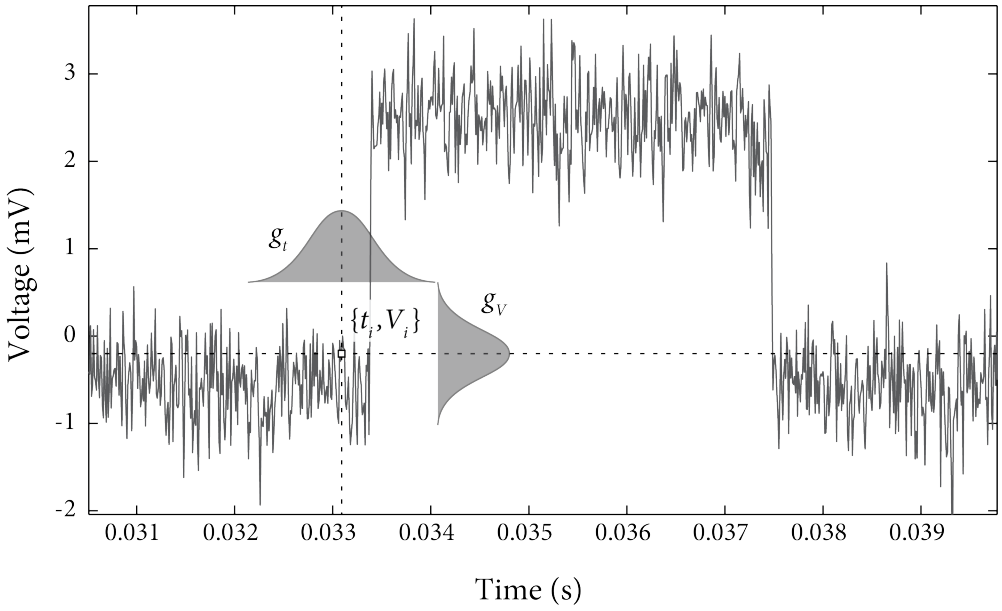

Figure A.2: Bilateral filter. For a point $\{t_i, V_i\}$, the algorithm scales nearby points by the two windowing functions g_t and g_V before averaging to obtain a new $\{t_i, V_i'\}$.

$$g_t \equiv \exp\left[-\frac{(t_k - t_i)^2}{\sigma_t^2}\right], \qquad g_V \equiv \exp\left[-\frac{(V_k - V_i)^2}{\sigma_V^2}\right], \tag{A.2}$$

this can written as

$$V'(t_i) = \frac{\sum_k V_k g_t g_V}{\sum_k g_t g_V}. \tag{A.3}$$

The two functions g_t and g_V are windowing functions that, taken together, form a two-dimensional ellipse around the point $\{t_i, V_i\}$ as shown in Fig. A.2. Eq. A.3 then takes the average voltage of all the points within this window to create the new voltage V_i'. The results of a filtering cycle are shown in Fig. A.3.a. Note that it is the use of g_V, rather than just g_t, that allows a bilateral filter to preserve edges since points that are far from $\{t_i, V_i\}$ in voltage will not count toward the average, even if they are close in time. Computer speed was optimized by performing array operations rather than loops for all calculations. For more information on bilateral filtering, see [77].

Although a simple comparator is the quickest tool for digitizing filtered data, it is not reliable for data that are either very noisy or where the Kramers time is comparable

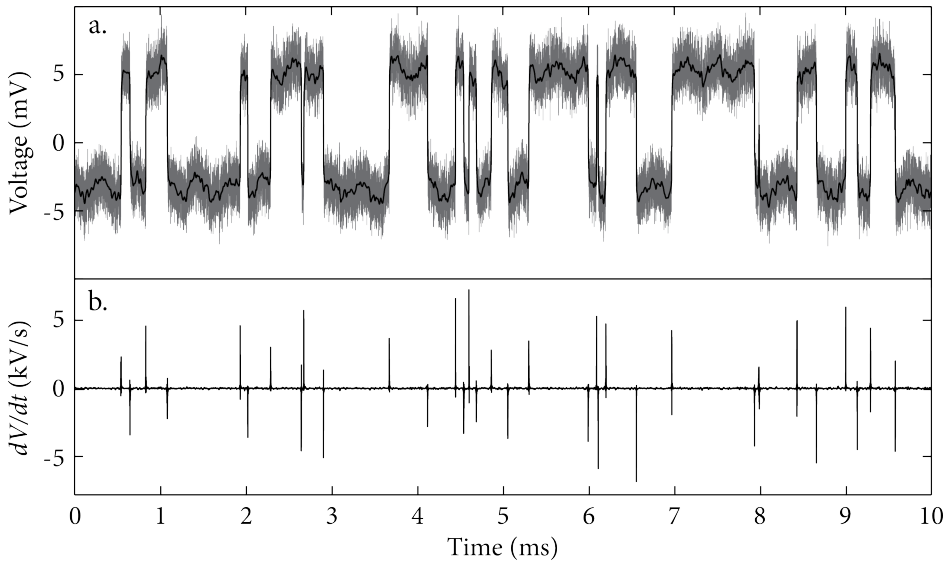

Figure A.3: (a) Effects of bilateral fitting. Raw trace is shown in gray, with filtered trace superimposed in black. (b) Time derivative of filtered data. Transitions are seen as positive or negative spikes in derivative.

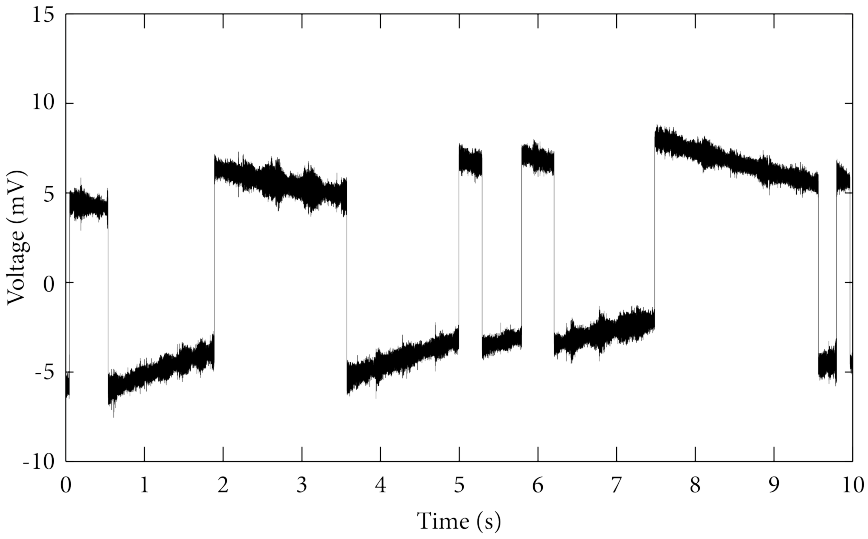

Figure A.4: Trace with τ_1 on the same order as the time constant of the DC blocking filter. Because the trace can cross the midpoint without a transition, a simple voltage comparator will register false transitions, and a more sophisticated digitization algorithm is necessary.

to the time constant of the blocking capacitor used to remove the DC voltage before measurement. A sample of such a signal is shown in Fig. A.4. The attenuation from the highpass filter can clearly be seen, and makes a comparator measurement impractical since it will register false transitions as the voltage signal will frequently cross the midpoint without any actual transition.

For data such as these, it is easier to work with the first time derivative of the filtered signal, as in Fig. A.3.b. Here, the transitions show up as individual spikes (high or low) in dV/dt. In order to digitize these spikes, we used a modified version of the peak detection algorithm detailed in [78]. Again, this is an inherently linear algorithm, but we have found that it can be compiled to run at an acceptable speed.

As a final note, with all processing methods, it is useful to have the computer plot the raw trace along with the reconstructed (binary) trace in real time as it processes each file. This allows the user to monitor the results and abort processing if a particular algorithm is unsuited to the dataset.

Appendix B

Relationship between ZDA and duty cycle

The zero-drive amplitude (ZDA) and duty cycle $\mathcal{D}$ are related for an RTN signal. This can be calculated for a system with two states $\mathbf{M}_A$ and $\mathbf{M}_A$ as follows:

The average value of magnetization $\overline{\mathbf{M}}$ is given by

$$\overline{\mathbf{M}} = \mathbf{M}_A\mathcal{D} + \mathbf{M}_B(1-\mathcal{D}), \tag{B.1}$$

which means that the deviations $\mathbf{M} - \overline{\mathbf{M}}$ for the two states are

$$|\mathbf{M} - \overline{\mathbf{M}}| = \begin{cases} (\mathbf{M}_A - \mathbf{M}_B)(1-\mathcal{D}) & \text{for} \quad \mathbf{M} = \mathbf{M}_A \\ (\mathbf{M}_A - \mathbf{M}_B)\mathcal{D} & \text{for} \quad \mathbf{M} = \mathbf{M}_B. \end{cases} \tag{B.2}$$

Since ZDA is defined by $\langle|\mathbf{M} - \overline{\mathbf{M}}|\rangle$, these combine to form

$$\begin{aligned} \text{ZDA} &= \mathcal{D}|\mathbf{M}_A - \overline{\mathbf{M}}| + (1-\mathcal{D})|\mathbf{M}_B - \overline{\mathbf{M}}| \\ &= 2(\mathbf{M}_A - \mathbf{M}_B)(\mathcal{D} - \mathcal{D}^2). \end{aligned} \tag{B.3}$$

Appendix C

Abbreviations

Acronym	Meaning
AC	Alternating current
AMR	Anisotropic magnetoresistance
CGS	Centimeter-gram-second
DC	Direct current
FM	Ferromagnet
FMR	Ferromagnetic resonance
LLG	Landau-Lifshitz-Gilbert
MRSEC	Materials research science and engineering centers
MTJ	Magnetic tunnel junction
MTTF	Mean time to failure
NM	Nonmagnetic layer
NNIN	National Nanotechnology Infrastructure Network
NSF	National Science Foundation
ONR	Office of Naval Research
PMGI	Polydimethylglutarimide
PMMA	Polymethylmethylacrylate
PSD	Power spectral density

Continued on next page

Acronym	Meaning
RKKY	Ruderman-Kittel-Kasuya-Yosida
RMS	Root-mean-square
RTN	Random telegraph noise
SAF	Synthetic antiferromagnet
SEM	Scanning electron microscope
SNR	Signal to noise ratio
SQUID	Superconducting quantum interference device
UMN	University of Minnesota
USB	Universal serial bus
UV	Ultraviolet
ZDA	Zero-drive amplitude